

https://dspace.org/

Structural and kinematic analysis of a pseudotachylite-bearing fault system within the upper Critical Zone of the Bushveld Complex, South Africa

Hales, Matthew Paul

2020
https://hdl.handle.net/10539/31024

Downloaded from a DSpace repository. https://dspace.org/



UNIVERSITY OF THE
WITWATERSRAND,
JOHANNESBURG

Structural and kinematic analysis of a pseudotachylite-bearing fault system within the upper Critical Zone of the Bushveld Complex, South Africa

Matthew Paul Hales

A dissertation submitted to the Faculty of Science, University of the Witwatersrand, Johannesburg, in fulfilment of the requirements for the degree of

Master of Science Geology

02 April 2020, Johannesburg

https://orcid.org/0000-0001-8572-7097

Declaration

I declare that this dissertation is my own, unaided work. It is being submitted for the Degree of Master of Science at the University of the Witwatersrand, Johannesburg. It has not been submitted before for any degree or examination at any other University.



(Signature of candidate)

02 day of April 2020 at the University of the Witwatersrand

Abstract

Two SSW-dipping, pseudotachylite-bearing faults are exposed within the northern portion of the Bushveld Complex Eastern Limb Critical Zone. Both faults display S-plunging slickenlines on fault-parallel shear fracture surfaces as well as several planar to sigmoidal macroscopic and microscopic fractures and fabrics (south-dipping P shear fractures and quasi-ductile sigmoidal fabrics and north-dipping R, R' and P' shear fractures) that are consistent with top-to-north, reverse-sense displacement. These fractures and fabrics display a mutually crosscutting relationship with E and W-dipping normal-sense shear fractures. From the contemporaneous N-S compression and E-W extension, oblate strain with principal stress axes orientations of subhorizontal N-S σ_1, subhorizontal E-W σ_2 and subvertical σ_3 is deduced.

The lower fault crosscuts the LG-6 chromitite and the footwall and hangingwall pyroxenite layers is steeply SSW-dipping. It displays a reverse, dip-slip displacement of 1.8 m. Field observations show a single pseudotachylite injection vein extending from the fault while petrographic studies show both quasi-ductile cataclasite and cataclasite within the fault. The fault zone displays pervasive epidote alteration. Petrographic studies revealed strong intracrystalline fracturing of pyroxenes, however, these fractures do not propagate into interstitial plagioclase. This phenomenon was observed in all pyroxene-plagioclase lithologies in the vicinity of the faults.

The upper fault is a shallowly SSW-dipping, layer-parallel fault at the contact of the MG-4 chromitite and underlying anorthosite near the boundary between the lower and upper Critical Zone. Owing to the layer-parallel orientation of the fault and homogeneity of the hangingwall and footwall rocks, the amount of slip for this fault is undetermined. Several fault-rock types were observed along strike for approximately 6 km. These fault rocks include quasi-ductile cataclasite, pseudotachylite and cataclasite. The quasi-ductile cataclasite is defined by highly altered and comminuted anorthosite with comminuted chromite aggregates defining a S-dipping sigmoidal fabric. The quasi-ductile cataclasite is crosscut by cogenetic pseudotachylite and cataclasite which have mutually crosscutting relationships. Pseudotachylite dykes form both parallel and almost orthogonal to the fault fabric, which is controlled by magmatic layering and foliation. The layer-parallel dykes are up to 5 cm thick and may contain more than one pseudotachylite generation. Up to four of these dykes may be exposed in outcrop. The layer-oblique dykes, interpreted as injection veins, extend up to 20 cm from the layer-parallel dykes preferentially into the footwall. Using crosscutting relationships between several dykes as well as mutually crosscutting relationships between pseudotachylite, cataclasite and oblique shear fractures, at least three pseudotachylite generations are identified, indicating that the fault underwent several seismic-slip events.

SEM and X-ray element mapping work shows extensive chloritization of the quasi-ductile cataclasite. Crosscutting relationships between chloritization textures within cataclasite and pseudotachylite suggests the ingress of fluids during interseismic periods, with the younger fault-rock generations displaying less chloritization. Chloritization during interseismic periods may have facilitated subsequent seismic-slip events that led to renewed friction melting and pseudotachylite generation.

Field and petrographic analysis of the upper fault zone indicates that strain was initially partitioned into the anorthosite along chromite aggregates that enhanced the propagation of fractures owing to the strong competency contrast between chromite and plagioclase. Increasing slip and fracture density led to the widening of the fault zone downward into the anorthosite from the MG-4 chromitite contact. The widening of the fault zone formed quasi-ductile cataclasite which was subsequently crosscut by pseudotachylite and cataclasite as the faulting mechanism transitioned from continuous cataclastic flow to seismic stick-slip faulting. Owing to the transition in the faulting mechanism, the ambient fault zone temperature is deduced to have decreased below 300°C. Despite ambient greenschist temperatures, the fault is presumed to have formed outside the greenschist facies and typical seismogenic zone owing to the emplacement depth and mineralogy of the Bushveld Complex.

The initiation and progressive deformation of the two faults are attributed to the development of a S-type flanking fold in the Transvaal and Bushveld Complex rocks abutting the Thabazimbi-Murchison Lineament during the sinistral-sense reactivation of the lineament during a broadly N-S compressional deformation event following the emplacement of the Bushveld Complex, ca. 2.04-1.95 Ga.

Acknowledgements

The furtherance of my studies was made possible by a Council for Geosciences full-time bursary which covered my living expenses and tuition these past two years. I am also indebted to Prof Roger Gibson and Dr Asinne Tshibubudze who have generously supported this project using their funding. Their patience in sharing their knowledge and wisdom while supervising this project is greatly appreciated.

I am grateful to Prof Paul Nex who introduced the research topic during the 2017 Honours field trip.

Kimberley Beaton, Caitlin Stewart and Nonkuselo Madlakana were a great help while using the TIMA. Both Kim and Caitlin took time away from their projects to ensure that I was appropriately trained on the instrument.

Kirsten Youlton, Leonidas Vonopartis and Danielle Duarte have often "gone the extra mile" to help in both academic and personal matters. Their friendship is valued highly.

The School of Geosciences support staff are thanked for their assistance over the past two years. Caiphas Majola and Samuel Tshabalala helped produce the thin sections used for the project. Lenah Mtiyane, Lungelwa Ndeve, Matt Kitching and Nicolas Chokoe helped with the general administration associated with the project.

Lastly, I would like to thank my parents, Paul and Michelle Hales, who have made significant sacrifices to ensure I receive a good education. They have also faithfully taught me to trust in the Lord; in His grace, He has sustained and comforted me during my studies.

Contents

Declaration ii

Abstract iii

Acknowledgements v

List of Figures ix

1 Introduction 1

1.1 The Bushveld Complex 2

1.2 Deformation of Bushveld Complex and Transvaal Supergroup rocks 5

1.2.1 Diapirism 5

1.2.2 Flexural-slip folding induced by lithostatic loading 6

1.2.3 Regional stress field 6

1.3 Occurrence and development of pseudotachylite 8

1.3.1 Prerequisites for formation 8

1.3.2 Formation process 9

1.3.3 Form of occurrence 10

1.3.4 Indicators of friction melt production 12

1.3.5 Melting temperatures for common Critical Zone minerals 13

2 Scientific Procedure 15

2.1 Hypotheses, Aim and Objectives 15

2.1.1 Hypotheses 15

2.1.2 Aim 15

2.1.3 Objectives 15

2.2 Methodology 16

2.2.1 Regional lineament desktop study 16
2.2.2 Field Mapping and Sample Collection 16
2.2.3 Data processing and sample preparation 17
2.2.4 Microscopy 18
2.2.5 TESCAN Integrated Mineral Analyser data processing 19
3 Results 23
3.1 Regional structures 23
3.2 The geology of Jagdlust Farm and adjacent farms 24
3.2.1 RLS stratigraphy 24
3.2.2 Dykes and sills 31
3.3 The chromite-foliated anorthosite fault 32
3.3.1 Chromite-foliated anorthosite wallrock 35
3.3.2 Quasi-ductile cataclasite 36
3.3.3 Pseudotachylite 41
3.3.4 Cataclasite and breccia 51
3.3.5 Crosscutting relationships between fault rock types 56
3.3.6 Comparison of the chromite-foliated anorthosite to the other magmatic lithologies 60
3.4 The LG-6 chromitite reverse fault 62
3.5 Kinematic Indicators 67
4 TIMA analysis and description 70
4.1 Alteration mineralogy and textures 73
4.2 Fault rocks hosted in the chromite-foliated anorthosite 76
4.2.1 Fractured chromite-foliated anorthosite 76
4.2.2 Quasi-ductile cataclasite 78
4.2.3 Pseudotachylite 79

4.2.4 Cataclasite and breccia 83

5 Discussion 84

5.1 The presence of pseudotachylite 84

5.1.1 Prerequisite processes 84

5.1.2 Friction melt indicators 85

5.1.3 Limiting factors 86

5.2 Fault zone P-T conditions 89

5.3 Structures and kinematics 92

5.3.1 Diapirism 92

5.3.2 Flexural-slip folding induced by lithostatic loading 93

5.3.3 Proposed stress field 93

5.4 Strain partitioning within the Jagdlust Farm stratigraphy 94

5.5 Progressive evolution of faulting within the chromite-foliated anorthosite 95

5.6 Relative age for the development of the Jagdlust Farm Fault system 98

5.6.1 Cooling history of the Bushveld Complex 98

5.6.2 Regional stress field 99

5.7 Structural relationship of the Jagdlust Farm fault system to the Thabazimbi-Murchison Lineament 101

5.8 Summary 102

References 104

List of Figures

Figure 1.1: Satellite imagery of the northern portion of the Eastern Limb of the Bushveld Complex showing the study area, Jagdlust Farm boundary and house and several significant geological features (Esri, 23 June 2013). The overview map is a schematic map of the Bushveld Complex, Transvaal Supergroup and Archaean Basement from Eales and Cawthorn (1996) (see Figure 1.2). The black box shows the extent of the Satellite image. UTM Grid 35J (Esri, 23 June 2013). 2

Figure 1.2: Schematic Map of the Bushveld Complex from Eales and Cawthorn (1996) showing the Northern, Eastern, Western, far Western and Southern limbs of the Bushveld Complex, as well as the mafic and felsic portion of the Bushveld Complex, Transvaal Supergroup and Archaean Basement. The black box shows the estimated extent of the Satellite image in Figure 1.1. 3

Figure 1.3: Stratigraphic column of the RLS with emphasis on the Critical Zone and Middle Group chromitites 4

Figure 1.4: Regional stress field as proposed by Du Plessis and Walraven (1990) showing the observed and expected structures within the Eastern Limb of the Bushveld Complex. The stress field is proposed to have a NE-SW primary compressive stress axis, which re-activated the TML in a sinistral-sense; developing NW-trending fold axes and NNE-trending normal-faults such as the Wonderkop fault (Du Plessis and Walraven, 1990; Basson, 2019). 7

Figure 1.5: The 6 forms of pseudotachylite as described by Magloughlin (1989) in the Nason terrane, USA. Type 1 are discontinuous pseudotachylite-filled, irregular fractures. Type 2 are planar sheets with lenses and injection veins. Type 3 and 4 form a continuum of injection vein network and pseudotachylite supported breccia. Type 5 are sinusoidal sheets of pseudotachylite. Type 6 form by the reactivation and overprinting of Types 1 through 5. 11

Figure 1.6: Fracture sets forming internal to the paired-planar generation surfaces. P, P', P" and T_3 fractures form in contractional slab-duplexes. X, X' and T_2 fractures form in extensional slab-duplexes. Blue, red, and green indicate normal-slip, reverse-slip, and fracture opening, respectively. 12

Figure 2.1: Satellite imagery of the study area with sample localities. The areas I) and II) are enlarged from the respective areas delineated on the base map. UTM Grid 35J (Esri, 23 June 2013). 17

Figure 2.2: Flow diagram of the methodology used for the production of Fe-Mg-Cr and Mg-Ca-Al three-element colour-composite maps. The Fe, Mg and Cr elemental maps from MHL-006A scanning area A are used to exemplify the process. 20

Figure 2.3: Flow diagram of the methodology used for the production of (Fe+Mg-Cr)-Cr-Na three-band colour-composite map. The Fe, Mg, Cr and Na elemental maps from MHL-006A scanning area A are used to exemplify the process. 22
Figure 3.1: Regional lineaments ≥1 km and diapiric domes within the northern portion of the Eastern Limb, Bushveld Complex. UTM Grid 35J (Esri, 23 June 2013). 23
Figure 3.2: Rose diagram of the regional lineaments traced within the RLS lithologies of the northern portion of the Eastern Limb, Bushveld Complex (n=102). The white, red, and blue bars correspond to the NNW, NE and E-W trends traced in Figure 3.1, respectively. 24
Figure 3.3: Profile of the northern slope of the ridge south of the R37 on the Jagdlust Farm with key stratigraphic layers: the pyroxenites marking the start and end of the stratigraphic section for the study, the anorthosite marking the lower-upper Critical Zone boundary and the anorthosite of interest to this study. 25
Figure 3.4: Simplified stratigraphy of the lower-upper Critical Zone boundary with an accompanying outcrop photograph of the boundary. The boundary is at the lower contact of the pyroxene-foliated anorthosite with the underlying pyroxenite and is marked by the dashed blue line. 26
Figure 3.5: Simplified stratigraphy of the lower-upper Critical Zone boundary with accompanying outcrop photographs of the upper (A) and lower (B) contacts of the pyroxene-foliated anorthosite. 28
Figure 3.6: Simplified stratigraphy of the lower-upper Critical Zone boundary accompanied by (A) chromitite and anorthosite nodules in the pyroxene-foliated anorthosite upper contact and (B) hook-shaped nodules of anorthosite within a pyroxenite of the pyroxenite series between the LG-7 chromitite and lower-upper Critical Zone boundary. 29
Figure 3.7: Simplified stratigraphy of the lower-upper Critical Zone boundary accompanied by an outcrop photograph of the MG-4 chromitite overlying the chromite-foliated anorthosite (the dashed white line traces the contact). The anorthosite stringer layer in the chromitite is seen with the stringer's irregular form. The chromitite-pyroxenite contact parallels the morphology of the anorthosite stringer layer (solid white line). 30
Figure 3.8: Equal area stereoplot of the poles to the magmatic layering (n=12, blue squares) of the RLS and chromite-foliation (n=6, red diamonds) within the study area. The average planes, as dip-angle → dip-direction, for layering (blue) and the foliation (red) are dipping at 21°→208° and 26°→205°, respectively. 31

Figure 3.9: Equal area stereoplot of the planes for the post-RLS dykes and sill within the study area. Orientations are labelled dip → dip-direction of the plane. The 74°→272° and 58°→059° dykes lie at a 58° angle, whereas the 23°→205° sill and 74°→272° dyke lie at a 67° angle. 32

Figure 3.10: A) is a satellite image of the study area with the chromite-foliated anorthosite (white lines) and LG-6 chromitite (black lines) outcrops traced. The white box delineates the enlarged area of B) and C). B) shows the localities for samples collected on Jagdlust farm. B) shows the localities for several outcrop photographs, e.g. Figure 3.14. UTM Grid 35J (Esri, 23 June 2013). 33

Figure 3.11: Sketch diagram of the fault within the chromite-foliated anorthosite bounded by the MG-4 chromitite and middle pyroxenite showing the main spatial and geometric characteristics of the fault. The sketch is drawn parallel to the slickenlines on the layer-parallel fracture surfaces. The P, P', R and R' fractures indicate a top-to-north displacement. The black boxes with labels represent where the respective figures for the features can be found, e.g. "11B, 13, 30" indicates that Figures 3.11B, 3.13 and 3.30 show the quasi-ductile cataclasite overlying a pseudotachylite and cataclasite. The diagram is not drawn to scale. 34

Figure 3.12: Outcrop photograph of foliation-parallel fractures (dashed blue lines) and foliation-oblique fractures (dashed yellow lines) associated with the foliation parallel fractures. 35

Figure 3.13: A) PPL photomicrograph of a portion of MHJL-001 thin section showing foliation-parallel (dashed yellow lines) and foliation-oblique (dashed orange lines) fractures with anastomosing form within the chromite-foliated anorthosite. B) XPL photomicrograph of a portion of MHJL-002 thin section showing foliation-parallel (dashed yellow lines) fractures with planar form within the chromite-foliated anorthosite. 36

Figure 3.14: A) Outcrop photograph of a rhomboidal to sigmoidal-clast, quasi-ductile cataclasite with sharp boundaries with overlying cataclasite and underlying anorthosite. B) Outcrop photograph of a quasi-ductile cataclasite with sigmoidal fabric and fault-parallel shears. The quasi-ductile cataclasite has a gradational upper boundary with the anorthosite wallrock and a sharp contact with the underlying pseudotachylite GPPD. The sigmoidal fabric and fault-parallel shears are crosscut by a pseudotachylite injection vein. The pseudotachylite has a gradational boundary with the underlying cataclasite, which grades into a breccia. QCt is quasi-ductile cataclasite, Pst is pseudotachylite, Ct is cataclasite, Br is breccia. See Figure 3.10 for photograph location. 37

Figure 3.15: Photograph of hand sample MHJL-021, which shows alternating clast-rich and clast-poor bands within the sigmoidal-clast, quasi-ductile cataclasite (QCt). Owing to the shape of the sample a N-S profile photograph is not informative. See Figure 3.10 for photograph location. 38

Figure 3.16: PPL photomicrograph of hangingwall anorthosite and lower cataclasite with sigmoidal fabric and fault-parallel shears in MHJL-022. The thin section shows R' fractures which are crosscut by sigmoidal fabrics and fault-parallel shears. Furthermore, the clast-shape variation is seen with well-rounded clasts between the two traced fault-parallel shears and subangular to subrounded clasts below the traced fault-parallel shears. See Fractures under Crosscutting relationships for foliation-parallel fractures. See Figure 2.1 for sample location..... 39

Figure 3.17: Photomicrograph showing the onset of subgrain rotation (SGR) within a clast in MHJL-022. A) is a PPL photomicrograph. B) and C) are XPL photomicrographs. C) was taken after the stage was rotated 10° anticlockwise with respect to B). 40

Figure 3.18: An E-W profile outcrop, perpendicular to the fault slip direction, of the chromite-foliated anorthosite showing four pseudotachylite GPPDs. Each GPPD is underlain by cataclasite. Two of the GPPDs can be seen to be the result of bifurcations (white box, see Figure 3.19). A 30 cm thick breccia is seen and has gradational boundaries with the chromite foliated anorthosite. See Figure 3.10 for photograph location. 42

Figure 3.19: Outcrop photograph of the uppermost pseudotachylite GPPD and an underlying GPPD showing a bifurcation. The pseudotachylite injection vein crosscuts the pseudotachylite within the underlying GPPD and bifurcation but is displaced along the top surface of the middle GPPD. Furthermore, the pseudotachylite from the upper GPPD injects into a W-dipping, normal-sense shear fracture, which appears to displace the injection vein associated with the upper GPPD. The injection vein is also crosscut by a foliation-parallel fracture. Ct is cataclasite. The photograph is an enlargement of the white box, Figure 3.18. See Figure 3.10 for photograph location..... 43

Figure 3.20: Equal area stereoplot of poles to GPPDs (n=10). The solid red line is the average plane to GPPDs poles (dipping at 25° → 195°). The blue line is the average plane to magmatic layering (see Figure 3.8). 44

Figure 3.21: Outcrop-scale pseudotachylite features and relationships with the host and fault rocks. A) shows two GPPDs, the upper having two pseudotachylite generations, both of which overlie breccia. The photo shows the weakly undulatory nature of the GPPDs. Injection veins from the upper GPPD inject downward from the GPPDs into the breccia, whereas the lower GPPD has upward and downward injection veins. B)

shows the mixing of pseudotachylite with the underlying breccia. C) shows breccia overlying a GPPD. The GPPD has a gradational boundary with the underlying cataclasite. Several downward injection veins and a single upward injection vein extend from the GPPD. QCt is quasi-ductile cataclasite, Pst is pseudotachylite, Ct is cataclasite. See Figure 3.10 for photograph location. 45

Figure 3.22: Outcrop photograph of a pseudotachylite GPPD with two pseudotachylites, clast-rich and clast-poor, within the GPPD (outlined by red lines). The GPPD has sharp contacts with the highly fractured anorthosite. Injection veins extend downward and have an irregular shape. The photo is of a boulder and therefore unoriented. Pst is pseudotachylite, Ct is cataclasite. See Figure 3.10 for photograph location. ... 46

Figure 3.23: Outcrop photograph of a pseudotachylite injection dyke with conjugate form (traced by the red lines). The photographed surface is subparallel to the layer-parallel fracture surface. 46

Figure 3.24: Equal area stereoplot of poles to pseudotachylite injection veins (n= 13, red dots with black outline) and average plane to magmatic layering (blue line). 47

Figure 3.25: PPL photomicrograph of the lower portion of MHJL-006A thin section. The image focuses on the pseudotachylite-cataclasite relationship. The solid red lines trace sharp pseudotachylite contacts whereas the dashed lines show diffuse boundaries with breccia or cataclasite. The dashed yellow line traces a convoluted and diffuse pseudotachylite. Pst is pseudotachylite, Ct is cataclasite, Br is breccia. 48

Figure 3.26: PPL photomicrograph of the MHJL-009 thin section, emphasizing the preferential direction of pseudotachylite injection veins and showing a cataclasite (Ct) that crosscuts a pseudotachylite injection vein. Both cataclasites have pseudotachylite at their margins. The cataclasite and pseudotachylite are crosscut by high-angle, normal-sense fractures. The host rock is highly fractured chromite-foliated anorthosite. The white arrows with red fill mark downward injecting pseudotachylite veins. The white arrows with blue fill mark upward injection veins. The sample is unoriented, therefore the directions are relative. See chapter 4 for TIMA analysis of the leftmost pseudotachylite injection vein crosscut by the cataclasite. 49

Figure 3.27: Photomicrograph of thin section MHJL-008E in PPL. The sample shows disruption of the older GPPDs (fractures traced by yellow lines) in the upper part of the image but not the younger GPPDs in the lower part of the image (all are traced with solid red lines). The sample also shows irregular injection vein networks between the GPPDs. The host rock is highly fractured chromite-foliated anorthosite. The sample is unoriented, therefore the directions are relative. 49

Figure 3.28: PPL photomicrographs of pseudotachylite injection veins from MHJL-006A (A) and MHJL-008D (B). A) shows light brown, chromite clast-dominated pseudotachylite with banding, pseudotachylite-crosscutting fractures with a consistent top-to-right displacement sense and a fracture contemporaneous with pseudotachylite generation. B) shows dark brown, plagioclase clast-dominated pseudotachylite. Several clasts within pseudotachylite appear to be crosscut by oblique, normal-sense shear fractures, however, these displacements are not observed within the colour banding adjacent to the clasts. A) has higher exposure than B) so that the colour banding is visible, giving the appearance that A) has a lighter colour than B). See Chapter 4 for TIMA analysis of both samples. The samples are unoriented, therefore the directions are relative. 50

Figure 3.29: Satellite image of the study area with Western and Eastern outcrop on Jagdlust Farm indicated. The white and black lines trace outcrop of the chromite-foliated anorthosite and LG-6 chromitite, respectively. The white dot marks the location of The LG-6 chromitite reverse fault. UTM Grid 35J (Esri, 23 June 2013). 51

Figure 3.30: Outcrop photograph showing normal-sense shear fractures, which displace a GPPD and underlying breccia. See Figure 3.10 for photograph location. 52

Figure 3.31: Outcrop photograph of two GPPDs (Pst) bounding a breccia (Br). The upper GPPD crosscuts a sigmoidal-fabric, quasi-ductile cataclasite (QCt). Both GPPDs are underlain by cataclasite, which grades into breccia. The solid white line traces the sharp contact between the quasi-ductile cataclasite and pseudotachylite. The dashed white line shows the transition from pseudotachylite to cataclasite or breccia. See Figure 3.10 for photograph location. 53

Figure 3.32: Outcrop photograph showing the pseudotachylite, cataclasite and fracture relationships in the Jagdlust Farm western outcrop. A) Shows the cataclasite relationship as well as the P'-fracture orientation of the cataclasite to the pseudotachylite GPPD. B) is a broader photograph of the outcrop from which photograph A) was taken. The white box indicates the position of A). See Figure 3.10 for photograph location. 54

Figure 3.33: A) PPL photomicrograph of the lower part of MHJL-002 thin section showing the contact of the overlying anorthosite with the underlying cataclasite. B) PPL photomicrograph the lower part of MHJL-008C thin section showing cataclasite and polycrystalline clasts of chromite-foliated anorthosite. 55

Figure 3.34: PPL photomicrograph of the MHJL-003 thin section showing the diffuse to gradational boundary of cataclasite with underlying breccia (dashed white line, see Chapter 4 for TIMA analyses of the various

clasts). Several polymineralic clasts of pseudotachylite, cataclasite and chromite-foliated anorthosite are evident (outlined in yellow). Clasts with cataclasite show fractures that crosscut the cataclasite at a high-angle. 56

Figure 3.35: Outcrop photographs of the various crosscutting relationships of fault rocks. A) shows pseudotachylite clasts within a younger pseudotachylite-cataclasite generation. B) shows a reverse-sense displacement shear fracture crosscutting two GPPDs. The lower GPPD is disrupted to a greater degree by crosscutting fractures than the upper GPPD. The lower surface of the upper GPPD is disrupted by normal-sense and reverse-sense shear fractures. The upper surface, however, is not crosscut by these fractures and neither is the overlying and crosscut cataclasite, implying the normal- and reverse-sense shear fractures were coeval to the generation of the upper GPPD as the fractures do not propagate into the pseudotachylite. See Figure 3.10 for photograph location. 58

Figure 3.36: Equal area stereoplot of the poles to pseudotachylite-absent fractures within the chromite-foliated anorthosite layer (n=33). The blue line is the average plane to magmatic layering. 59

Figure 3.37: Outcrop photograph of a dolerite dyke (Dol) terminating against the base of the chromite-foliated anorthosite (fl_{Chr} Ano). The dyke crosscuts the underlying pyroxenite (Pxt) and pyroxene-foliated (fl_{Px} Ano) base of the chromite-foliated anorthosite. 60

Figure 3.38: Equal area stereoplot of poles to fractures from the various lithologies outside the chromite-foliated anorthosite and chromite-foliated anorthosite fault. The blue, black, and green dots are poles to fractures in the pyroxene-foliated anorthosite (n=4), chromitites (n=6) and pyroxenites (n=27), respectively. The blue line is the average plane to magmatic layering. 61

Figure 3.39: Photomicrograph of pyroxene grains within norite in thin section MHJL-005B emphasizing the greater density of intracrystalline fractures within the pyroxene grains compared to the surrounding plagioclase grains. 62

Figure 3.40: Outcrop photograph of the LG-6 chromitite and crosscutting faults. The main SSW-dipping fault is traced by the dashed white line. A smaller fault, subparallel to the diggings wall is traced by the dotted white line (Expanded in Figure 3.43). See Figure 3.10 for location (UTM 35J 0793361 mE 7312893 mN) 63

Figure 3.41: Equal area stereoplot of orientation data from the reverse fault crosscutting the LG-6 chromitite, SSW-dipping fault (red line labelled f_{SSW}, dipping at 67°→206°) and slickenlines on the reverse fault

(black dot, dipping at 59°→176°), diggings wall-parallel fault (green line labelled f_W, dipping at 44°→260°) and average plane to magmatic layering (blue line labelled L_m). 64
Figure 3.42: Outcrop photograph of an injection vein extending from the reverse fault crosscutting the LG-6 chromitite. The injection vein extends horizontally northward into the footwall of the fault and is outlined by the dotted white lines. 65
Figure 3.43: Outcrop photograph of the diggings wall parallel fault, traced by the dashed white line. The fault crosscuts the LG-6 chromitite in the footwall of the SSW-dipping reverse fault. 65
Figure 3.44: Outcrop photograph of the layer-parallel and oblique-fractures within the LG-6 chromitite in the footwall of the reverse fault. The fault-parallel fracture is parallel to the W-dipping fault in Figure 3.43.. 66
Figure 3.45: Photomicrograph of the fault rocks within the main, SSW-dipping fault crosscutting the LG-6 (Figure 3.40) in thin section MHJL-023. The thin section displays quasi-ductile cataclasite (QCt) with sigmoidal chromite-aggregate fabric, fault-parallel shears, P' fractures and R fracture. A feldspathic pyroxenite (Pxt) clast is traced for comparison of intracrystalline fracturing of pyroxene and plagioclase. Epidote (Ep) is observed in the matrix surrounding the outlined pyroxenite clast. Note that north is obliquely inclined to the edges of the thin section. 67
Figure 3.46: Outcrop photograph of slickenlines on the top surface of a pseudotachylite GPPD. Several slickenlines are traced by the solid white lines. 68
Figure 3.47: Equal area stereoplot of slickenlines within the various lithologies exposed at Jagdlust Farm and surrounding study area. The black dots are slickenlines within the chromitites (n=4). The green triangles are slickenlines within the pyroxenites (n=4). The red dots are slickenlines within the chromite-foliated anorthosite; hollow dots are on fractures without pseudotachylite (n=13), solid red dots are on pseudotachylite-bearing fractures (n=19). The blue line is the average plane to magmatic layering. 68
Figure 3.48: Schematic diagram of the expected orientation of fractures forming between two paired GPPDs in a top-to-north fault zone, after Swanson (1988). R, R', P to P" and P' shears should dip at 15° N, 75° N, 20°-15° S and 30° N, respectively, for a top-to-north displacement sense (Logan, 1979; Swanson, 1988; Davis et al., 2000). 69
Figure 4.1: Comparison between the EDS spectra for the TIMA anorthite standard (A) and plagioclase from the chromite foliated anorthosite (B) and plagioclase from the pyroxene-foliated anorthosite (C). Plagioclase from the chromite foliated anorthosite has slight enrichment of Mg and minor amounts of Na. A large line spacing for the pyroxene-foliated anorthosite has resulted in the discrete data form of C. 71

Figure 4.2: Comparison between the EDS spectra for the TIMA xieite standard (chromite polymorph, orange) and chromite within the chromite-foliated anorthosite (black line). Chromite within the anorthosite has slight enrichment of Mg, Al and Si, which form a part of the chromite-spinel solid solution series (Liipo et al., 1994). Ca is also present in minor proportions within chromite in the sample set. 71
Figure 4.3: Comparison between the energy-dispersive spectroscopy spectra for the TIMA chlorite standard (A) and chlorites of various Mg proportions within the chromite-foliated anorthosite fault (B, C and D). The chlorite is likely chamosite with clinochlore solid solution (Brindley, 1949; Welch, 2004; Wu et al., 2019). 72
Figure 4.4: An example of the differences in textural and mineralogical detail of pseudotachylite, cataclasite and chloritization as revealed by optical microscopy (A), BSE imaging (B), phase mapping (C) and Fe-Mg-Cr composite elemental mapping (D). The images are of the only scanning area within the MHJL-009 thin section. See section 2.2.5 for (C) and (D) production methodology. 73
Figure 4.5: A section from the Fe-Mg-Cr elemental composite map of MHJL-001 scanning area A. The image shows the blebby-textured chloritization (bright green) and its association with magmatic chromite aggregates (purple). See section 2.2.5 for image production methodology. 74
Figure 4.6: A section from the Fe-Mg-Cr elemental composite map of MHJL-003 scanning area A. The image shows the webbed-textured chloritization (bright green). See section 2.2.5 for image production methodology. 75
Figure 4.7: A section from the Fe-Mg-Cr elemental composite map of MHJL-003 scanning area C. The image shows the flecked-texture chloritization (bright green). See section 2.2.5 for image production methodology. 76
Figure 4.8: Photomicrograph (A) and corresponding Fe-Mg-Cr composite map (B) of the MHJL-001 scanning area A. The composite element map shows the blebby-textured chloritization along foliation-oblique and foliation-parallel fractures. The blebby-textured chloritization typically grades into the webbed-textured chloritization away from magmatic chromite aggregates. The webbed-textured chloritization occurs along grain boundaries and foliation-parallel and foliation-oblique fractures. See section 2.2.5 for image production methodology. 77
Figure 4.9: A) Photomicrograph of foliation-parallel and foliation-oblique fractures within the chromite-foliated anorthosite and corresponding RGB composite elemental maps of B) Fe-Mg-Cr and C) Mg-Ca-Al. The images emphasize the distribution of chlorite along fractures as well as the relationship between the

webbed-textured chlorite, blebby-textured chlorite, and magmatic chromite aggregates. The images are of MHJL-001 scanning area B. See section 2.2.5 for B) and C) production methodology. 78
Figure 4.10: Photomicrograph (A), Fe-Mg-Cr composite map (B) and Mg-Ca-Al composite map (C) of MHJL-003 scanning area B. The images emphasize the chloritization textures (B) and clast-shape (C) within the quasi-ductile cataclasite and two generations of cataclasite. The quasi-ductile cataclasite and older cataclasite generation are within a clast of the younger cataclasite. The quasi-ductile cataclasite and older cataclasite generation have pervasive webbed-textured chlorite. The younger cataclasite has flecked-textured chloritization. A chromite-foliated anorthosite clast is also observed. This clast has a blebby-textured chloritization. The disaggregation of the anorthosite clast has produced the flecked texture. See section 2.2.5 for B) and C) production methodology. 79
Figure 4.11: Photomicrograph (A) and corresponding Fe-Mg-Cr composite map (B) showing the webbed-textured chloritization crosscutting pseudotachylite GPPDs (Pst) and injection veins within the breccia (Br) consisting of anorthosite (Ano) clasts. The pseudotachylite dykes are fractured to varying degrees with older generations forming clasts within cataclasite (Ct) associated with younger pseudotachylite generations. The more deformed pseudotachylites are crosscut by webbed-textured chloritization. It is unclear if the near-perpendicular fractures are associated with deformation or production of the thin section. The images are of the MHJL-006A thin section scanning area B. See section 2.2.5 for B) production methodology. 80
Figure 4.12: Photomicrograph (A) and corresponding Fe-Mg-Cr composite elemental map (B) showing the webbed-textured chloritization along the edges of a pseudotachylite injection vein. The chloritization also weakly pervades the crosscutting fractures, altering the pseudotachylite. The images are of MHJL-006A scanning area A. See section 2.2.5 for B) production methodology. 81
Figure 4.13: High exposure photomicrograph (A) of colour banding within a pseudotachylite (Pst) injection vein and corresponding Fe-Mg-Cr composite map (B). The colour composite map shows that the colour banding is neither the result of crosscutting chloritization nor compositional banding. The banding is presumed to be the result of grain size variation within the matrix. The injection vein crosscuts chromite-foliated anorthosite (Ano), cataclasite (Ct) and a chromitite (Chr) nodule. The images are of the only scanning area within the MHJL-008D thin section. See section 2.2.5 for B) production methodology. 82
Figure 4.14: Photomicrograph (A) and corresponding Fe-Mg-Cr composite elemental map (B) showing the webbed-textured (subscript W) and flecked-textured (subscript F) chloritization within clasts of cataclasite

(Ct), anorthosite (Ano) and pseudotachylite (Pst) within a cataclasite matrix. The images are of MHJL-003 scanning area C. See section 2.2.5 for B) production methodology. 83

Figure 5.1: Diagrammatic representation of the chromite-foliated anorthosite fault of the Jagdlust Farm fault system. The hangingwall is cohesive fault rock with slip occurring at the footwall-hangingwall interface. The footwall colour gradation represents clast-size distribution within the footwall, with the smallest clasts at the pseudotachylite GPPD (red). Slip within the footwall is distributed through the incohesive fault rock and decreases away from the footwall-hangingwall interface. 88

Figure 5.2: Simplified stratigraphy of the Bushveld Complex and the relationship thereof with the Transvaal Supergroup, Rooiberg Volcanics, Loskop Formation and Waterberg Group rocks, after von Gruenewaldt et al. (1985). The Bushveld Complex is estimated to be 8 km thick with an unknown amount of overburden at the time of emplacement. The dashed white line is the approximate stratigraphic level of the chromite-foliated anorthosite fault. Garnet geobarometry estimates greenschist facies pressures of 3-5 kbar at the base of the intrusion (Nel, 1984; Buick et al., 2000; Mavimbela, 2013). 90

Figure 5.3: Block model of the chromite-foliated anorthosite fault, Jagdlust Farm fault system. The σ_1, σ_2, σ_3, principal stress axes are oriented subhorizontal N-S, subhorizontal E-W and subvertical, respectively. The σ_2 stress axis was tensile and therefore produced N-S trending extensional shear fractures associated with layer-parallel extension. Layer-parallel shortening in the N-S direction produced south-dipping sigmoidal fabric and P fractures, and north-dipping R-R' fractures. 94

Figure 5.4: Fault development model for the chromite-foliated anorthosite fault. A) through C) sketch the initiation of the fault through to the development of sigmoidal-clast, quasi-ductile cataclasite. The transition from continuous cataclastic-flow to stick-slip occurs between C) and D). D) through F) sketch the development and chloritization of structures formed during stick-slip events. Chloritization is represented by a change in feature colour to light green. 97

Figure 5.5: A) Schematic diagram, after Grasemann et al. (2003) of an S-type flanking fold developing under a sinistral shear-sense. B) Schematic diagram, in plan-view, showing the relationship of the TML with the RLS and Transvaal Supergroup (TvS) rocks. Sinistral-shear, with up-throw of the northern block, along the TML, is thought to produce a regional S-type flanking fold within the RLS layering (approximate strike and dip-direction shown). Shearing is a response to the approximately NE-SW compression and NW-SE extension proposed by Du Plessis and Walraven (1990). The Wonderkop and Steelpoort faults are omitted from the diagram. C) West-facing, schematic cross-section of the TML and abutting down-thrown,

southern block with the RLS and Transvaal Supergroup rocks represented. The relationship of the chromite-foliated anorthosite fault and LG-6 reverse fault, as well as the Mhlapitsi Belt, are shown in relation to the TML. Layer steepening of the RLS and TvS rocks abutting the TML is expected with northern block up-throw through the development of an S-type flanking fold. 102

1 Introduction

The Rustenburg Layered Suite (RLS) forms the ultramafic-to-mafic portion of the Bushveld Complex (Clarke et al., 2005). The RLS has three of the five limbs exposed in outcrop, viz. the Northern, Western and Eastern Limbs (Schouwstra et al., 2000; Wilson, 2015). The Northern Limb of the RLS is separated from the Eastern and Western Limbs by the crustal-scale Thabazimbi-Murchison Lineament (TML) (Du Plessis and Walraven, 1990; McCourt, 1995; Clarke et al., 2009). The Eastern and Western Limbs of the RLS have a basin-like shape with the layering generally dipping ~10° centripetally (Cawthorn and Webb, 2001; Clarke et al., 2005; Perritt and Roberts, 2007; Roberts and Clark-Mostert, 2010), but anomalously steep dips are found locally within the Eastern Limb. Much of the local steepening within the Eastern Limb occurs on the flanks of syn-crystallization, buoyancy-driven, Transvaal Supergroup footwall diapirs (Gerya et al., 2003; Clarke et al., 2005; Clarke et al., 2009; Montjoie, 2018), and along a broader region of steep dips, approaching 60°, occurs along the Eastern Limb immediately south of the TML, indicating large-scale, post-magmatic rotation. Despite these features, comparatively little work has been done on the implications of such vertical movements for strain accommodation within the RLS rocks themselves, apart from Basson (2019), who proposes a model for the original shape of the Bushveld Complex, and , who propose that the centripetal dip of the Western and Eastern Limbs is the result of flexural-slip folding induced by lithostatic loading and accommodated through the development of a suite of centripetally-dipping, reverse-slip, layer-parallel faults along chromitite contacts and connected by ramp faults.

This study focuses on a pseudotachylite-bearing fault system exposed in outcrop and recent artisanal diggings on Jagdlust Farm, in the northern portion of the Eastern Limb (Figure 1.1), southeast of the steeply-dipping margin of the RLS and a zone of intensely folded footwall rocks in the Mhlapitsi Belt, a subsection of the TML (McCourt, 1995; Basson, 2019). It aims to characterise the fault rocks and their structural features and relationships to establish the strain evolution and kinematics of the fault system, which are used to evaluate the origin of the fault system with respect to the deformation history of the Bushveld Complex.

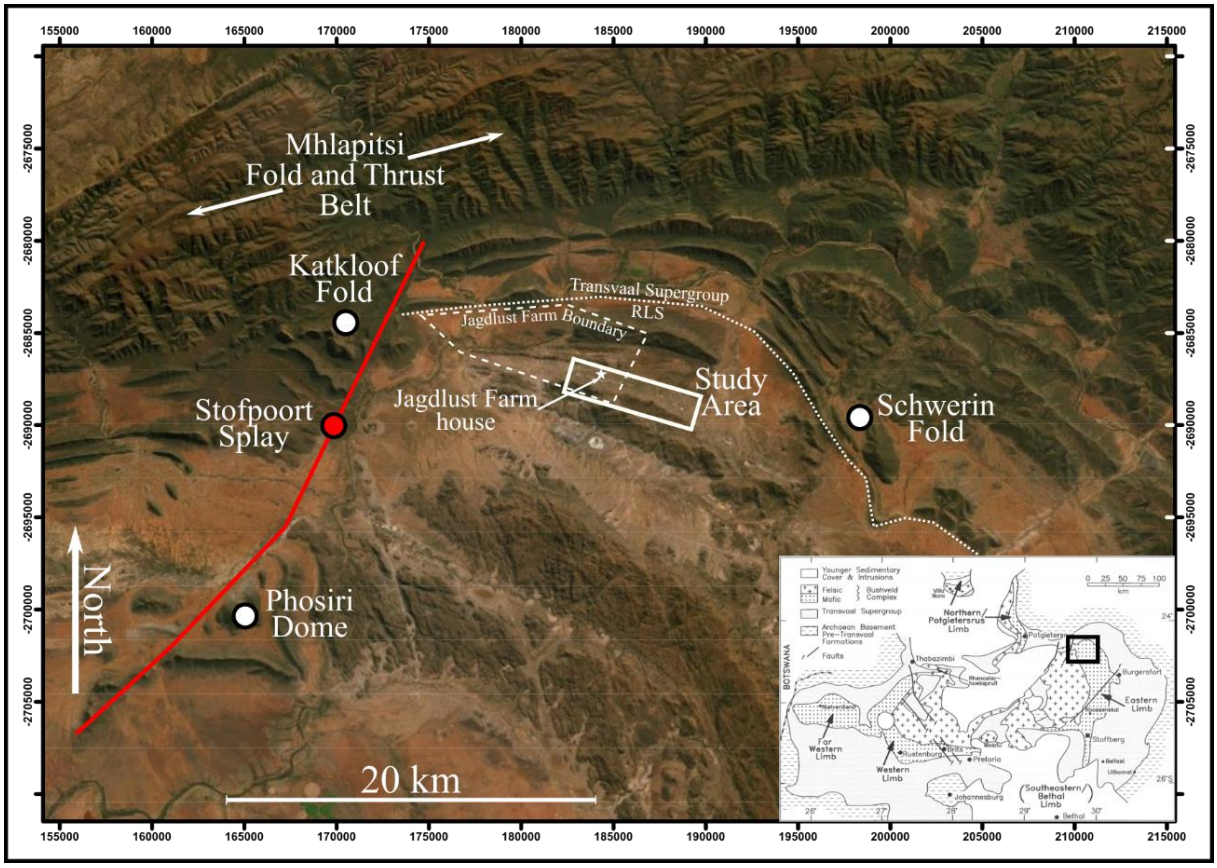


Figure 1.1: Satellite imagery of the northern portion of the Eastern Limb of the Bushveld Complex showing the study area, Jagdlust Farm boundary and house and several significant geological features (Esri, 23 June 2013). The overview map is a schematic map of the Bushveld Complex, Transvaal Supergroup and Archaean Basement from Eales and Cawthorn (1996) (see Figure 1.2). The black box shows the extent of the Satellite image. UTM Grid 35J (Esri, 23 June 2013).

1.1 The Bushveld Complex

The Bushveld Complex in South Africa is a Paleoproterozoic (ca. 2.061-2055 Ga) ultramafic-mafic-felsic layered intrusion (Eales and Cawthorn, 1996; Buick et al., 2001; Scoates and Wall, 2015; Zeh et al., 2015). The Bushveld Complex covers an area of 70 000 km^2 and is divided into five limbs, viz.; Far Western, Western, Eastern, Northern and, Bethel (Southern) limbs (Figure 1.2) (Eales and Cawthorn, 1996; Schouwstra et al., 2000; Seabrook et al., 2005) reaching a maximum thickness of 9 km in places, making it the largest layered intrusion on earth (Schouwstra et al., 2000; Wilson, 2015).

The ultramafic-mafic portion of the intrusion, known as the Rustenburg Layered Suite (RLS), intruded the volcano-sedimentary Transvaal Supergroup, under pressures of 2-4 kbar (Nel, 1984; Uken, 1998; Buick et al., 2000; Mavimbela, 2013), as a series of elongated sills that expanded and interlocked with the introduction of new magma pulses over 75000 years (Eales and Cawthorn, 1996; Cawthorn and Walraven, 1998; Buick et al., 2001; Kruger, 2005; Clarke et al., 2009). Each new magma pulse is represented by a lithological cyclic unit (Cawthorn

and Walraven, 1998). These cyclic units are then grouped based on the appearance or disappearance of cumulate minerals and divide the RLS into five Zones, viz.; the Marginal, Lower, Critical, Main, and Upper Zones (Eales and Cawthorn, 1996; Schouwstra et al., 2000; Clarke et al., 2005; Kruger, 2005; Wilson, 2015).

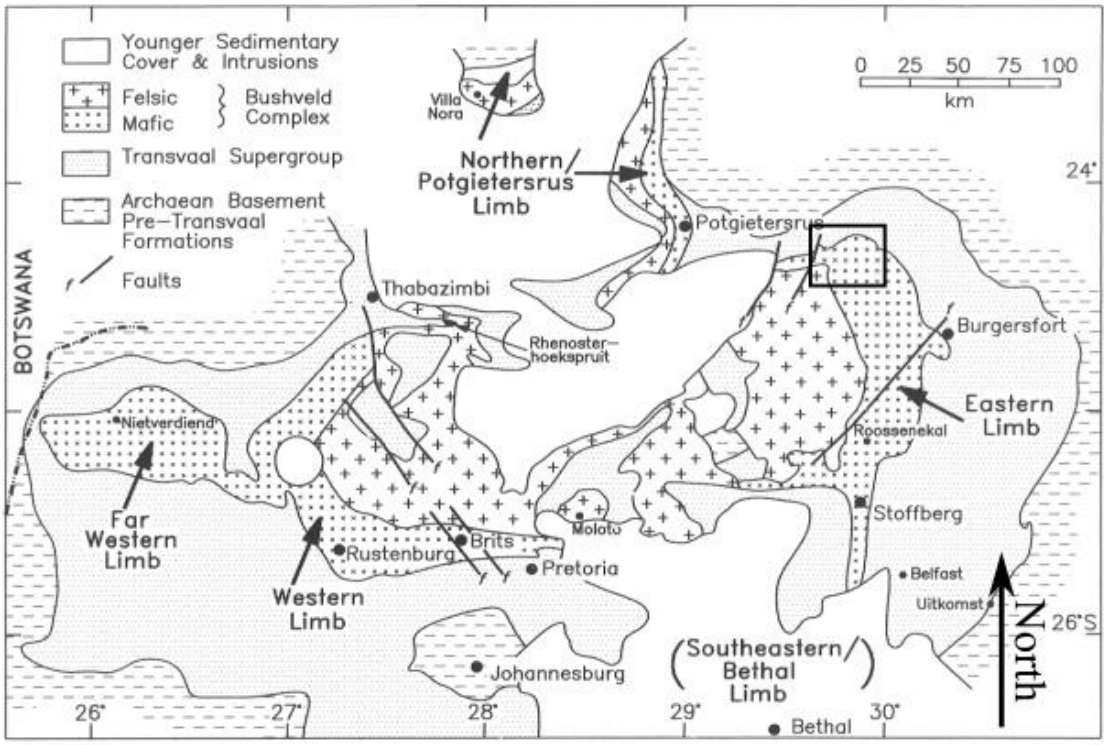


Figure 1.2: Schematic Map of the Bushveld Complex from Eales and Cawthorn (1996) showing the Northern, Eastern, Western, far Western and Southern limbs of the Bushveld Complex, as well as the mafic and felsic portion of the Bushveld Complex, Transvaal Supergroup and Archaean Basement. The black box shows the estimated extent of the Satellite image in Figure 1.1.

Of the five zones mentioned, the Critical Zone is the most economically significant as it hosts approximately half of the world's Platinum Group Elements (PGE's) as well as the world's largest chromium reserves in 13 chromitite seams (Seabrook et al., 2005; Schulte et al., 2010).

The Critical Zone consists of chromite-harzburgite-pyroxenite cycles and chromite-pyroxenite-norite-anorthosite cycles, with each new chromitite interpreted as a new magma influx (Figure 1.3) (Eales and Cawthorn, 1996; Seabrook et al., 2005; Mondal and Mathez, 2006). The chromitites are clustered in three stratigraphic levels within the Critical Zone; towards the base of the Zone is a cluster of seven, which are called the Lower Group chromitites (LG 1-7), towards the Merensky Reef is a cluster of two called the Upper Group chromitites (UG 1&2), and a cluster of four seams found between the LG and UG chromitites, which are called the Middle Group chromitites (MG 1-4) (Eales and Cawthorn, 1996; Cawthorn and Walraven, 1998; Schulte et al., 2010).

The MG chromitites are found at the upper-lower Critical Zone boundary, with the MG2 dividing the sub-zones (Cameron, 1963; Eales and Cawthorn, 1996; Cawthorn and Walraven, 1998; Schulte et al., 2010). This distinction between the upper and lower Critical Zone is based on the appearance of cumulate plagioclase, with rock sequences changing from chromitite-harzburgite-pyroxenite cycles of the lower Critical Zone (C_LZ) to chromitite-pyroxenite-norite-anorthosite cycles of the upper Critical Zone (C_UZ) (Eales and Cawthorn, 1996; Seabrook et al., 2005; Mondal and Mathez, 2006).

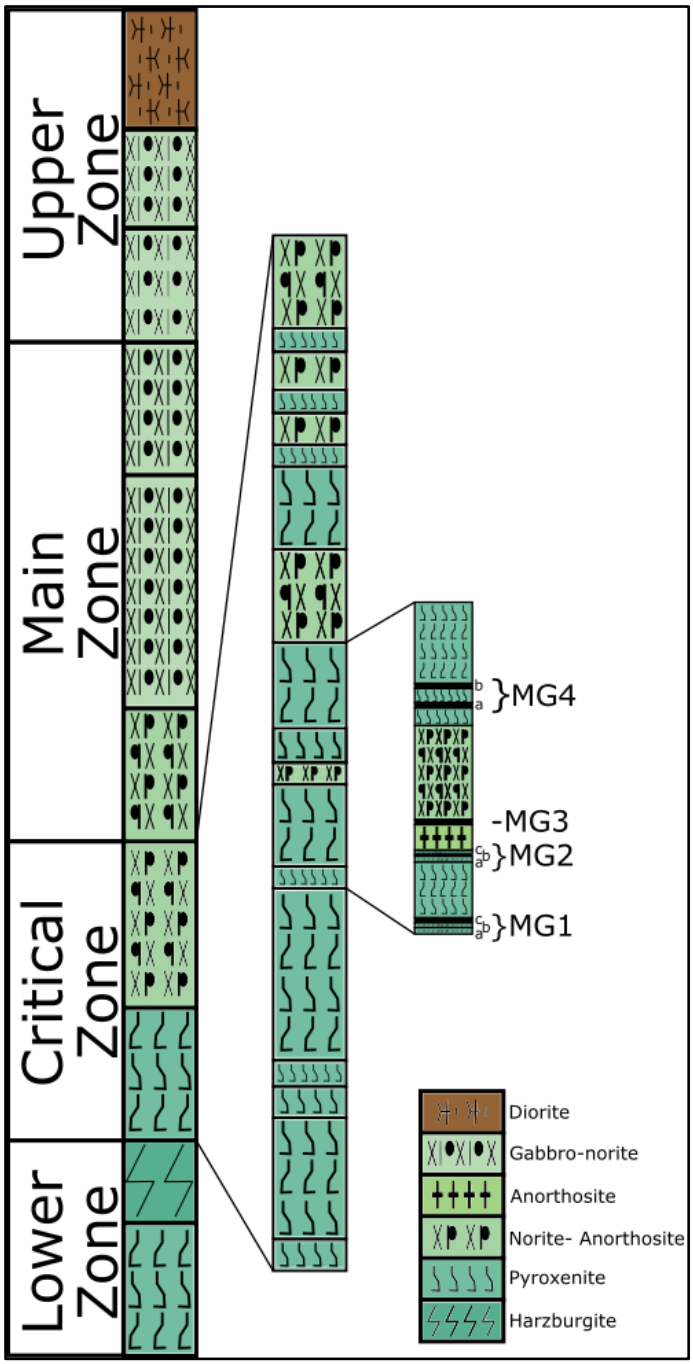


Figure 1.3: Stratigraphic column of the RLS with emphasis on the Critical Zone and Middle Group chromitites

(Eales and Cawthorn, 1996; Cawthorn and Walraven, 1998).

1.2 Deformation of Bushveld Complex and Transvaal Supergroup rocks

1.2.1 Diapirism

With the influx of hot ultramafic-mafic magmas into a cold sedimentary host sequence, a density and, consequently, a gravity contrast between the RLS and volcano-sedimentary footwall rocks was created (Gerya et al., 2003; Clarke et al., 2005). The hot RLS magmas heated the host rocks to amphibolite-granulite facies grades (500°C to >750°C), causing partial melting in the immediate footwall, which facilitated upward mobilization of the less dense floor rocks through the RLS as it cooled and crystallized (Buick et al., 2000; Gerya et al., 2003; Johnson et al., 2004; Clarke et al., 2005; Longridge et al., 2009). These diapirs are found both around the edges and within the RLS and typically have an asymmetrical cuspate to bulbous shape. Within the Eastern Limb, the majority of diapirs have NW-SE trending fold hinges (Du Plessis and Walraven, 1990; Gerya et al., 2003).

Within the limbs of the diapirs, layer-parallel extensional shear zones may form (Uken, 1998; Gerya et al., 2003; Clarke et al., 2005; Longridge et al., 2009). Furthermore, layers of the RLS surrounding the diapirs are thinned through extension, with deformation decreasing upward within the RLS sequence, indicating that the diapirs were active during the emplacement and crystallization processes (Uken, 1998; Cawthorn and Webb, 2001; Gerya et al., 2003; Clarke et al., 2005; Montjoie, 2018).

Near Jagdlust Farm are three such diapirs, viz.: the Katkloof and Schwerin Folds and Phosiri Dome. Both the Katkloof and Schwerin Folds are found on the margins of the RLS whereas the Phosiri Dome is an inlier of Transvaal sediments within the RLS (Sharpe and Chadwick, 1982; Uken, 1998; Scoon, 2002; Montjoie, 2018).

The Katkloof Fold is approximately 15 km west of Jagdlust Farm. The fold has a SSW-plunging axis about, which the western and eastern limbs are rotated (Sharpe and Chadwick, 1982; Uken, 1998). The western limb is more steeply dipping than the eastern limb, resulting in a SW-vergence. Parasitic folds with S-plunging axes deform both layering and quartz veining and are postdated by sinistral, N-S trending kind bands (Uken, 1998).

The Schwerin Fold is found 18km southeast of the Jagdlust Farm (Sharpe and Chadwick, 1982; Eales and Cawthorn, 1996). The fold is W-verging about the NW-SE axis (Uken, 1998; Longridge et al., 2009). A 100 m wide, south-dipping layer-parallel extensional shear zone is present within the southern limb (Longridge et al., 2009). Deformation within the shear zone is characterised by S- to SW-verging folds, W-E boudinage axes, and

NNW-SSE trending lineations, all of which indicate that the shear zone underwent north-south extension (Longridge et al., 2009).

The Phosiri Dome is approximately 25km southwest of Jagdlust Farm. The dome has the southern and eastern limbs rotated about a SE-plunging fold axis (Sharpe and Chadwick, 1982; Uken, 1998; Montjoie, 2018). The dome has a SW-vergence; the eastern limb is less-steeply dipping compared to the subvertical dip of the southern limb (Sharpe and Chadwick, 1982; Uken, 1998; Montjoie, 2018). Both limbs of the dome have parasitic folding and schistosity subparallel to the fold axis (Sharpe and Chadwick, 1982; Uken, 1998).

1.2.2 Flexural-slip folding induced by lithostatic loading

Owing to the similarity between the Eastern and Western Limbs of the Bushveld Complex, centripetal dip and palaeomagnetic data showing originally horizontal layering, it has been concluded that the Western and Eastern Limbs of the Bushveld Complex are connected at depth and the current orientations of the layering are the result of post-crystallization processes (Cawthorn and Webb, 2001; Clarke et al., 2005; Perritt and Roberts, 2007; Roberts and Clark-Mostert, 2010). Lithostatic loading of the crust, owing to the density and volume of the RLS, was proposed to be the cause for the cylindrical folding of the Bushveld Complex, producing the centripetal dips of the RLS layering within the Western and Eastern Limbs (Cawthorn and Webb, 2001; Clarke et al., 2005; Perritt and Roberts, 2007; Roberts and Clark-Mostert, 2010). Perritt and Roberts (2007), studying structures at Kroondal, Horizon and Helena chrome mines concluded that flexural slip, after the model by Tanner (1989), was the mechanism by which folding occurred; reverse-sense displacement, layer-parallel faults connected by ramp duplexes.

Both the layer-parallel and ramp faults have reverse-sense displacement and centripetally-plunging slickenlines, indicating dip-slip movement (Perritt and Roberts, 2007). Displacement along the ramp faults does not exceed 10 cm and is typically <1 cm (Perritt and Roberts, 2007). The faults range from sharp, polished surfaces to 5 cm thick zones with altered fault-gouge infill (Perritt and Roberts, 2007).

1.2.3 Regional stress field

The Bushveld Complex is transected by the Thabazimbi-Murchison Lineament (TML), an east-northeast-trending crustal lineament (Du Plessis and Walraven, 1990; McCourt, 1995; Clarke et al., 2009). This lineament was reactivated during and immediately after the emplacement of the RLS by a N-S to NE-SW primary compressive stress axis orientation (Figure 1.4) (Du Plessis and Walraven, 1990; McCourt, 1995; Basson, 2019). This stress

orientation resulted in sinistral movement along the TML and uplift of the northern block (Du Plessis and Walraven, 1990; De Wit and Good, 1997; Basson, 2019). The movement was accompanied by the development of south-verging thrusting and the activation of several major Transvaal Supergroup and Bushveld Complex crosscutting fault systems, viz. the Wonderkop, Steelpoort and Rustenburg faults, in a strike-slip manner (Molyneux and Klinkert, 1978; Bumby et al., 1998; Uken, 1998; Basson, 2019). Furthermore, Transvaal footwall diapirs, which developed in response to the emplacement of the hot, dense, ultramafic-mafic magmas inherited N-S to NW-SE trending fold axes (Du Plessis and Walraven, 1990; Hartzer, 1995; Gerya et al., 2003; Clarke et al., 2005; Clarke et al., 2009).

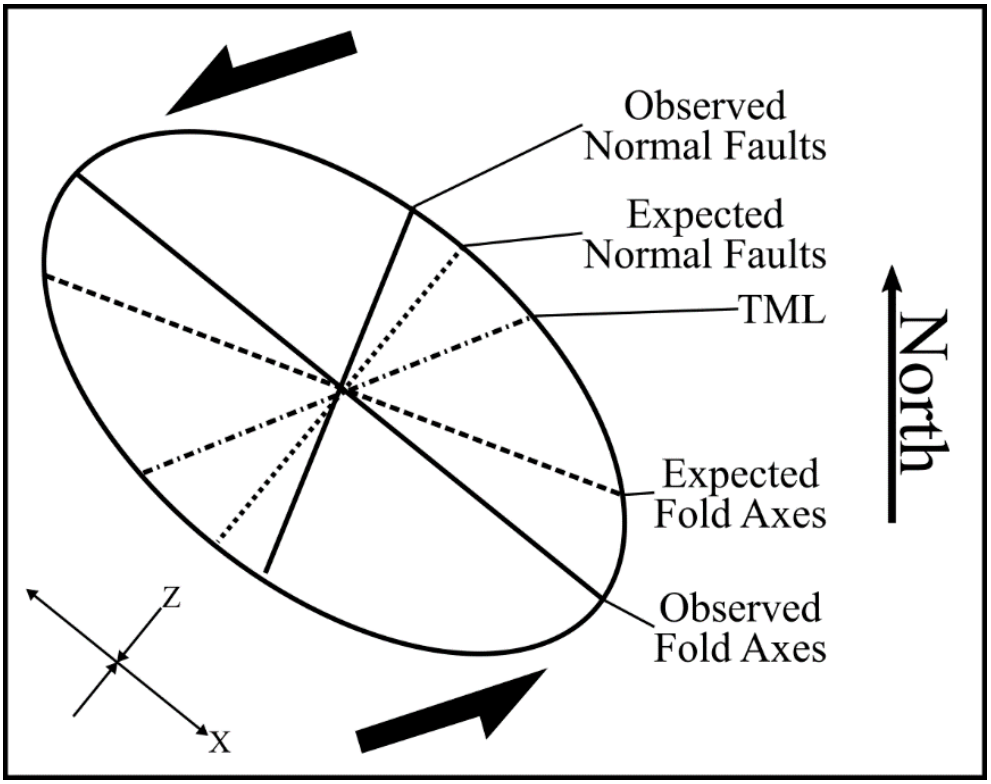


Figure 1.4: Regional stress field as proposed by Du Plessis and Walraven (1990) showing the observed and expected structures within the Eastern Limb of the Bushveld Complex. The stress field is proposed to have a NE-SW primary compressive stress axis, which re-activated the TML in a sinistral-sense; developing NW-trending fold axes and NNE-trending normal-faults such as the Wonderkop fault (Du Plessis and Walraven, 1990; Basson, 2019).

In the northern and central portions of the Eastern Limb, this stress field caused normal to sinistral-slip along faults parallel to the Wonderkop fault, as well as dextral-slip along the Steelpoort fault and Wonderkop conjugates (Molyneux and Klinkert, 1978; Uken, 1998; Basson, 2019). Furthermore, directly north of Jagdlust Farm is the Mhlapitsi Belt; a north-verging fold and thrust belt within the TML (McCourt, 1995; Basson, 2019). Within this belt, normal faults were reactivated, post-Bushveld Complex emplacement, in a top-to-north reverse sense,

steepening the layering of both the Transvaal Supergroup and Bushveld Complex rocks within the northern portion of the Eastern Limb (McCourt, 1995; Basson, 2019)

1.3 Occurrence and development of pseudotachylite

Pseudotachylite is an intrusive melt rock associated with high slip-rate brittle failure (Higgins, 1971; Sibson, 1975; Spray, 1995). It resembles tachylyte, an igneous glass, but differs in that it forms from the rapid frictional heating by seismic faulting and quenching of the melt (Higgins, 1971; Spray, 1995; Bjørnerud and Magloughlin, 2004; Jerram and Petford, 2011). Pseudotachylite is believed to develop at the brittle-ductile (B-D) transition due to the coincidence of the B-D transition with the seismogenic zone (Sibson, 1975; Sibson, 1977; Spray, 1995). The transition typically occurs at depths of approximately 10 km for quartzo-feldspathic rock, under a normal geothermal gradient, however, consideration must be given to the mafic-ultramafic composition of the RLS as well as the geothermal gradient during the cooling history of the Bushveld Complex as pseudotachylite has been known to form at both shallower and deeper crustal levels where compositional variation and high strain rates facilitate coseismic slip (Sibson, 1975; Sibson, 1977; Maddock et al., 1987; Spray, 1995)

1.3.1 Prerequisites for formation

The formation of pseudotachylite requires several conditions to be met before friction melting of the rock can occur, viz.: high slip-rate, comminution, low pore fluid pressure and a high content of hydrous phases (Philpotts, 1964; Sibson, 1975; Spray, 1995; Bjørnerud and Magloughlin, 2004; Passchier and Trouw, 2005; Bjørnerud, 2010).

In order for friction melting to occur, the slip-rate needs to be $\geq$10 $cm \cdot s^{-1}$ so as to overcome the rate at which heat is diffused through the rock by advection and conduction (Sibson, 1975; Bjørnerud and Magloughlin, 2004). As such, the presence of pseudotachylite is typically used as the indicator for coseismic slip (Sibson, 1975; Sibson, 1977; Bjørnerud and Magloughlin, 2004; Rowe and Griffith, 2015). However, frictional heating is only one mechanism by which elastic energy is released during faulting, therefore, it is possible to infer seismic-slip velocities from other fault features, e.g. injection veins or silica gels (Sibson, 1977; Pittarello et al., 2008; Faulkner et al., 2010; Faber et al., 2014; Rowe and Griffith, 2015).

During seismic-slip events, coseismic comminution facilitates the generation of pseudotachylite through the reduction of grain size (Allen, 1979; Magloughlin, 1989; Spray, 1995; Bjørnerud, 2010). This is because comminution increases the surface area within the fault zone, allowing for greater frictional heat production, and

the generated heat is distributed over a smaller volume of rock (Allen, 1979; Spray, 1995; Lin and Shimamoto, 1998; Bjørnerud and Magloughlin, 2004).

Historically it was thought that pseudotachylite could not form in incohesive comminuted rocks (Allen, 1979; Magloughlin, 1989; Spray, 1995; Bjørnerud, 2010; Rowe and Griffith, 2015), however, Bjørnerud (2010) has argued that comminution during earlier faulting events in rocks with high pore fluid pressure may assist in pseudotachylite formation, as comminution allows for the draining of fluids through increased permeability, which in turn allows for greater strain energy to be stored in the rock.

High pore fluid pressure prevents the formation of pseudotachylite by lowering the effective stress, causing the premature release of stored strain energy and lowering the slip-rate (Sibson, 1975; Allen, 1979; Passchier and Trouw, 2005; Bjørnerud, 2010). Conversely, the growth of hydrous minerals is favourable as these minerals seal the fault and act as a flux, facilitating the melting of dry minerals, during seismic-slip events (Sibson, 1975; Allen, 1979; Manatschal, 1999; Passchier and Trouw, 2005; Bjørnerud, 2010; Caine et al., 2010).

1.3.2 Formation process

Should the conditions at which faulting occurs be suitable for the generation of pseudotachylite; formation would proceed as follows:

1. Strain is stored in the rock as elastic energy, which is concentrated around heterogeneities, whether they be pre-existing microfractures or lenses of competency heterogeneity (Sibson, 1975; Sibson, 1977; Magloughlin, 1989; Bjørnerud and Magloughlin, 2004).
2. Elastic energy is released primarily as heat and slip (Pittarello et al., 2008; Newman and Ashley Griffith, 2014). The slip results in comminution, with latent and frictional heat melting the smaller comminuted material (Sibson, 1975; Allen, 1979; Bjørnerud and Magloughlin, 2004).
3. The generated pseudotachylite is transported away from the fault surface through a pressure gradient, allowing for the continued formation of pseudotachylite by maintaining frictional contact on the fault surface (Bjørnerud and Magloughlin, 2004). Further generation of friction melt is accommodated through the transport of pre-existing melt into dilational jogs (Higgins, 1971; Spray, 1995; Bjørnerud and Magloughlin, 2004).
4. The friction melt quenches in a matter of seconds to minutes, forming pseudotachylite and sealing the fault; resetting the seismic cycle (Sibson, 1975; Allen, 1979; Macaudière and Brown, 1982; Magloughlin, 1989; Spray, 1995; Bjørnerud, 2010).

1.3.3 Form of occurrence

Owing to the relationship of pseudotachylite with structural features, the form of pseudotachylite is easily recognisable. Generation plane-parallel dykes (GPPDs) of pseudotachylite are planar to sinusoidal dykes within the fault zone in which the pseudotachylite formed (Sibson, 1975; Passchier and Trouw, 2005). As the orientation of GPPDs is typically controlled by competency heterogeneity within the host rock, e.g. layering or metamorphic fabrics (Sibson, 1975; Sibson, 1985; Sibson and Toy, 2006; Bjørnerud, 2010), they form subparallel to parallel to the controlling feature and are therefore described as being concordant (Sibson, 1975). Extending from the GPPDs, often preferentially in one direction, are discordant injection veins (Sibson, 1975; Passchier and Trouw, 2005; Bjørnerud, 2010). These veins act as sinks, into which the generated melt is transported and stored (Higgins, 1971; Spray, 1995; Bjørnerud and Magloughlin, 2004).

Based on work in the Nasson Terrane, USA, Magloughlin (1989) describes six forms of generation surfaces for pseudotachylite (Figure 1.5). Type 1 are discontinuous dykes forming within a tabular zone of fractures parallel to foliation. Type 2 is a laterally extensive planar sheet with convex lenses and injection veins protruding off the GPPD. Types 3 and 4 consist of two, paired GPPDs bounding a continuum between an injection vein network within a deformation zone and a pseudotachylite-supported breccia, respectively. Type 5 is non-planar to sinuous with injection veins. Type 6 forms through multiple slip events; each successive event produces pseudotachylite in the form of types 2 through 4, producing a complex zone of crosscutting GPPD and injection vein relationships.

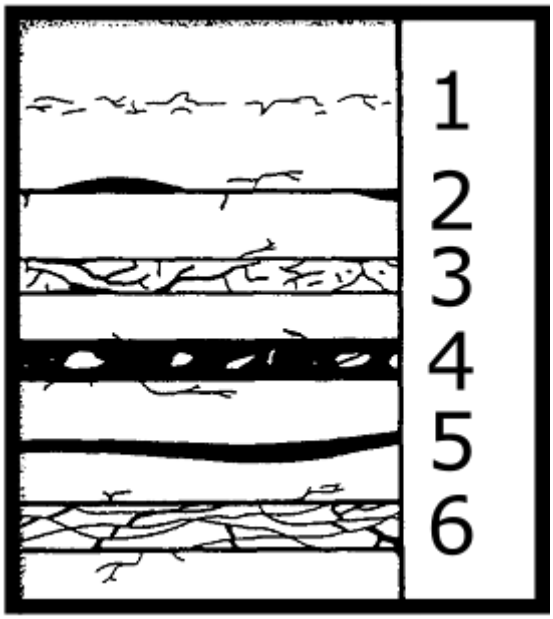


Figure 1.5: The 6 forms of pseudotachylite as described by Magloughlin (1989) in the Nason terrane, USA. Type 1 are discontinuous pseudotachylite-filled, irregular fractures. Type 2 are planar sheets with lenses and injection veins. Type 3 and 4 form a continuum of injection vein network and pseudotachylite supported breccia. Type 5 are sinusoidal sheets of pseudotachylite. Type 6 form by the reactivation and overprinting of Types 1 through 5.

More detailed work was done by Logan (1979) on the fracture patterns internal to the GPPDs. This work was later refined and expanded by Swanson (1988) and Davis et al. (2000). Logan (1979) began fault gouge studies with a series of experiments on various gouge mineralogies at increasing temperatures. The study found that several fracture sets developed post-Riedel shear and T_1 tension gashes formation (Figure 1.6). These fractures were later studied in greater detail by Swanson (1988) who grouped them into contractional and extensional slab-duplexes. In a horizontal, dextral system, contractional slab duplexes produced reverse-sense displacement P, P' and P* fractures at 15-20° from the GPPDs (Figure 1.6) (Logan, 1979; Swanson, 1988). The P-set fractures are accompanied by T_3 tension gashes (labelled Y-shears where slip occurs), which are parallel to the GPPDs (Figure 1.6) (Swanson, 1988). By comparison, extensional slab-duplexes form an X fracture set with T_2 tension gashes (Figure 1.6) (Logan, 1979; Swanson, 1988). The X and X' fractures form at 70-75° to the GPPDs and the T_2 is perpendicular to these surfaces (Figure 1.6) (Swanson, 1988).

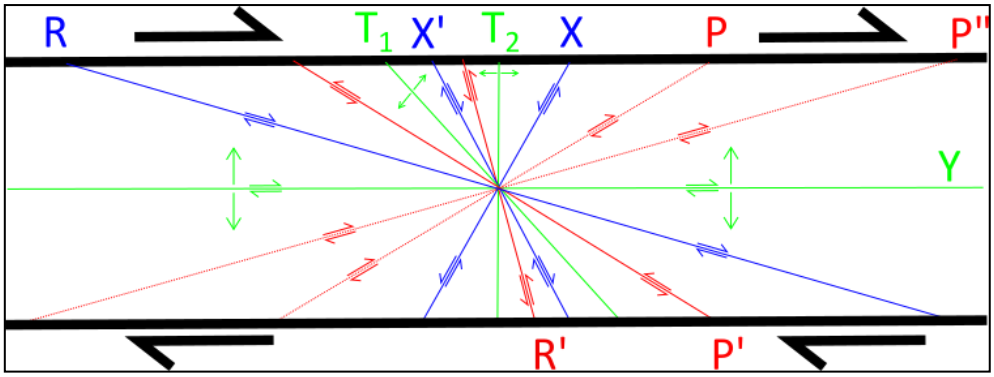


Figure 1.6: Fracture sets forming internal to the paired-planar generation surfaces. P, P', P" and T_3 fractures form in contractional slab-duplexes. X, X' and T_2 fractures form in extensional slab-duplexes. Blue, red, and green indicate normal-slip, reverse-slip, and fracture opening, respectively.

1.3.4 Indicators of friction melt production

True pseudotachylite is defined as a friction melt and ideally occurs as a melt-quenched glass (Allen, 1979). However, as the conditions at which most pseudotachylite forms are unfavourable to glass preservation, several features and textures have been used to distinguish the presence of quenched friction melt pseudotachylite from ultramylonites and ultracataclasites (Higgins, 1971; Sibson, 1975; Magloughlin, 1989; Bjørnerud and Magloughlin, 2004):

- Clasts, particularly quartz and feldspar, hosted in the fine-grained pseudotachylite matrix are common (Higgins, 1971; Bjørnerud and Magloughlin, 2004; Passchier and Trouw, 2005).
- Microlitic textures form where the cooling rate is slower. These textures appear as acicular, skeletal or dendritic crystal structures and may have flow structures around embayed clasts (Higgins, 1971; Sibson, 1975; Bjørnerud and Magloughlin, 2004; Passchier and Trouw, 2005).
- Where cooling rates were rapid enough to preserve glass, but ambient conditions were not conducive to preservation, devitrification structures may be present as spherulites that nucleate on clasts or other inclusions (Allen, 1979; Lin, 1994b, a; Passchier and Trouw, 2005).
- Degassing structures may also be present depending on the fluxing volatile content (Higgins, 1971; Maddock et al., 1987).
- As smaller clasts are incorporated into melts preferentially, the lack of a log-normal clast distribution suggests the presence of a melt phase (Evans, 1988; Ray, 2004; Lin, 2008; Pittarello et al., 2008). Furthermore, as melting is in disequilibrium, phases with lower solidus temperatures are preferentially

melted, producing higher proportions of monomineralic clasts with higher solidus temperatures (Higgins, 1971; Sibson, 1975; Allen, 1979; Fabbri et al., 2000).

1.3.5 Melting temperatures for common Critical Zone minerals

Friction melts produced during coseismic slip form from disequilibrium melting of the minerals at the fault surface (Allen, 1979). Minerals at the fault surface melt independently and the bulk composition of the melt will not follow partial melting compositions (Higgins, 1971; Sibson, 1975; Allen, 1979; Fabbri et al., 2000). Therefore, pseudotachylite within GPPDs often displays a similar, if not identical, composition to the host rock composition (Higgins, 1971; Sibson, 1975; Allen, 1979). As such, it is unwise to ascribe conventional bulk-rock melting temperatures to explain melting as the melt is not in equilibrium with the wallrock, as temperatures may differ based on fluxing and comminution of the host material (Allen, 1979). However, it is useful to know the common melting temperatures of the minerals present, as the order and degree of melting and fusion are the same as increasing melting temperatures (Sibson, 1975).

Common minerals found within the Critical Zone include chromite, plagioclase and pyroxenes (Eales and Cawthorn, 1996). Experimental melting temperatures for chromite in basalts range from 1170 °C to 1400 °C, depending on the melt composition, oxygen fugacity and pressure (Roeder and Reynolds, 1991; Feig et al., 2006, 2010), however, the melting temperature for pure chromite is 2265°C (Keith, 1954; Irvine, 2015) but may range between 2130°C and 2350°C depending on the MgO-CaO-FeO solid solution content (Glasser and Osborn, 1958; Muan and Sömiya, 1959, 1960). Feldspar melting temperatures range from 1100 °C to 1500 °C (Passchier and Trouw, 2005) and, more specifically, plagioclase ranges from 1095 °C to 1400 °C for An_{32} to An_{89} compositions respectively (Drake, 1976). Pyroxenes, overall, have a similar melting temperature range as plagioclase (Passchier and Trouw, 2005). The crystallization temperature, and subsequently melting temperature, for pure diopside and enstatite is 1392°C and 1557°C respectively (Morse, 1980).

As hydrous phases may act as a flux during frictional melting it is important to note the melting temperatures for hydrous phases that would be expected from the alteration of common Critical Zone minerals (Sibson, 1975; Allen, 1979). These alteration products may include epidote, chlorite and biotite (see Ferry (1979) for reactions and pathways). Using a friction welding apparatus, Spray (1992) showed that biotite undergoes disequilibrium friction melting at ~650°C. Epidote decomposes at ~1000°C however, this was determined under atmospheric oxidizing conditions (Vance and Routcliffe, 1976). There is no data available for chlorite group minerals,

however, comparable temperatures to biotite are expected as chlorite becomes unstable and dehydrates at ~600°C (Battaglia, 1999; Vigneresse, 2004; Wu et al., 2019).

2 Scientific Procedure

2.1 Hypotheses, Aim and Objectives

2.1.1 Hypotheses

- Pseudotachylite is present in the Jagdlust Farm chromite-foliated anorthosite fault.
- Pseudotachylite was formed in a layer-parallel fault system associated with post-Bushveld Complex tectonism.
- The pseudotachylite was generated under brittle-ductile transition P-T conditions.
- Alteration within the fault is a consequence of the post-faulting channelling of fluids along the fault-related fracture-network.

2.1.2 Aim

The aims of this study were threefold:

First, to describe the structures and kinematics of a prominent layer-parallel fault exposed at Jagdlust Farm.

Second, to determine the presence and extent of pseudotachylite within the layer-parallel fault. This included determining the number of likely coseismic slip events, the P-T conditions at which they occurred and the relative timing of individual structures within the fault.

Third, to determine the significance of the fault within the context of the Bushveld Complex structural evolution.

2.1.3 Objectives

Using field, petrographic, and analytical techniques the objectives for this study are to:

- Describe the structural features.
- Deduce fault kinematics from structural features.
- Determine the lateral and stratigraphic extent of the fault.
- Describe any lateral and vertical variation in strain-distribution within the fault.
- Describe the form, composition, and petrography of the pseudotachylite-bearing features to establish the provenance and age-relations to other structural features.

2.2 Methodology

2.2.1 Regional lineament desktop study

A preliminary regional lineament analysis was conducted on the northern portion of the Eastern Limb. Rather than produce a comprehensive analysis of the greater study area, like that produced by Greyvensteyn (2001) and Basson (2019), the purpose of the desktop survey was to contextualize the structures within the Jagdlust fault system.

This analysis was done using the Google Earth Pro path tool, visually tracing lineaments within the greater study area. The bearing of the individual lineament traces was measured using the ruler tool and plotted onto a Rose diagram using GeoRose 0.5.1. The lineament traces were imported into ArcGIS 10.1 and added to hyperspectral and Satellite imagery base maps. Despite using various hyperspectral composite maps, the sense of displacement along the lineaments could not be ascertained.

2.2.2 Field Mapping and Sample Collection

Mapping methodology

Fieldwork was conducted over two, three-day trips in 2018, the first in April and the second in September. The purpose of the trips was to map the outcrop extent of the chromite-foliated anorthosite fault, record structural data and collect representative samples. Mapping was done using a Garmin eTrex20 GPS (3 m accuracy) and the data were recorded under the following titles: Waypoint number, GPS data (UTM Zone 35S), Feature, Plane Orientation, Lineation Orientation, Displacement sense, Colour and Thickness of Pseudotachylite and Additional Notes. Structural data were collected, using a Silva Expedition 15TDCL and Brunton TruArc15, as dip-angle and dip-direction for plane orientation and plunge and trend for lineation orientation.

Sample collection

During the first fieldwork trip, 22 samples were collected from the Jagdlust Farm and adjacent properties. Of the 22 samples, 17 were from the chromite-foliated anorthosite fault, 2 were from undeformed anorthosite, 2 were from the pyroxenites underlying the layer-parallel fault, and 1 was of the fault-gouge within the reverse fault crosscutting the LG-6 chromitite. Sampling locations are shown in Figure 2.1 with the descriptions of the samples in Appendix A.

Fault zone samples were selected based on feature representivity and relationships between the features. The undeformed anorthosite and pyroxenites were sampled to provide a standard for comparison with the anorthositic

fault rocks. Where possible, the samples were taken in situ and oriented to north and/or horizontal. Where float samples were collected, the sample was collected either owing to poor outcrop or the sample displayed features and relationships not represented by in situ samples.

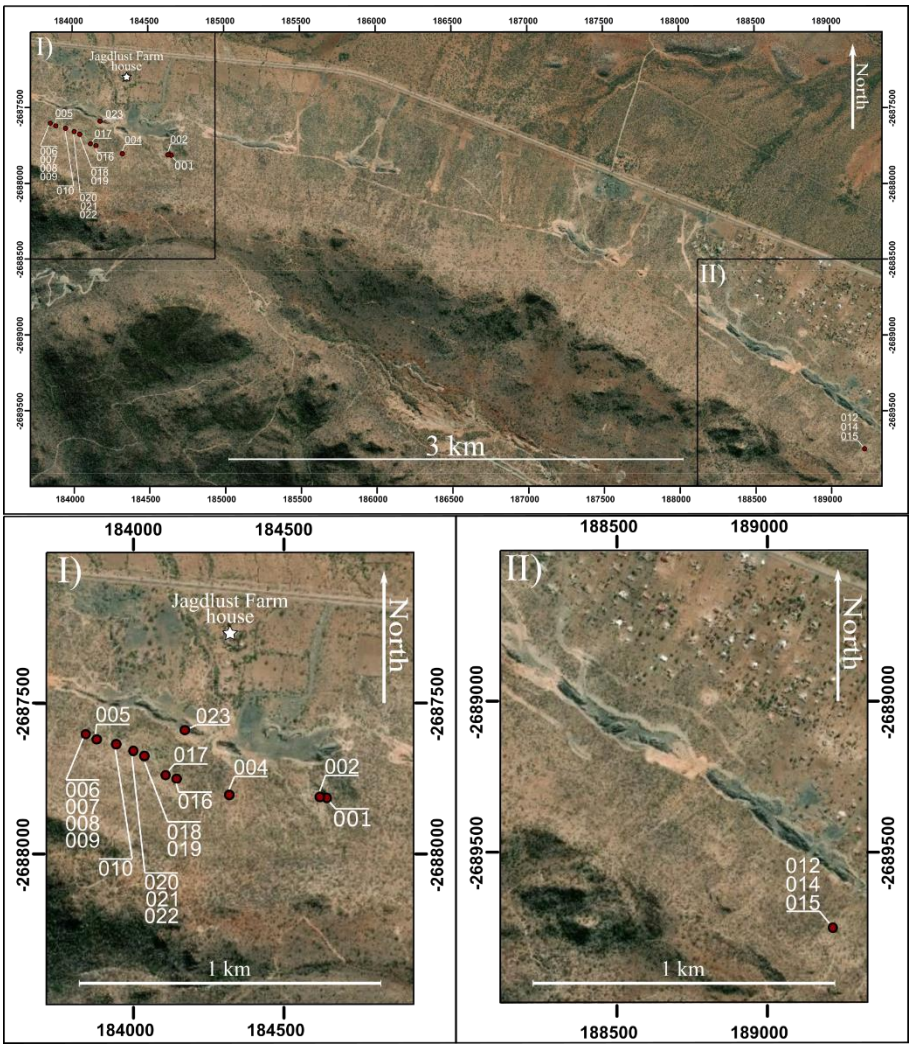


Figure 2.1: Satellite imagery of the study area with sample localities. The areas I) and II) are enlarged from the respective areas delineated on the base map. UTM Grid 35J (Esri, 23 June 2013).

2.2.3 Data processing and sample preparation

Field data processing

Field data were processed using MS Excel, grouping data based on lithology and structural orientation (All plane orientations are given as dip-angle → dip-direction). These data were then imported into ArcGIS 10.1, Stereonet 9.9.4 and GeoRose 0.5.1. These programs were used to produce structural maps, stereoplots and Rose plots, respectively. Furthermore, Stereonet 9.9.4 was used to calculate the angle between poles and planes as well as the conical best fit for pole groups. Equal-area, southern-hemisphere stereoplots were used in all instances.

All base maps are from Esri World Imagery, High-Resolution 30 cm Imagery base map as of 06 Jan 2020. The scale is defined for each image separately. The imagery was last accessed on 30 Jan 2020 at http://www.arcgis.com/home/item.html?id=10df2279f9684e4a9f6a7f08febac2a9

Sample preparation

After the first field trip, samples were described and photographed (Appendix A), with unoriented samples given a relative up direction. From the 22 samples, 16 were selected for thin section production. Lineated samples where cut parallel to lineation and perpendicular to the layer-parallel shear fracture. Oriented samples without a lineation were cut along an N-S profile and, where present, perpendicular to the layer-parallel shear fracture. Unoriented samples with no lineation where cut perpendicular to the layer-parallel shear fracture and parallel to an estimated movement direction, which was based on 3D analysis of the sample. Cut surfaces of the samples were then photographed and described.

Of the 16 samples selected for thin section production, 7 large (26×76 mm) and 14 regular (27×46 mm) thin sections were produced from 13 samples. Owing to the friability of many samples, 3 samples were destroyed and rendered unusable for thin section production and several other samples fragmented, losing feature representativity and relations. All thin sections are double polished, uncovered thin sections. The thin section size was chosen based on sample size and feature representativity.

2.2.4 Microscopy

Following thin section production, all sections were reoriented with respect to the remaining hand sample, ensuring correct orientation for structural descriptions. Thin sections were then photographed with high and low exposure plane-polarized light (PPL), cross-polarized light (XPL) and reflected light (RL) using an Olympus BX-63 microscope. Thin section descriptions and PPL photographs accompany the hand sample descriptions in Appendix A.

In conjunction with the thin section photographs, a Leitz Laborlux 11 Pol microscope was used for the petrographic studies. High exposure PPL photomicrography was used to describe pseudotachylite and alteration textures whereas low exposure PPL photomicrography was used to describe mineral and host rock form and textures. XPL was used for mineral identification, determining grain and clast sizes, and differentiating between clasts and matrix. Owing to variation in production method, RL was only used to describe chromite clast textures and qualitative description of alteration and fracture distribution within regular-sized thin sections. Features were initially described using a relative position in the thin section rather than an interpreted order of formation,

however, crosscutting relationships were noted after feature descriptions. Feature orientations within the sections were measured on A5 printed, full section photographs.

2.2.5 TESCAN Integrated Mineral Analyser data processing

The TESCAN Integrated Mineral Analyser (TIMA) is an SEM-based instrument capable of energy-dispersive spectroscopy (EDS) and measurement of back-scattered electrons (BSE) (Hrstka et al., 2018). These functions enable the instrument to produce elemental and phase maps; for a comprehensive detailing of the processes by which these are produced and other functions, capabilities and outputs of the TIMA system, see Hrstka et al. (2018).

Owing to the stage type in the Wits Automated Mineralogy Laboratory TIMA, only regular-sized thin sections could be selected analysis. Of the 14 regular thin sections produced, 10 scanning areas from 6 samples were selected for analysis. Samples from within the chromite-foliated anorthosite fault displaying significant fault rock crosscutting relationships were selected for mineral liberation analysis (3 µm measurement spacing), whereas the samples from the surrounding lithologies were scanned using the line mapping function (50 µm measurement spacing).

The phase mapping and output function of the TIMA did not adequately differentiate between the fault rocks, alteration mineralogy and plagioclase resulting in poor textural detail within the phase maps. This is likely owing to the small BSE differences between the plagioclase, chlorite and pseudotachylite as well as the fine-grained nature of the chlorite and pseudotachylite. As such, colour-composite elemental maps were used as proxies for mapping the distribution and textures of the various minerals and clast types. ImageJ 1.52p was used to process the elemental maps into three-element colour-composite maps. The best results were obtained by creating false colour-composites of Fe-Mg-Cr, Mg-Ca-Al and (Mg+Fe-Cr)-Cr-Na elemental maps. For the Fe-Mg-Ca composite, the Fe, Mg and Cr elemental maps were assigned to the red, green and blue bands respectively (Figure 2.2). Likewise, for the Mg-Ca-Al composite, the Mg, Ca, and Al elemental maps were assigned to the red, green, and blue bands, respectively. For the (Mg+Fe-Cr)-Cr-Na composite, MatLab R2019B was used to produce a single greyscale image by summing each pixel with the Mg elemental map with the corresponding pixel from the Fe elemental map. Each pixel in the Cr elemental map was then deducted from the corresponding pixel in the Mg+Fe greyscale elemental map, producing a greyscale (Mg+Fe-Cr) greyscale elemental map. This map was then assigned to the red band, with the Cr and Na elemental maps assigned to the green and blue bands to produce the colour-composite map.

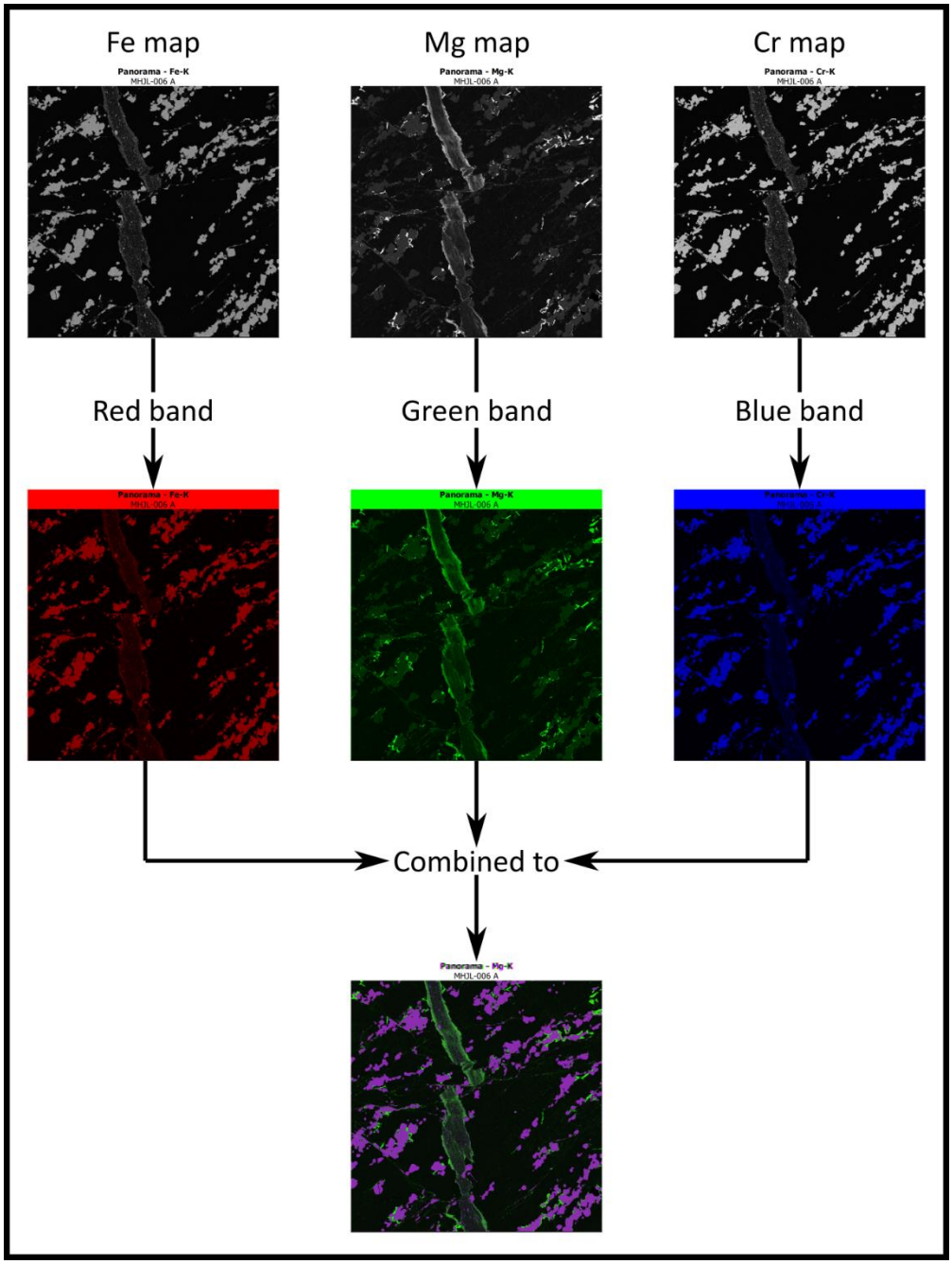


Figure 2.2: Flow diagram of the methodology used for the production of Fe-Mg-Cr and Mg-Ca-Al three-element colour-composite maps. The Fe, Mg and Cr elemental maps from MHL-006A scanning area A are used to exemplify the process.

The Fe-Mg-Cr colour-composite emphasizes the spatial relation of the chloritic alteration to both the magmatic and comminuted chromite aggregates as well as the distribution of the chloritic alteration within the cataclasites and breccias. The Mg-Ca-Al colour-composite emphasizes clast-shape and internal textures as well as fracture distribution within the anorthosite. The (Mg+Fe-Cr)-Cr-Na emphasizes the relationship between sodic and chloritic alteration.

All scanning areas are described in Appendix B and are accompanied by full thin section photomicrographs showing the position and context of the scanning areas.

Problems encountered

A problem with the use of the elemental maps as proxies for the mineral assemblages and element distribution is that each elemental map is scaled based on the maximum counts in the scan area. This means that the composite maps qualitatively represent the position of the elemental concentrations with respect to the other elemental maps used in the composite but cannot be used to determine the quantitative elemental proportions within the samples. Therefore, the maps show elemental associations but cannot be used to determine the mineralogy. In order to determine the mineralogy, the spectra used for the phase mapping function were compared to the TIMA spectra database. These minerals were then ascribed to the various colours and textures within the composite elemental maps using optical microscopy and textural correlation between the composite elemental and phase maps.

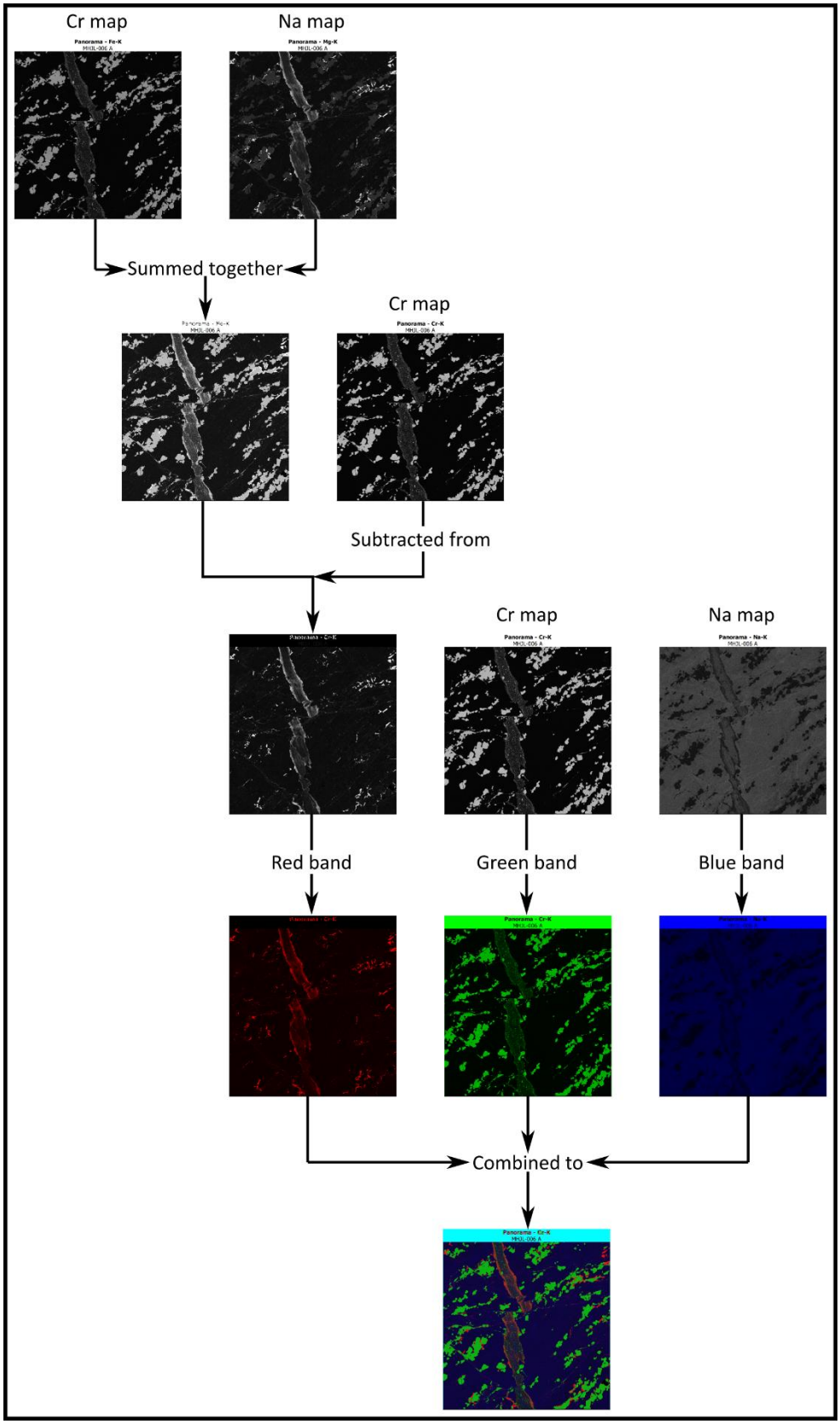


Figure 2.3: Flow diagram of the methodology used for the production of (Fe+Mg-Cr)-Cr-Na three-band colour-composite map. The Fe, Mg, Cr and Na elemental maps from MHL-006A scanning area A are used to exemplify the process.

3 Results

3.1 Regional structures

A preliminary regional lineament analysis was done on the greater study area comprising the northern portion of the Eastern Limb of the Bushveld Complex. The strongest lineament trends are the NNW and NE trends (Figure 3.1 and Figure 3.2). These follow the trends of the Wonderkop fault and the conjugates thereof as described by Basson (2019). The weaker E-W to ESE-WNW trend observed (Figure 3.1 and Figure 3.2) is possibly related to faulting associated with a NNE compression as proposed by Du Plessis and Walraven (1990). The layer-parallel fault under investigation in this study follows the same ESE-WNW trend indicated by the yellow line in Figure 3.1.

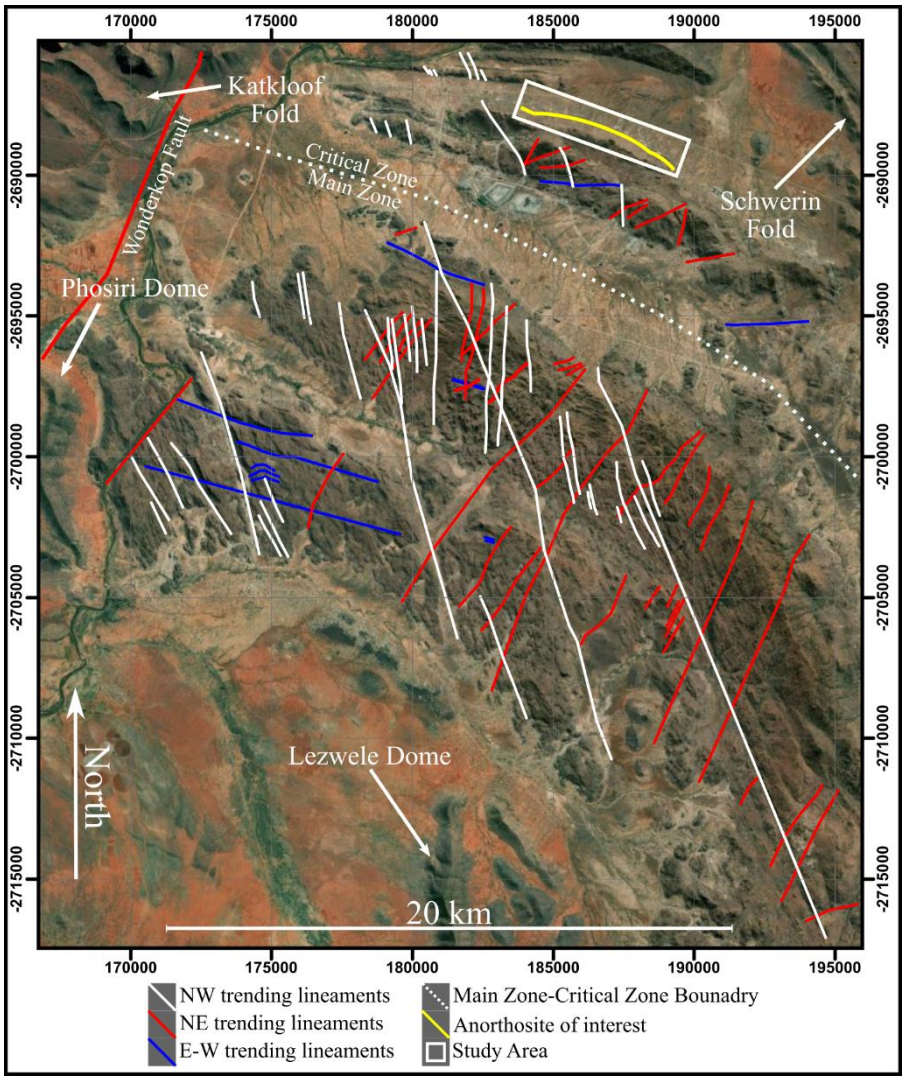


Figure 3.1: Regional lineaments ≥1 km and diapiric domes within the northern portion of the Eastern Limb, Bushveld Complex. UTM Grid 35J (Esri, 23 June 2013).

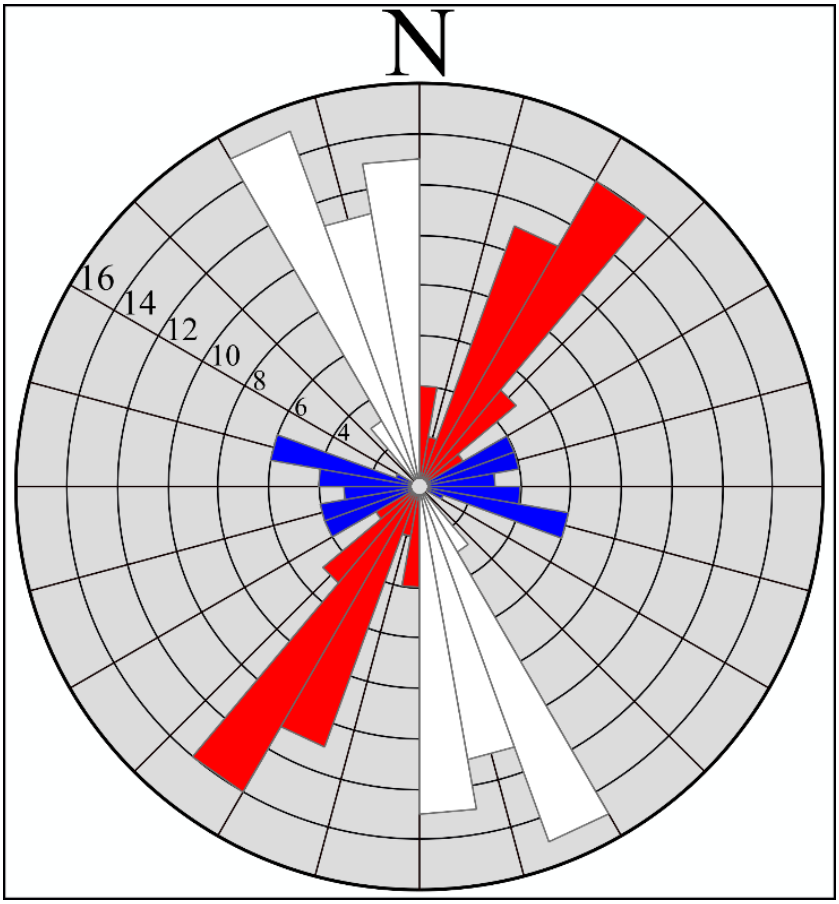


Figure 3.2: Rose diagram of the regional lineaments traced within the RLS lithologies of the northern portion of the Eastern Limb, Bushveld Complex (n=102). The white, red, and blue bars correspond to the NNW, NE and E-W trends traced in Figure 3.1, respectively.

3.2 The geology of Jagdlust Farm and adjacent farms

3.2.1 RLS stratigraphy

The RLS stratigraphy as exposed at Jagdlust Farm is underlain by Critical Zone harzburgites and pyroxenites, which outcrop to the north of the study area (Cameron, 1963). The base of the stratigraphic section of interest for this study is the pyroxenite underlying the LG-6 chromitite; both the pyroxenite and chromitite are exposed by artisanal diggings on the Jagdlust Farm, south of the R37 (Figure 3.3). The top of the section is the pyroxenite overlying the second anorthosite from the base of the ridge.

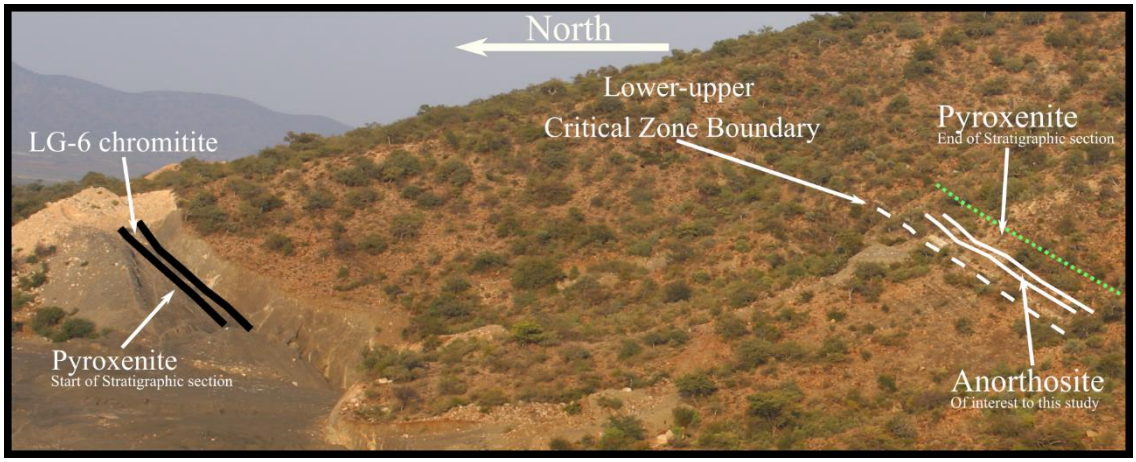


Figure 3.3: Profile of the northern slope of the ridge south of the R37 on the Jagdlust Farm with key stratigraphic layers: the pyroxenites marking the start and end of the stratigraphic section for the study, the anorthosite marking the lower-upper Critical Zone boundary and the anorthosite of interest to this study.

Lithologies

The LG-6 chromitite has a thickness of 40-50 cm. The layer has a granular to nodular texture with phaneritic chromite (0.3-0.5 mm) and interstitial pyroxene. The layer is under and overlain by pyroxenites with interstitial plagioclase. The overlying pyroxenite has phenocrystic clinopyroxenes disseminated throughout the rock. The LG-7 chromitite is separated from the LG-6 chromitite by this phenocrystic pyroxenite.

The LG-7 chromitite is matte black, massive, and aphanitic. The layer is ~30 cm thick with sharp and planar lower and upper contacts. Fractures in the layer are north dipping and curvi-planar to conchoidal with radial slickenlines. Overlying the LG-7 chromitite is a pyroxenite series defined by variations in chromite and phenocrystic clinopyroxene. This series continues through to the base of the anorthosite that defines the lower-upper Critical Zone boundary (Figure 3.4).

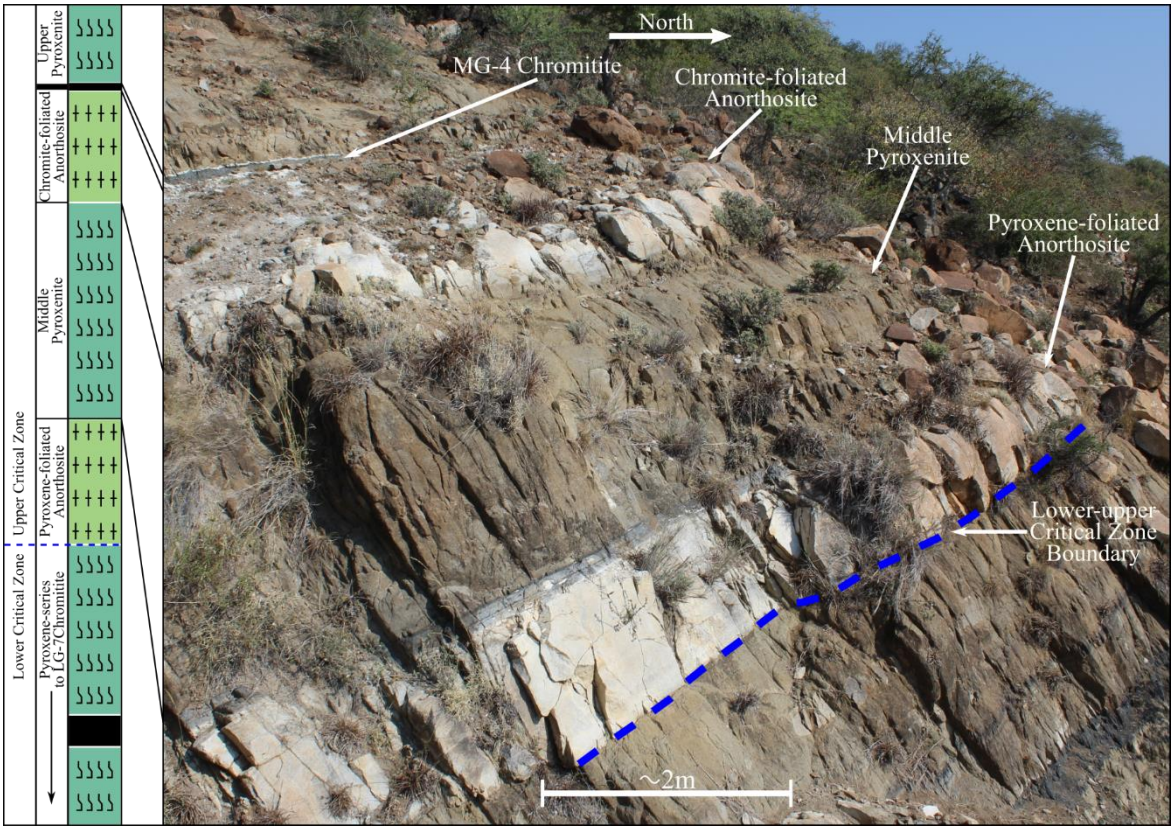


Figure 3.4: Simplified stratigraphy of the lower-upper Critical Zone boundary with an accompanying outcrop photograph of the boundary. The boundary is at the lower contact of the pyroxene-foliated anorthosite with the underlying pyroxenite and is marked by the dashed blue line.

The base of the anorthosite that defines the lower-upper Critical Zone boundary is sharp but irregular with the underlying pyroxenite (Figure 3.5B). The anorthosite varies between 0.8 m and 1.5 m in thickness along strike and has a layer-parallel magmatic foliation defined by pyroxene grain aggregates (~5-10%) and is referred to as the pyroxene-foliated anorthosite hereafter. An approximately 30 cm thick sublayer of chromititic-anorthosite marks the upper portion of the pyroxene-foliated anorthosite (Figure 3.5A). The sublayer is defined by magmatic chromite banding, which is parallel to the magmatic pyroxene-aggregate foliation. Chromite comprises up to 50% of the sub-layer mineralogy. Within the sublayer, there are autoliths of anorthosite as well as nodules of chromite and anorthosite, the latter of which may have a hook-shape (Figure 3.6A). Similar hook-shaped anorthosite nodules are found in the underlying pyroxenite series (Figure 3.6B).

The upper contact of the pyroxene-foliated anorthosite is planar but gradational with the overlying pyroxenite; chromite content in the sublayer increases upwards and plagioclase is replaced by pyroxene as the interstitial mineral. The sub-layer has a gradational contact with the overlying pyroxenite. The gradation is ~2 cm with chromite decreasing to <1%, pyroxene increasing to ~90% and interstitial plagioclase is re-introduced at ~10%

(Figure 3.5A). The thickness of the pyroxenite overlying the pyroxene-foliated anorthosite (hereafter referred to as the middle pyroxenite) varies along strike from 1-2.5 m, having a mean thickness of 2 m. Hook-shaped nodules of anorthosite, similar to those in the underlying pyroxene-foliated anorthosite, are present within this layer (Figure 3.6B).

The middle pyroxenite grades into the overlying anorthosite. The base of the anorthosite is noritic in composition, with pyroxene aggregates defining a weak magmatic foliation. Pyroxene content decreases upward, over 30 cm, giving way to layer-parallel 0.1×2 mm, chromite-grain aggregates defining a layer-parallel, magmatic foliation. This anorthosite is referred to as the chromite-foliated anorthosite hereafter. The anorthosite layer thickness varies laterally between 1 m and 2 m. Outcrop texture also varies laterally between hard, consolidated white to bluish-white anorthosite and highly friable, granular to powdery greyish-white to white anorthosite. Typically, friable outcrop grades upwards from a moderately cohesive granular texture at the base of the anorthosite to friable, powdered anorthosite near the contact with the overlying chromitite. The upper contact of the chromite-foliated anorthosite with the overlying chromitite is obscured by the fault surface.

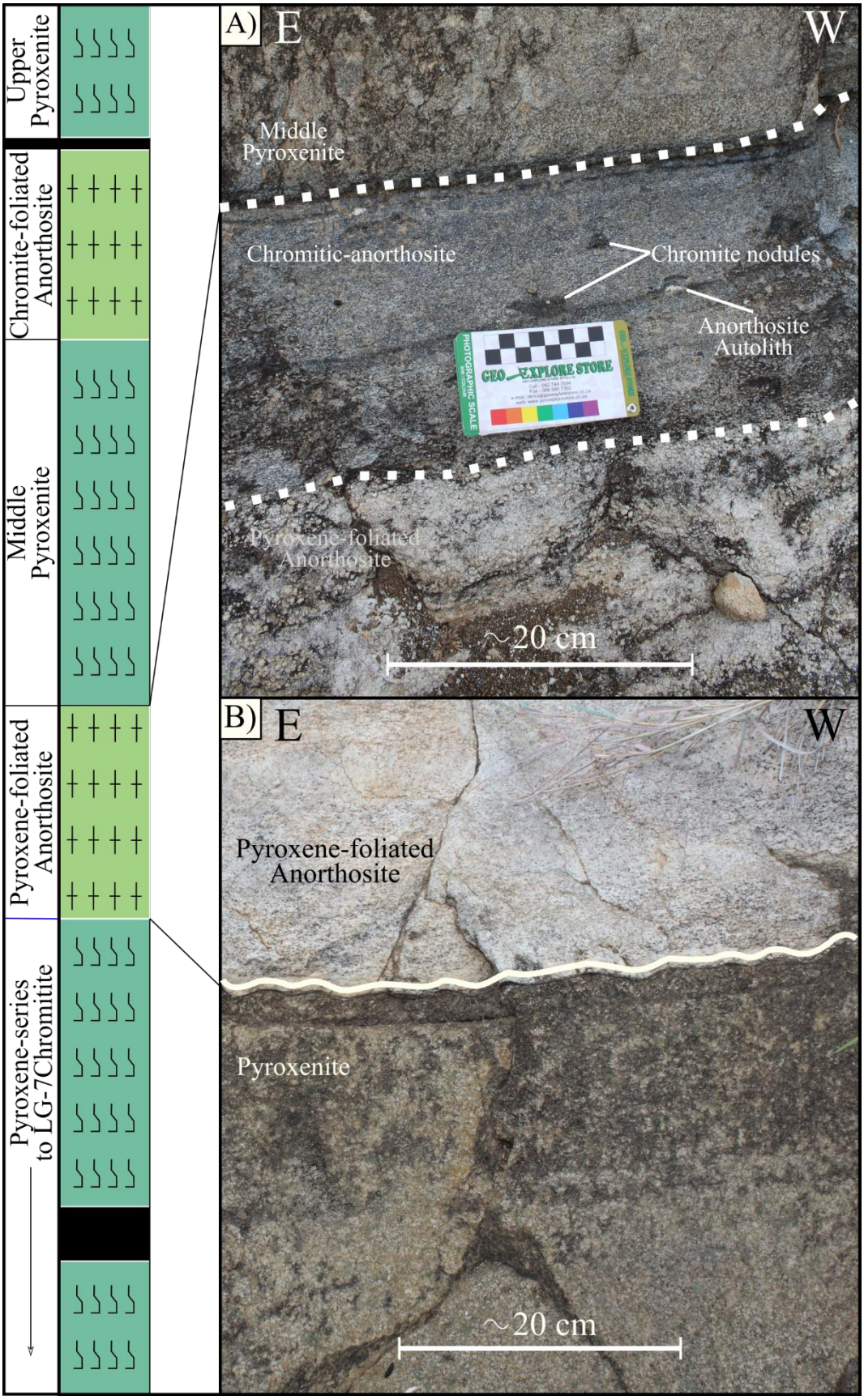


Figure 3.5: Simplified stratigraphy of the lower-upper Critical Zone boundary with accompanying outcrop photographs of the upper (A) and lower (B) contacts of the pyroxene-foliated anorthosite.

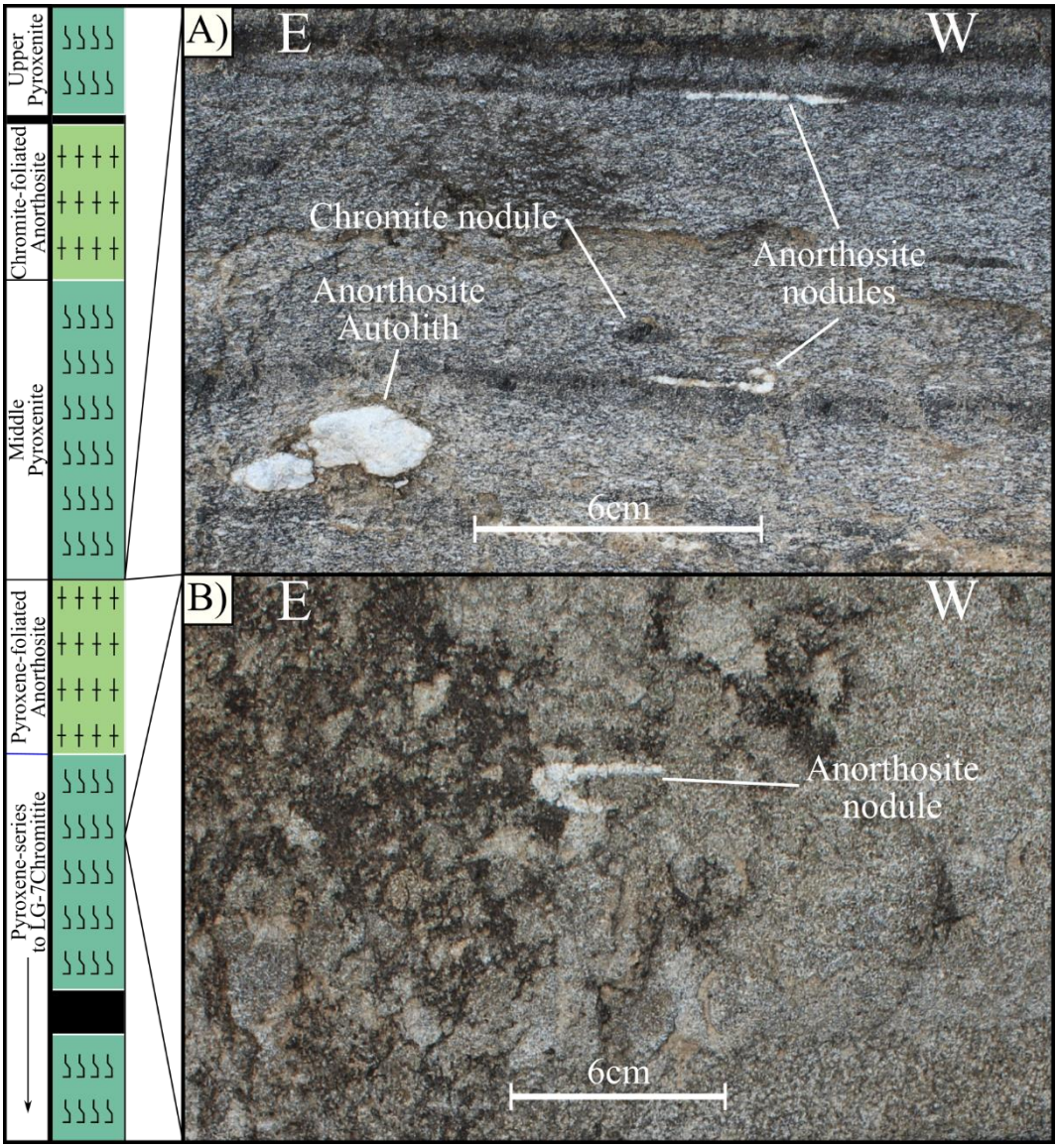


Figure 3.6: Simplified stratigraphy of the lower-upper Critical Zone boundary accompanied by (A) chromitite and anorthosite nodules in the pyroxene-foliated anorthosite upper contact and (B) hook-shaped nodules of anorthosite within a pyroxenite of the pyroxenite series between the LG-7 chromitite and lower-upper Critical Zone boundary.

The overlying chromitite layer is probably the MG-4 chromitite (Eales and Cawthorn, 1996) and is ~30 cm thick. The chromitite is friable, particularly along its base. A 2-4 cm thick chromite-foliated anorthosite occurs 1-3 cm below the upper contact of the chromitite. This layer is irregular to undulatory, highly fractured and friable (Figure 3.7). The upper contact of the chromitite with the overlying pyroxenite is sharp but irregular to undulatory.

The pyroxenite overlying the MG-4 chromitite comprises of >1 mm, equant, pyroxene grains with interstitial plagioclase. The layer is devoid of clinopyroxene phenocrysts.

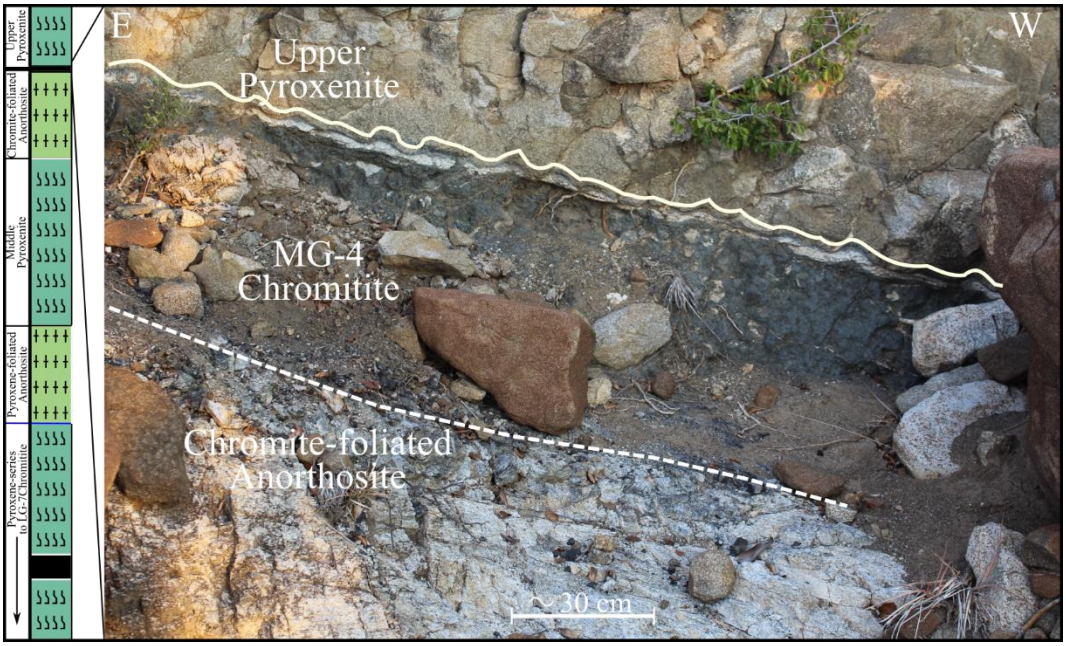


Figure 3.7: Simplified stratigraphy of the lower-upper Critical Zone boundary accompanied by an outcrop photograph of the MG-4 chromitite overlying the chromite-foliated anorthosite (the dashed white line traces the contact). The anorthosite stringer layer in the chromitite is seen with the stringer's irregular form. The chromitite-pyroxenite contact parallels the morphology of the anorthosite stringer layer (solid white line).

Orientations of Magmatic layers and chromite-foliation.

Magmatic layering in the RLS within the study area has an average dip of 21° and dip-direction of 208° (Figure 3.8). The chromite-grain aggregates forming the magmatic foliation within the anorthosite are elongate parallel to subparallel to the layering, having an average dip of 26° and dip-direction of 205° (Figure 3.8).

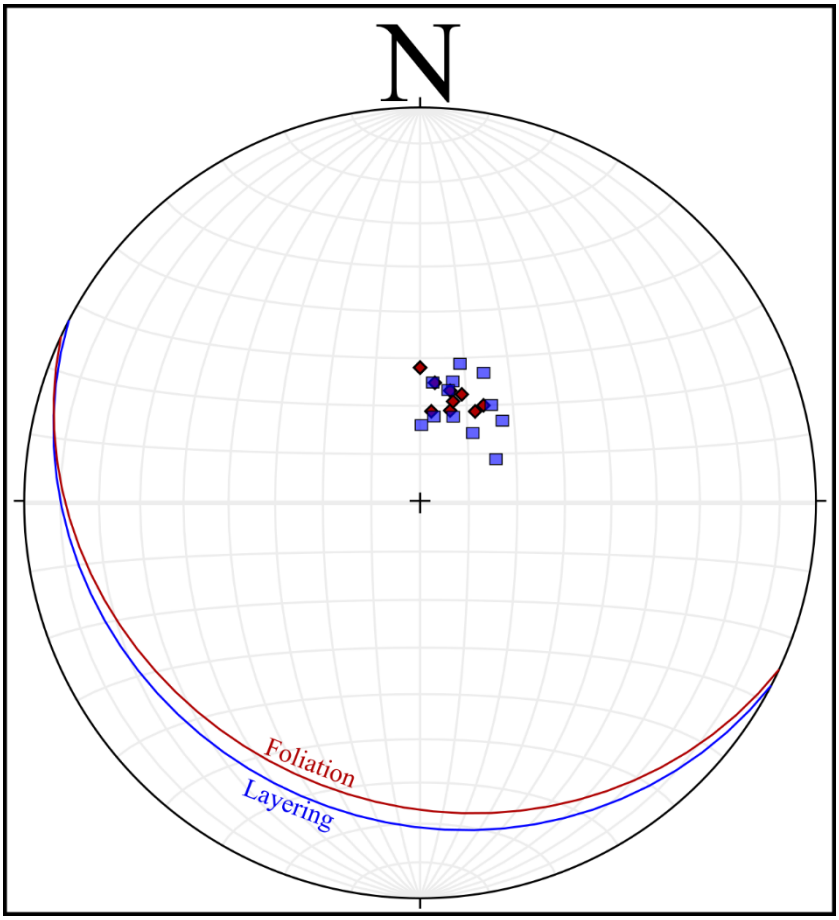


Figure 3.8: Equal area stereoplot of the poles to the magmatic layering (n=12, blue squares) of the RLS and chromite-foliation (n=6, red diamonds) within the study area. The average planes, as dip-angle → dip-direction, for layering (blue) and the foliation (red) are dipping at 21°→208° and 26°→205°, respectively.

3.2.2 Dykes and sills

Several dykes and a single sill intrude the RLS layering within the study area. The intrusive rock is aphanitic and brown and is highly weathered. A high joint density has resulted in segmentation of the intrusions into centimetre-sized orthogonal blocks. Although no general trend is seen in the dyke orientations (Figure 3.9) the NE and NW-trends of the Soutpansberg and Waterberg dyke swarms are possibly represented by the dykes dipping at 74°→306° and 58°→059°, respectively (Uken and Watkeys, 1997). Alternatively, the NE-trending dyke dipping at 74°→306° is associated with the Olifants River dyke swarm that is interpreted as contemporaneous with the Karoo dyke swarm (Uken and Watkeys, 1997; Basson, 2019).

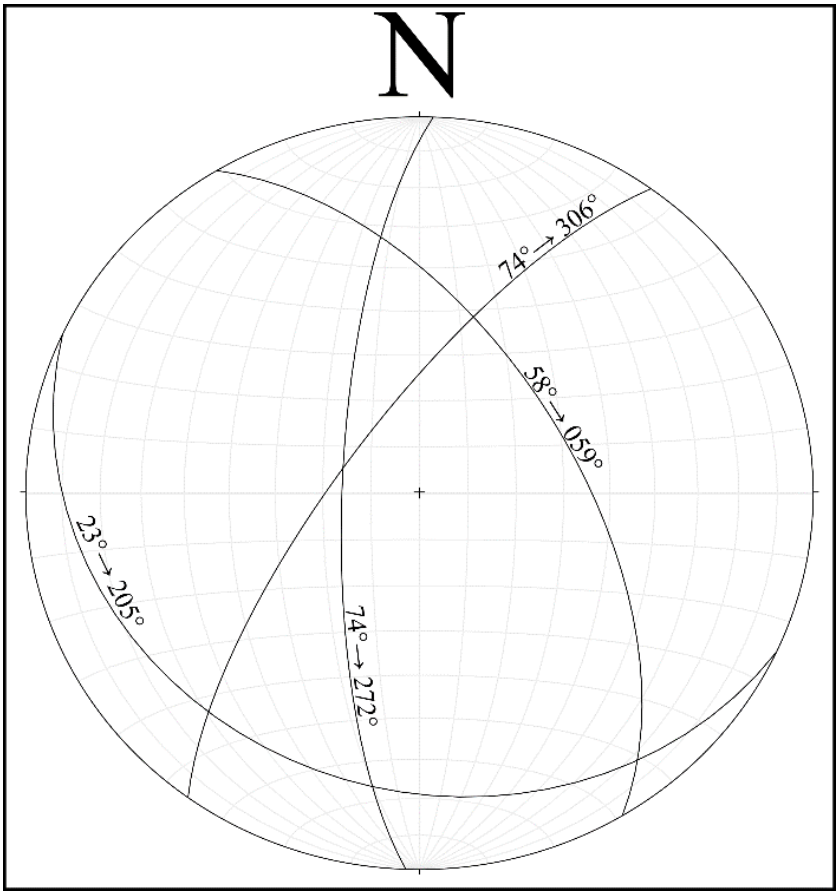


Figure 3.9: Equal area stereoplot of the planes for the post-RLS dykes and sill within the study area. Orientations are labelled dip → dip-direction of the plane. The 74°→272° and 58°→059° dykes lie at a 58° angle, whereas the 23°→205° sill and 74°→272° dyke lie at a 67° angle.

3.3 The chromite-foliated anorthosite fault

Several fault rock types are present within the chromite-foliated anorthosite exposed on Jagdlust Farm and adjacent properties. These fault rocks include quasi-ductile cataclasite, pseudotachylite, cataclasite and breccia. These fault rocks are found in both float and outcrop for at least 6 km laterally along the chromite-foliated anorthosite strike (Figure 3.10). The full lateral extent of these fault rocks could not be determined owing to access restrictions and safety concerns. Likewise, several attempts were made to obtain access to down-dip borehole logs, however, these were denied.

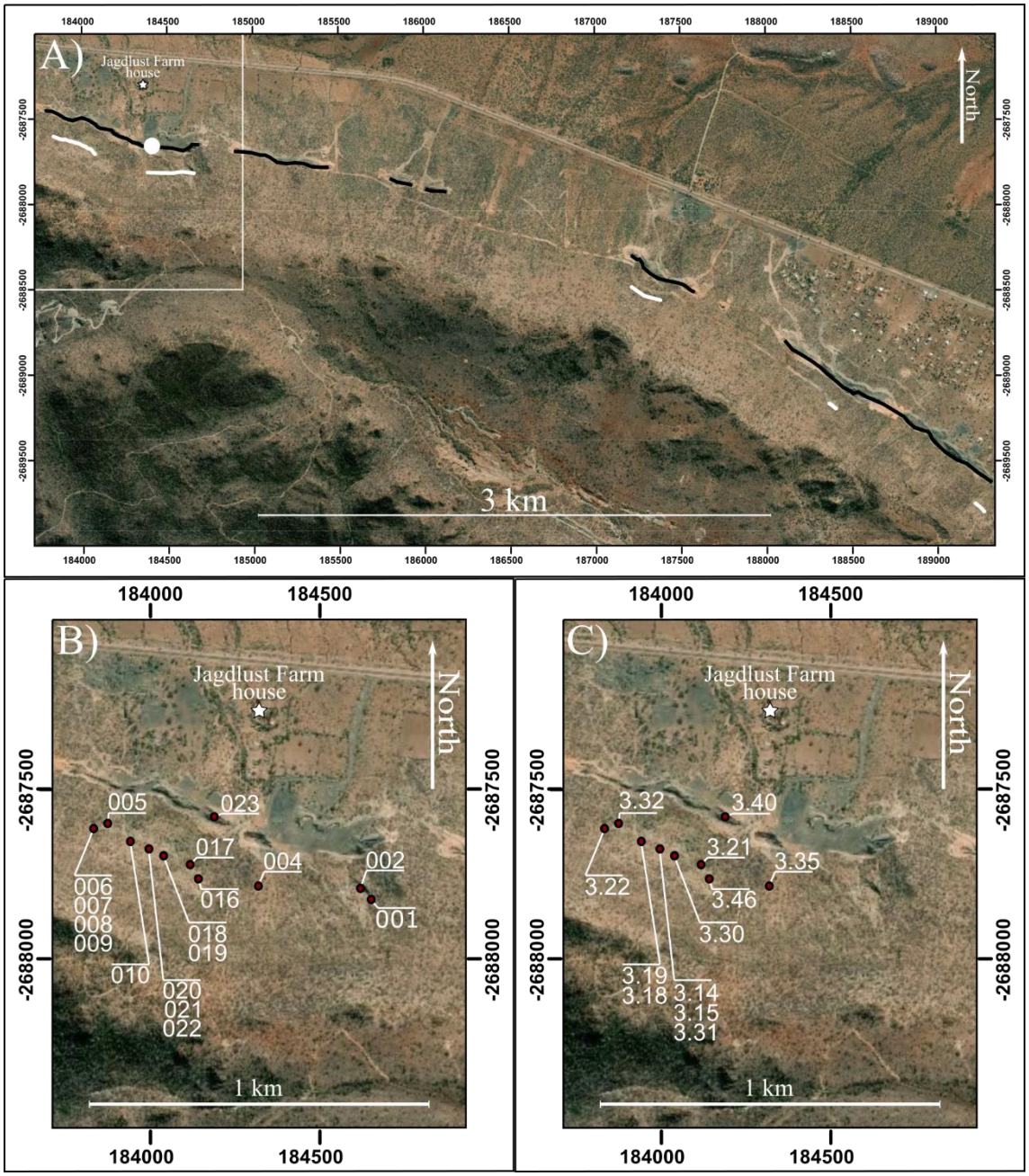


Figure 3.10: A) is a satellite image of the study area with the chromite-foliated anorthosite (white lines) and LG-6 chromitite (black lines) outcrops traced. The white box delineates the enlarged area of B) and C). B) shows the localities for samples collected on Jagdlust farm. B) shows the localities for several outcrop photographs, e.g. Figure 3.14. UTM Grid 35J (Esri, 23 June 2013).

Figure 3.11 shows the general morphology of the fault within the chromite-foliated anorthosite as interpreted from various outcrops, particularly on Jagdlust Farm, within the study area. The various fault rocks and associated features are described below.

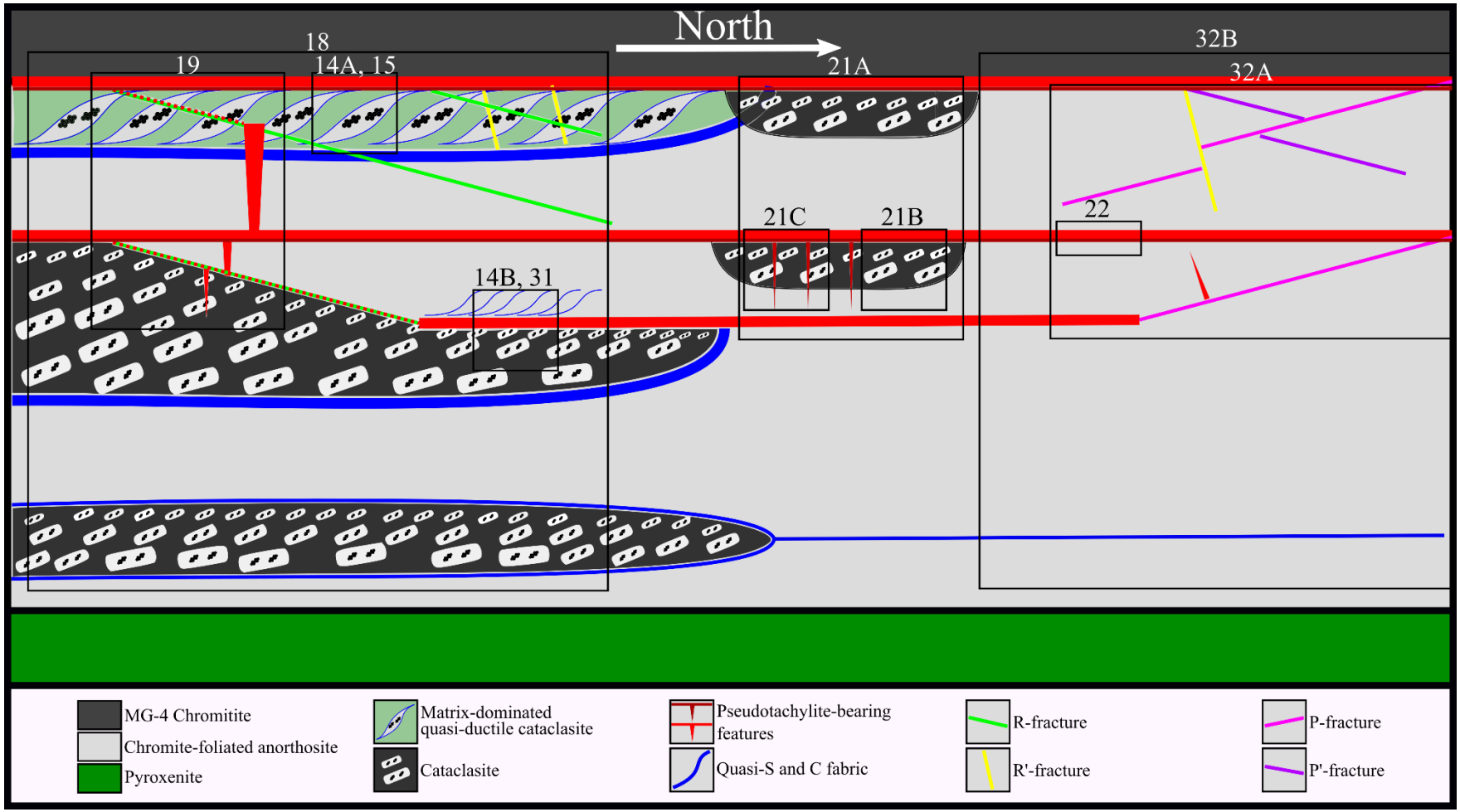


Figure 3.11: Sketch diagram of the fault within the chromite-foliated anorthosite bounded by the MG-4 chromitite and middle pyroxenite showing the main spatial and geometric characteristics of the fault. The sketch is drawn parallel to the slickenlines on the layer-parallel fracture surfaces. The P, P', R and R' fractures indicate a top-to-north displacement. The black boxes with labels represent where the respective figures for the features can be found, e.g. "11B, 13, 30" indicates that Figures 3.11B, 3.13 and 3.30 show the quasi-ductile cataclasite overlying a pseudotachylite and cataclasite. The diagram is not drawn to scale.

3.3.1 Chromite-foliated anorthosite wallrock

The chromite-foliated anorthosite is the wallrock to the fault rocks mentioned above but is also fractured, forming a part of the fault zone consisting of the fault rocks described below.

Fractures forming oblique to the chromite-foliation are abundant within the chromite-foliated anorthosite. These, however, are typically associated with the fault rocks described below.

Foliation-parallel to subparallel fractures are evident within the layer (Figure 3.12). These fractures are <1 mm thick; either being open or having aphanitic fracture fill. The edges of the fractures are curvi-planar, deflecting up towards the MG-4 chromitite contact.

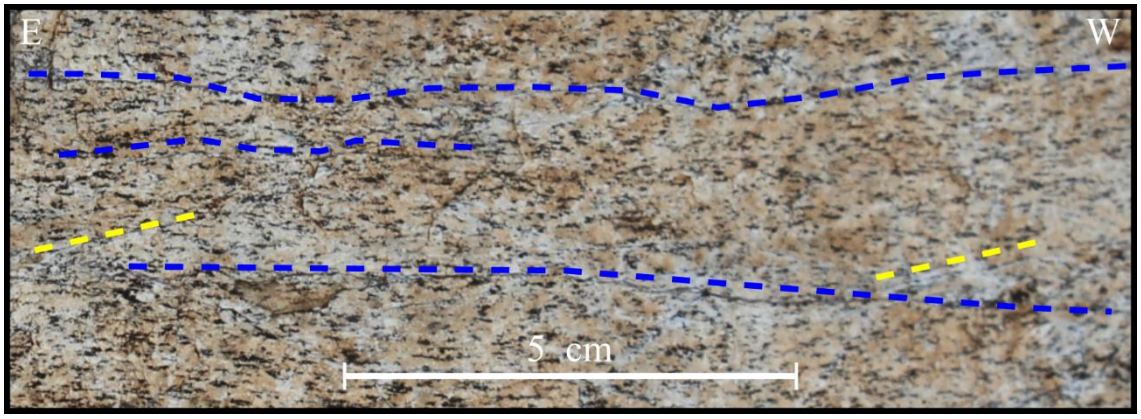


Figure 3.12: Outcrop photograph of foliation-parallel fractures (dashed blue lines) and foliation-oblique fractures (dashed yellow lines) associated with the foliation parallel fractures.

Throughout all the thin section samples, foliation-parallel fractures are observed (Figure 3.13). These fractures have anastomosing to planar forms and truncate the magmatic plagioclase grains to give the appearance of layer-parallel alignment of the elongated crystal axis. The thickest fractures are <0.4 mm and are filled with comminuted plagioclase and chromite grains, <0.1 mm, within a brown-green cryptocrystalline matrix. Foliation-oblique fractures associated with these fractures have a similar form and fracture fill but may be thicker, <0.8 mm.

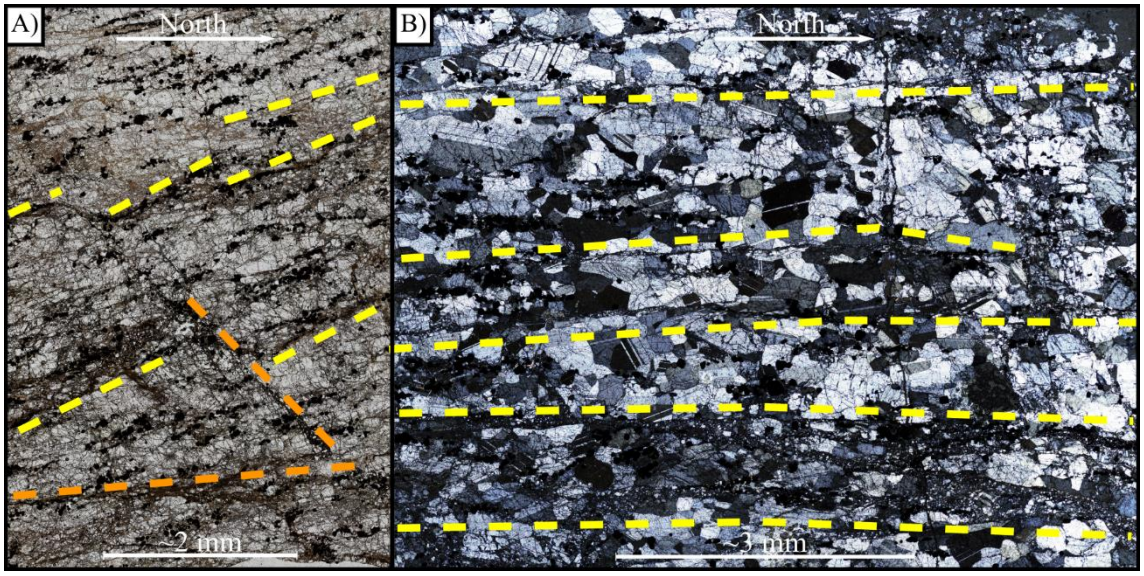


Figure 3.13: A) PPL photomicrograph of a portion of MHJL-001 thin section showing foliation-parallel (dashed yellow lines) and foliation-oblique (dashed orange lines) fractures with anastomosing form within the chromite-foliated anorthosite. B) XPL photomicrograph of a portion of MHJL-002 thin section showing foliation-parallel (dashed yellow lines) fractures with planar form within the chromite-foliated anorthosite.

3.3.2 Quasi-ductile cataclasite

Two discontinuous quasi-ductile cataclasite zones are locally evident within the chromite-foliated anorthosite: a lower, ~10 cm thick, cataclasite displays a sigmoidal fabric between fault-parallel shear fractures, and an upper, ~5 cm thick, sigmoidal-clast, quasi-ductile cataclasite with rhomboidal to sigmoidal clasts. The sigmoidal-fabric, quasi-ductile cataclasite comprises comminuted-chromite aggregates defining a sigmoidal fabric between fault-parallel shear fractures, found toward the middle of the layer (Figure 3.14B, MHJL-021). This lower quasi-ductile cataclasite grades into the host anorthosite over ~20 cm.

The sigmoidal-clast, quasi-ductile cataclasite displays ≤1×2 cm, rhomboidal to sigmoidal, polycrystalline clasts in ≥50% aphanitic matrix. This upper quasi-ductile cataclasite is found within 10 cm of the upper MG-4 chromitite contact (Figure 3.14A, MHJL-014, 020 and 021). This cataclasite has sharp boundaries with the host anorthosite and, locally, has alternating clast-rich and clast-poor bands, which are ≤2 cm and ≤1 cm wide, respectively (Figure 3.15).

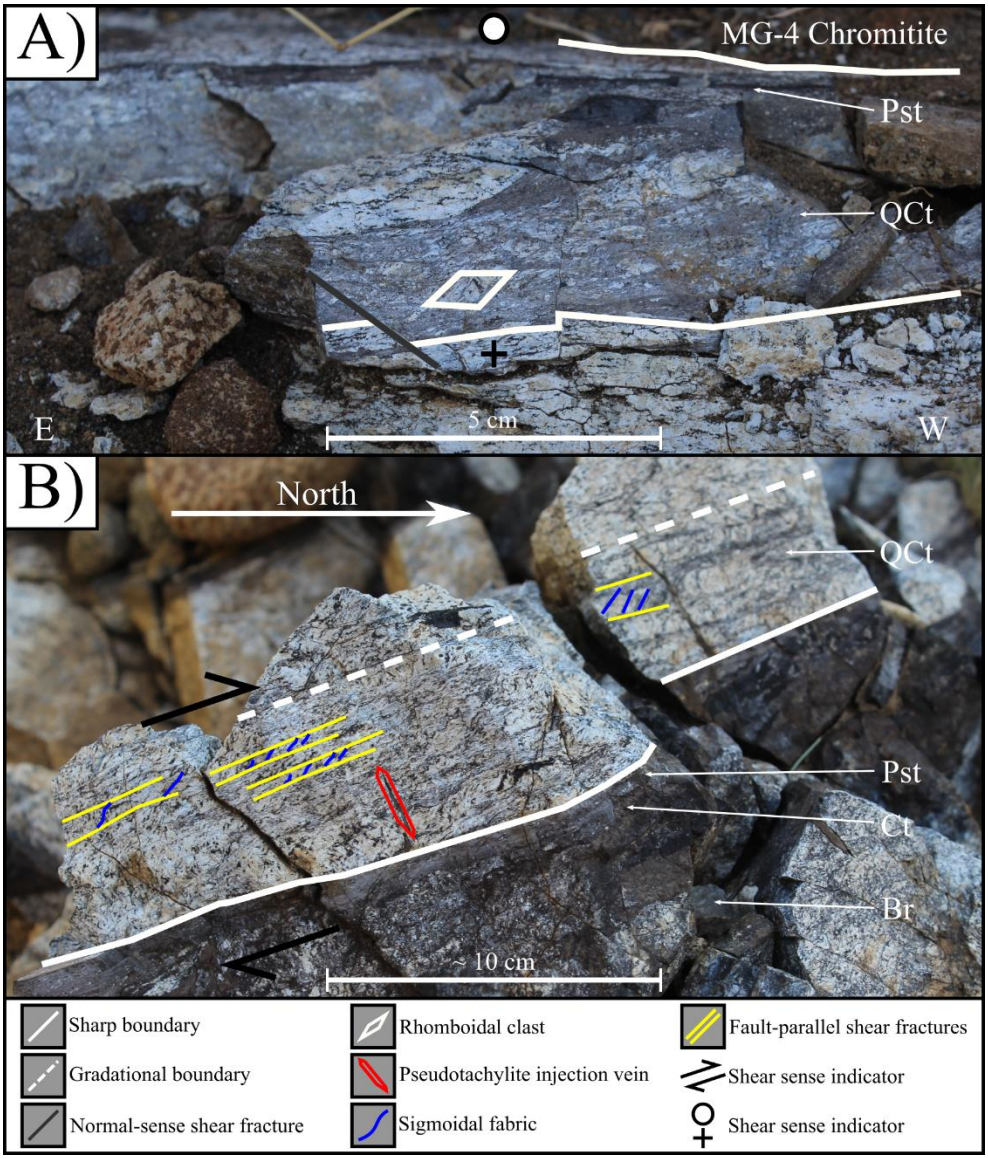


Figure 3.14: A) Outcrop photograph of a rhomboidal to sigmoidal-clast, quasi-ductile cataclasite with sharp boundaries with overlying cataclasite and underlying anorthosite. B) Outcrop photograph of a quasi-ductile cataclasite with sigmoidal fabric and fault-parallel shears. The quasi-ductile cataclasite has a gradational upper boundary with the anorthosite wallrock and a sharp contact with the underlying pseudotachylite GPPD. The sigmoidal fabric and fault-parallel shears are crosscut by a pseudotachylite injection vein. The pseudotachylite has a gradational boundary with the underlying cataclasite, which grades into a breccia. QCt is quasi-ductile cataclasite, Pst is pseudotachylite, Ct is cataclasite, Br is breccia. See Figure 3.10 for photograph location.

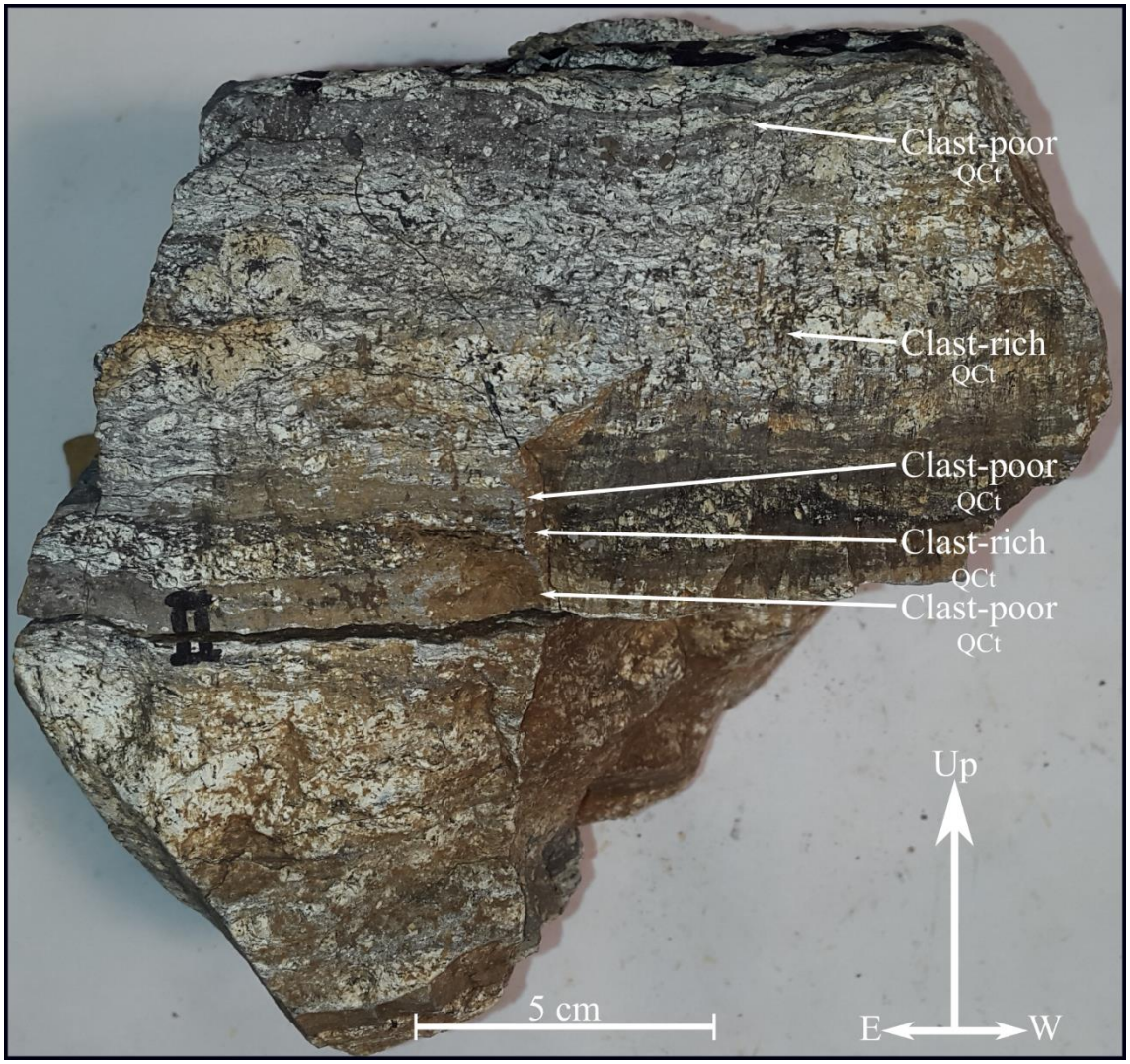


Figure 3.15: Photograph of hand sample MHJL-021, which shows alternating clast-rich and clast-poor bands within the sigmoidal-clast, quasi-ductile cataclasite (QCt). Owing to the shape of the sample a N-S profile photograph is not informative. See Figure 3.10 for photograph location.

Thin sections the quasi-ductile cataclasites show clasts consist of mono- to polycrystalline plagioclase and polymineralic foliated-anorthosite clasts (≤1×2 cm) within a matrix of cryptocrystalline alteration product containing ≤0.1 mm chromite and plagioclase clasts (Figure 3.16). Most clasts are comminuted in a brittle fashion, however, evidence for subgrain rotation grain-size reduction is found in a few of the larger polycrystalline clasts (Figure 3.17). Comminution of polycrystalline clasts produced subangular, sigmoidal and well-rounded clasts with varying degrees of clast rotation (Figure 3.16).

Chromite within the matrix forms cryptocrystalline grain aggregates. These aggregates have a sigmoidal shape, dipping ~40° south but become asymptotic to fault-parallel shears (Figure 3.16). The orientation and sigmoidal shape of these aggregates resemble S fabrics. The sigmoidal fabric and fault-parallel shears crosscut R'-shears

within the wallrock. Comminuted-chromite aggregates define R shears within the matrix of the sigmoidal-fabric, quasi-ductile cataclasite, however, this fabric is poorly developed compared to the sigmoidal fabric (Figure 3.16).

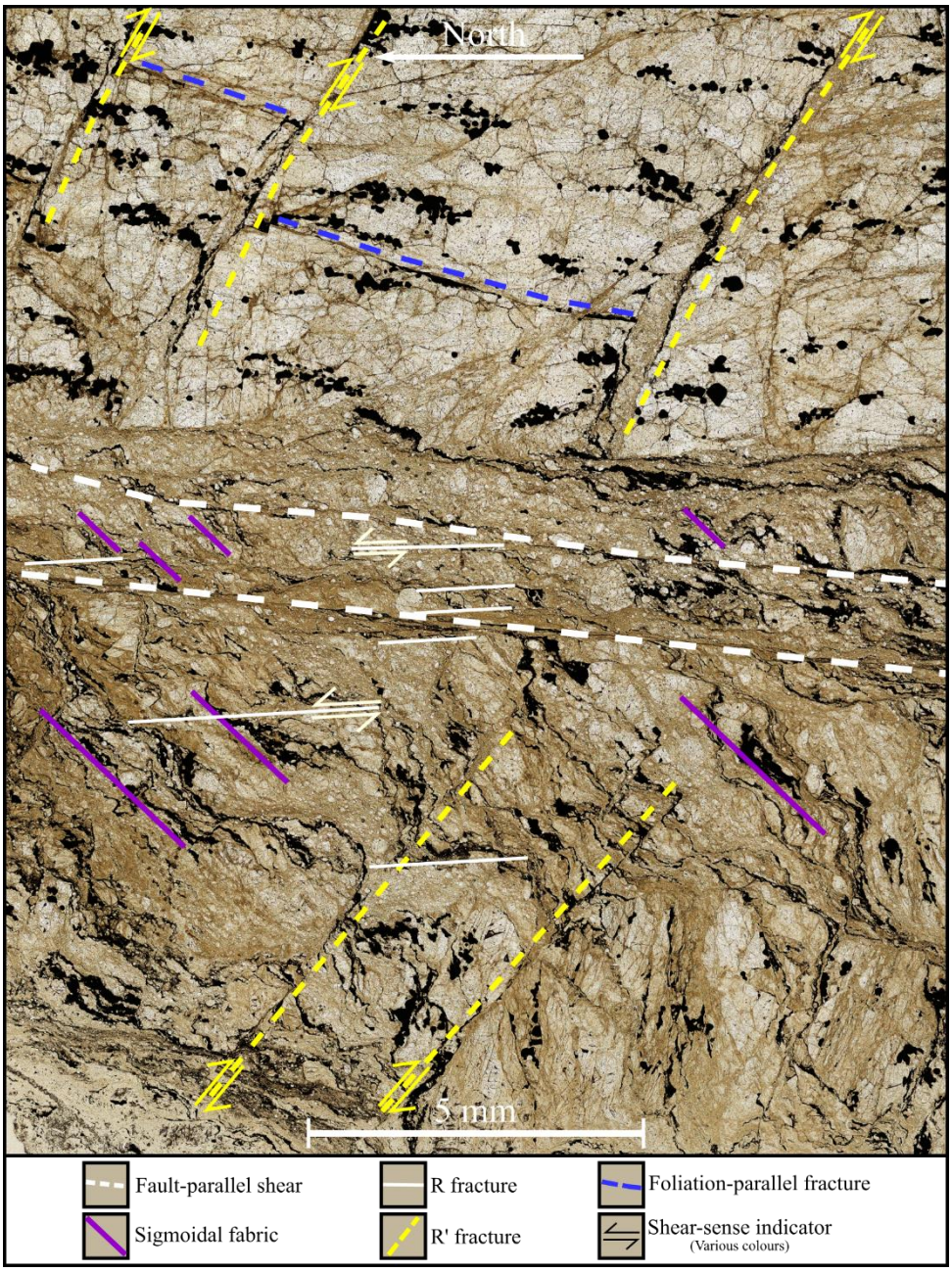


Figure 3.16: PPL photomicrograph of hangingwall anorthosite and lower cataclasite with sigmoidal fabric and fault-parallel shears in MHJL-022. The thin section shows R' fractures which are crosscut by sigmoidal fabrics and fault-parallel shears. Furthermore, the clast-shape variation is seen with well-rounded clasts between the two traced fault-parallel shears and subangular to subrounded clasts below the traced fault-parallel shears. See Fractures under Crosscutting relationships for foliation-parallel fractures. See Figure 2.1 for sample location.

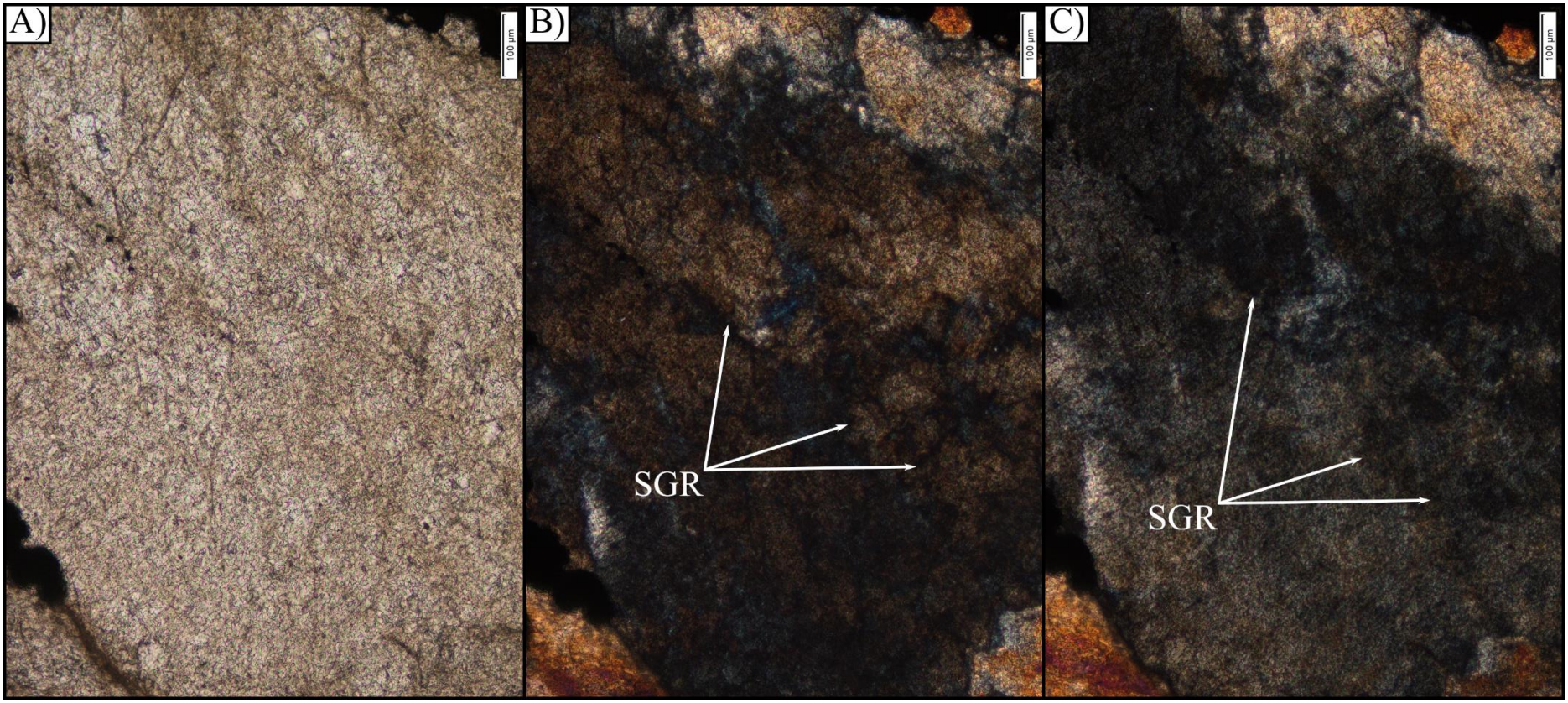


Figure 3.17: Photomicrograph showing the onset of subgrain rotation (SGR) within a clast in MHJL-022. A) is a PPL photomicrograph. B) and C) are XPL photomicrographs. C) was taken after the stage was rotated 10° anticlockwise with respect to B).

3.3.3 Pseudotachylite

Pseudotachylite in the study area occurs as aphanitic, generally massive but locally clast-laden or colour-banded, layer-parallel, and layer-discordant dykes within the chromite-foliated anorthosite. Pseudotachylite-bearing layer-parallel dykes are subparallel to the faulted contact of the chromite-foliated anorthosite with the MG-4 chromitite; these fractures are thus interpreted as GPPDs (Figure 3.18). Discordant pseudotachylite-dykes extend ≤5 cm and ≤20 cm into both the footwall and hangingwall, respectively, from the GPPDs. The discordant dykes are interpreted as injection veins (Figure 3.19 and Figure 3.21).

Within the best-preserved outcrops, on Jagdlust Farm, up to four GPPDs may be present (Figure 3.18). Locally, these GPPDs are planar to undulatory and have bifurcations, which produce new GPPDs as the bifurcations become parallel to the layering (Figure 3.18 and Figure 3.19). Over the extent of the study area, however, GPPDs are subparallel to parallel with the magmatic layering and foliation, dipping at 25° → 195° (Figure 3.20). The GPPDs typically have sharp and planar upper contacts (Figure 3.21A). The form of the lower contact of the GPPDs is dependent on the footwall rock. Where the footwall is highly fractured anorthosite, the contact is also sharp and planar (Figure 3.22). Where the footwall is cataclasite or breccia, the contacts are typically sharp and irregular. However, locally these contacts may be diffuse and irregular, showing the mixing of pseudotachylite with the underlying fault rocks (Figure 3.19 and Figure 3.21A and B).

The GPPDs are up to 5 cm thick and may display more than one pseudotachylite generation (Figure 3.21A and Figure 3.22). The various pseudotachylite generations range in colour from black (matte and vitreous) to grey (light and dark) to brown (Figure 3.21A and Figure 3.22).

Macroscopic clast content also varies between the pseudotachylite generations from absent to ~10% volume (Figure 3.22). Clasts predominantly consist of plagioclase (Figure 3.22) with few pseudotachylite generations displaying macroscopic chromitite or pseudotachylite clasts. Clasts are up to 5 mm in diameter.

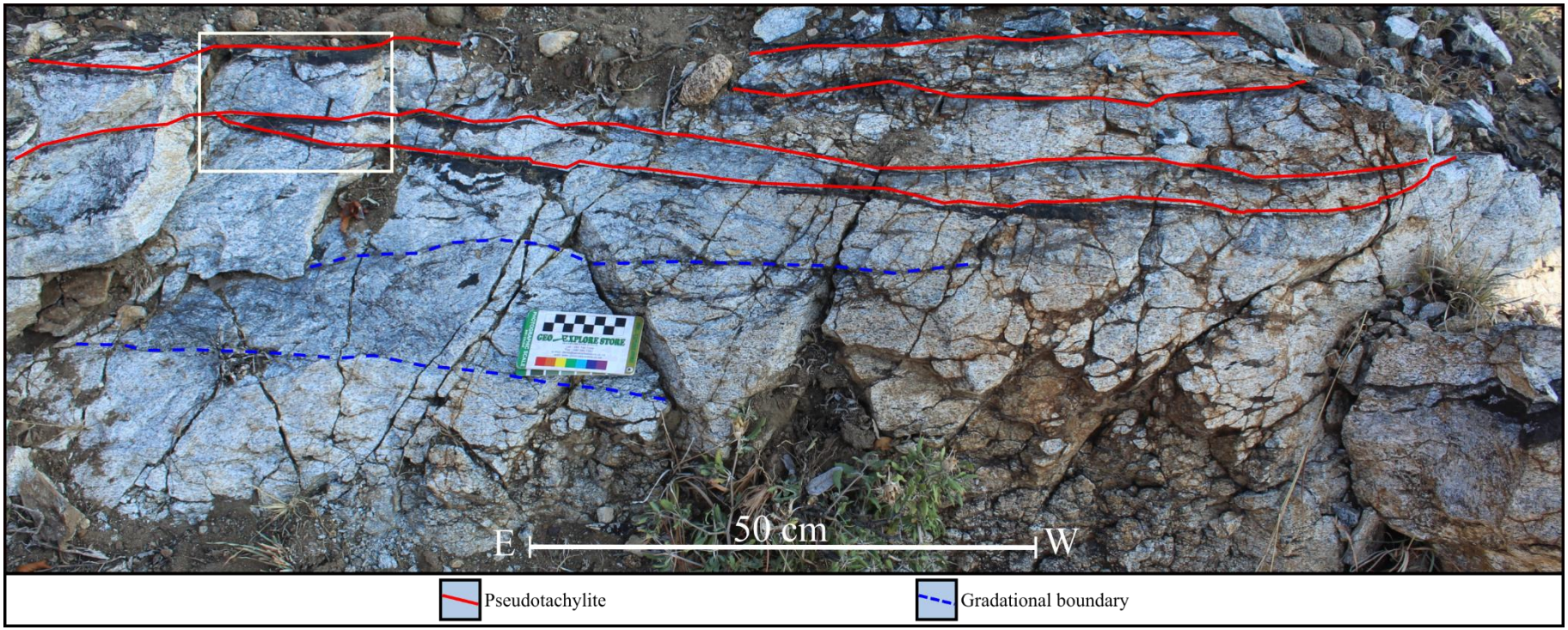


Figure 3.18: An E-W profile outcrop, perpendicular to the fault slip direction, of the chromite-foliated anorthosite showing four pseudotachylite GPPDs. Each GPPD is underlain by cataclasite. Two of the GPPDs can be seen to be the result of bifurcations (white box, see Figure 3.19). A 30 cm thick breccia is seen and has gradational boundaries with the chromite foliated anorthosite. See Figure 3.10 for photograph location.

The majority of injection veins extend from the various GPPDs into the footwall (Figure 3.21C). The longest veins are >20 cm, most are ≤10 cm. Edges of the veins are sharp albeit irregular, irrespective of the rock the vein injects into (Figure 3.19 and Figure 3.21B). The pseudotachylite in these veins resembles that found in the GPPD from which it extends, in both colour and clast content. During sample processing, it was noted that, locally, injection veins have a conjugate form with N-S and NW-SE to E-W trends (Figure 3.23). These trends, however, were not observed in outcrop, which is likely owing to poor 3D exposure of the injection veins in unfavourably oriented, E-W trending outcrop (Figure 3.24).

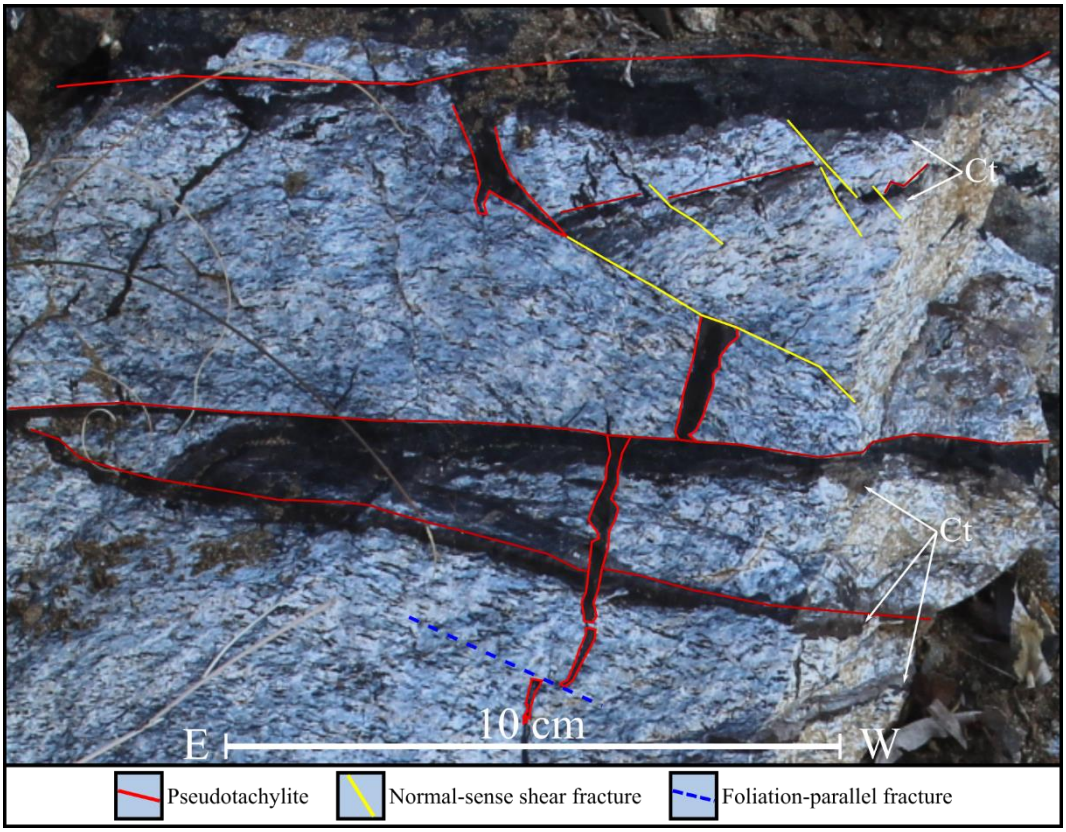


Figure 3.19: Outcrop photograph of the uppermost pseudotachylite GPPD and an underlying GPPD showing a bifurcation. The pseudotachylite injection vein crosscuts the pseudotachylite within the underlying GPPD and bifurcation but is displaced along the top surface of the middle GPPD. Furthermore, the pseudotachylite from the upper GPPD injects into a W-dipping, normal-sense shear fracture, which appears to displace the injection vein associated with the upper GPPD. The injection vein is also crosscut by a foliation-parallel fracture. Ct is cataclasite. The photograph is an enlargement of the white box, Figure 3.18. See Figure 3.10 for photograph location.

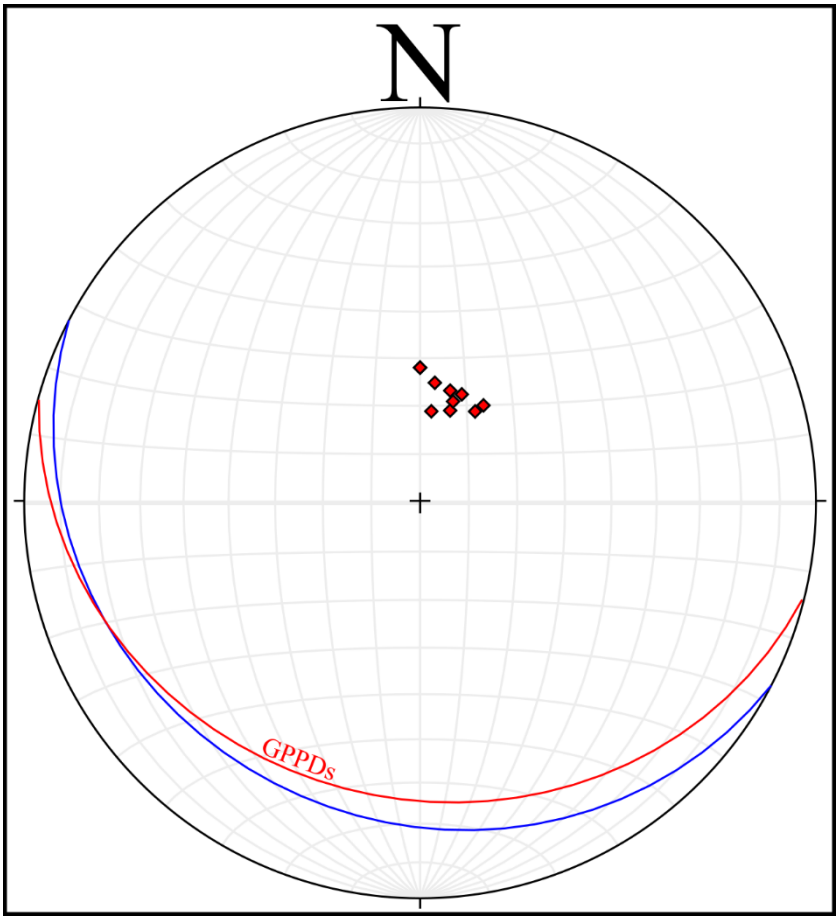


Figure 3.20: Equal area stereoplot of poles to GPPDs (n=10). The solid red line is the average plane to GPPDs poles (dipping at 25° → 195°). The blue line is the average plane to magmatic layering (see Figure 3.8).

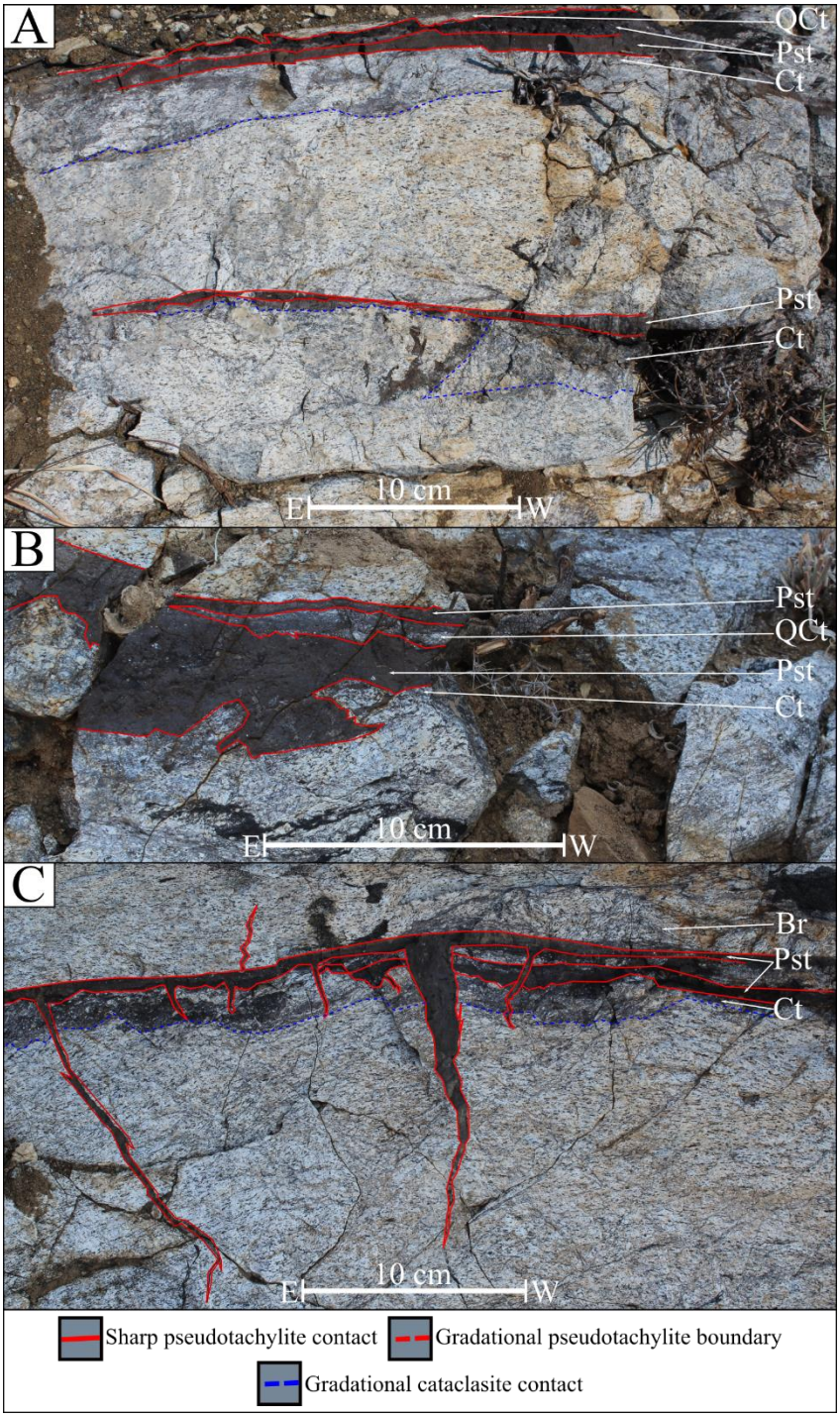


Figure 3.21: Outcrop-scale pseudotachylite features and relationships with the host and fault rocks. A) shows two GPPDs, the upper having two pseudotachylite generations, both of which overlie breccia. The photo shows the weakly undulatory nature of the GPPDs. Injection veins from the upper GPPD inject downward from the GPPDs into the breccia, whereas the lower GPPD has upward and downward injection veins. B) shows the mixing of pseudotachylite with the underlying breccia. C) shows breccia overlying a GPPD. The GPPD has a gradational boundary with the underlying cataclasite. Several downward injection veins and a single upward injection vein extend from the GPPD. QCt is quasi-ductile cataclasite, Pst is pseudotachylite, Ct is cataclasite. See Figure 3.10 for photograph location.

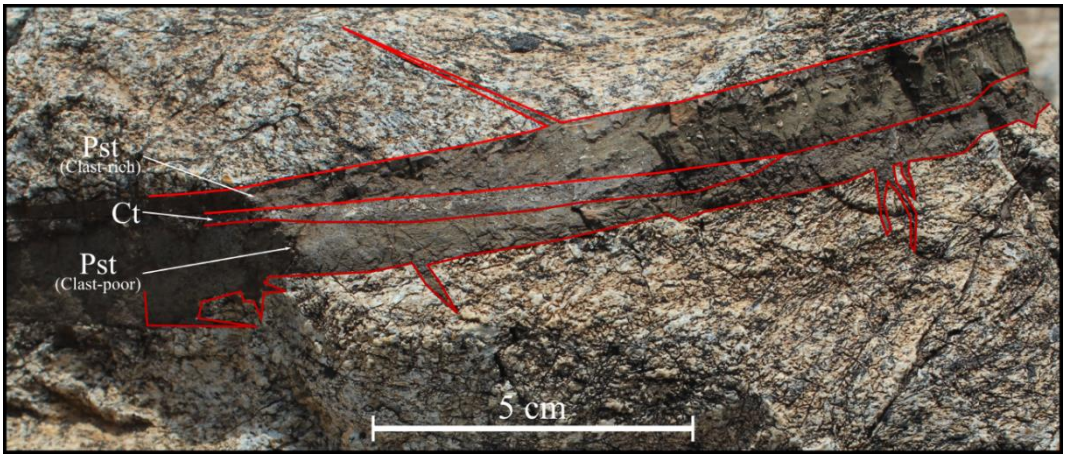


Figure 3.22: Outcrop photograph of a pseudotachylite GPPD with two pseudotachylites, clast-rich and clast-poor, within the GPPD (outlined by red lines). The GPPD has sharp contacts with the highly fractured anorthosite. Injection veins extend downward and have an irregular shape. The photo is of a boulder and therefore unoriented. Pst is pseudotachylite, Ct is cataclasite. See Figure 3.10 for photograph location.

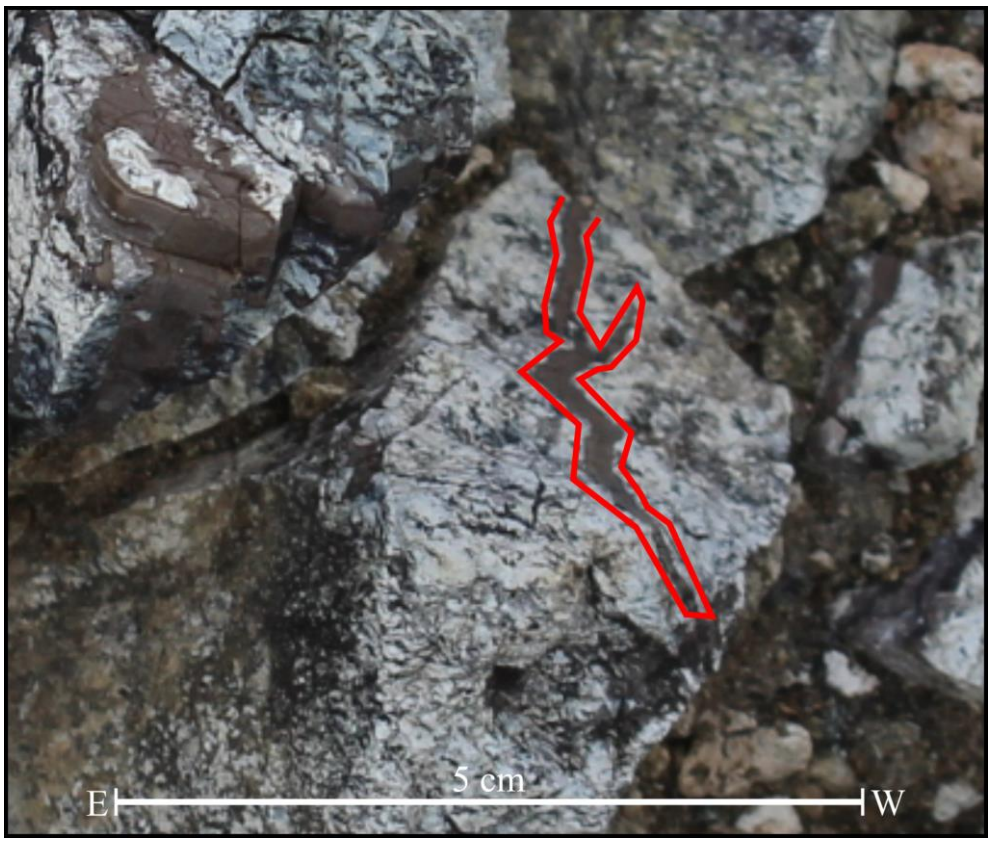


Figure 3.23: Outcrop photograph of a pseudotachylite injection dyke with conjugate form (traced by the red lines). The photographed surface is subparallel to the layer-parallel fracture surface.

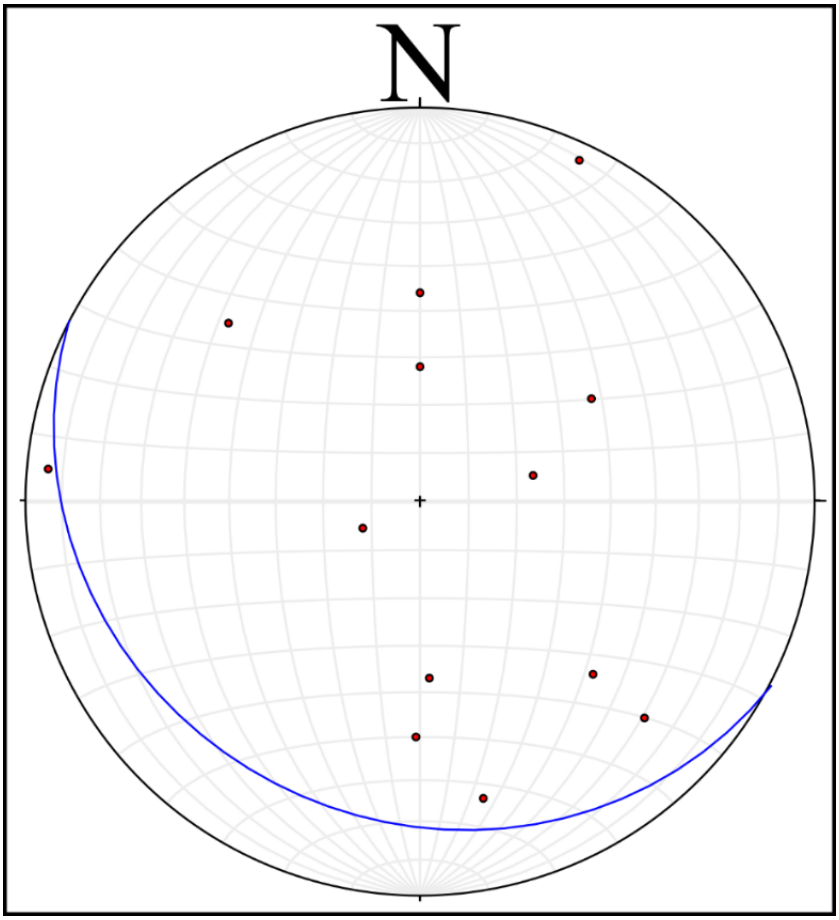


Figure 3.24: Equal area stereoplot of poles to pseudotachylite injection veins (n= 13, red dots with black outline) and average plane to magmatic layering (blue line).

Pseudotachylite dykes are distinguished from the other fault rocks by the XPL opaque, cryptocrystalline matrix with clasts of plagioclase and chromite. The PPL colour of pseudotachylite varies from dark greenish-brown to light brown.

In thin section, the GPPDs show sharp planar contacts with the chromite-foliated anorthosite, irrespective of the rotation of the foliation (Figure 3.25). Contacts between GPPDs and cataclasites may be sharp, diffuse, planar, or irregular to convoluted (Figure 3.25). Contacts with the breccias are typically sharp but irregular, whereas the contacts with the cataclasite are sharp when crosscut by pseudotachylite but diffuse and irregular to convoluted, particularly where the cataclasite is within a GPPD or parallel to one (Figure 3.25, dashed yellow line).

Injection veins extend from the GPPDs both up and down into relatively undeformed fault rock, however one direction (downward in oriented samples) is favoured, producing longer and thicker veins (Figure 3.26). These veins have sharp boundaries with the relatively undeformed fault rock. Where the veins inject into a deformation zone (fault rock bounded by two GPPDs) the veins form irregular vein networks (Figure 3.27).

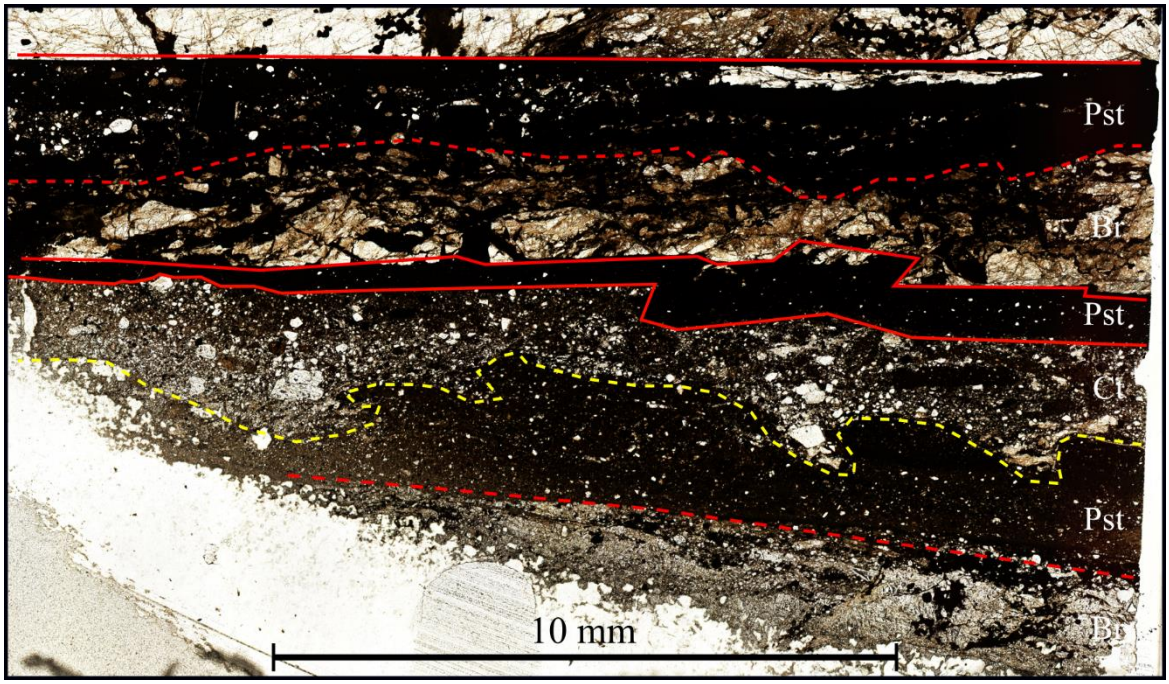


Figure 3.25: PPL photomicrograph of the lower portion of MHJL-006A thin section. The image focuses on the pseudotachylite-cataclasite relationship. The solid red lines trace sharp pseudotachylite contacts whereas the dashed lines show diffuse boundaries with breccia or cataclasite. The dashed yellow line traces a convoluted and diffuse pseudotachylite. Pst is pseudotachylite, Ct is cataclasite, Br is breccia.

Pseudotachylite, in both the GPPDs and injection veins, is distinguished on colour and clast content (Figure 3.25). Pseudotachylite with a darker greenish-brown colour, both in GPPDs and injection veins, is crosscut by light brown pseudotachylite. Furthermore, dark green pseudotachylites are crosscut by more fractures compared to light brown pseudotachylites; the latter typically have smaller displacements along fractures that crosscut multiple generations (Figure 3.27). Colour banding occurs in both darker and lighter brown pseudotachylites but is most recognisable in the light brown pseudotachylites (Figure 3.28). The reason for the colour variation within the pseudotachylites is cryptic in thin section.

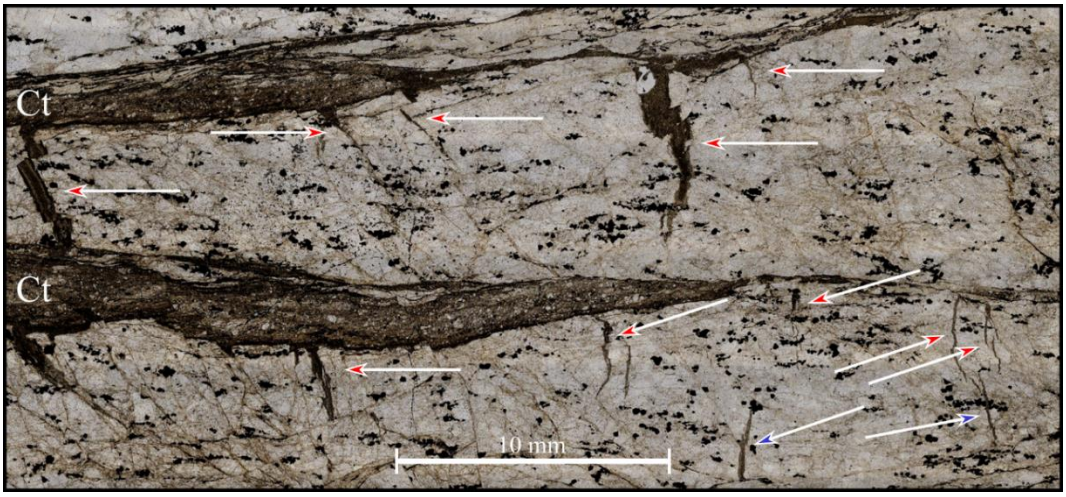


Figure 3.26: PPL photomicrograph of the MHJL-009 thin section, emphasizing the preferential direction of pseudotachylite injection veins and showing a cataclasite (Ct) that crosscuts a pseudotachylite injection vein. Both cataclasites have pseudotachylite at their margins. The cataclasite and pseudotachylite are crosscut by high-angle, normal-sense fractures. The host rock is highly fractured chromite-foliated anorthosite. The white arrows with red fill mark downward injecting pseudotachylite veins. The white arrows with blue fill mark upward injection veins. The sample is unoriented, therefore the directions are relative. See chapter 4 for TIMA analysis of the leftmost pseudotachylite injection vein crosscut by the cataclasite.

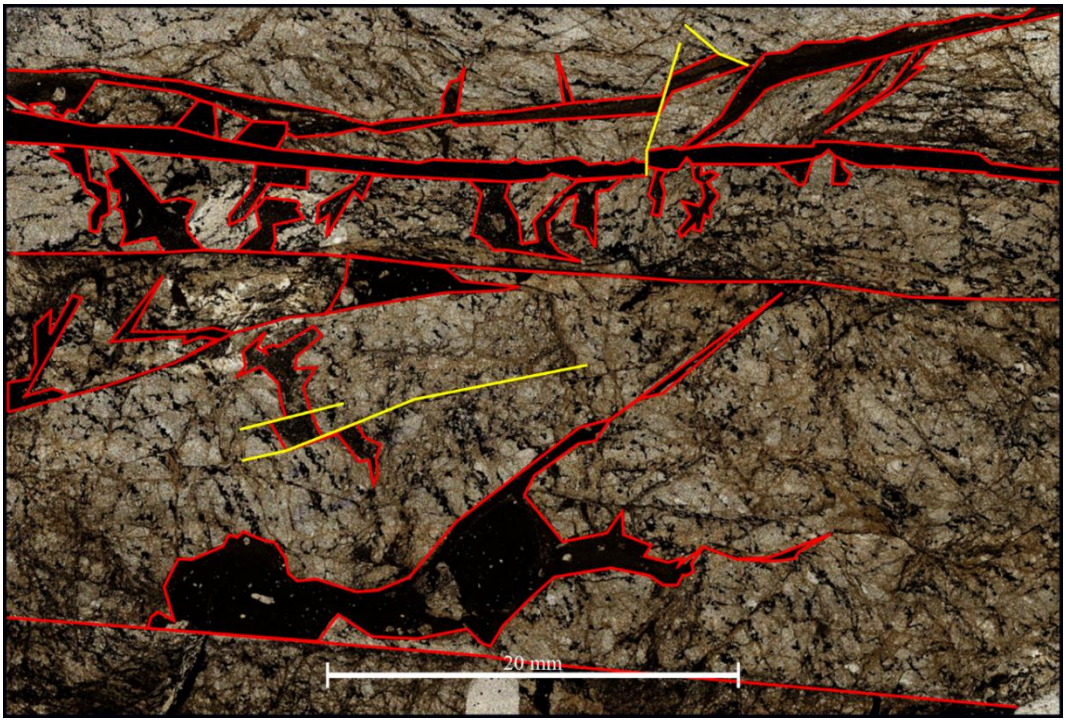


Figure 3.27: Photomicrograph of thin section MHJL-008E in PPL. The sample shows disruption of the older GPPDs (fractures traced by yellow lines) in the upper part of the image but not the younger GPPDs in the lower part of the image (all are traced with solid red lines). The sample also shows irregular injection vein networks between the GPPDs. The host rock is highly fractured chromite-foliated anorthosite. The sample is unoriented, therefore the directions are relative.

The various pseudotachylites may be further distinguished based on the abundance and mineralogy of clasts; with clast-absent, plagioclase-dominated and chromite-dominated pseudotachylite varieties identified (Figure 3.28). Clast-absent pseudotachylite is classified as lacking visible clasts in thin section and is uncommon. Plagioclase-dominated pseudotachylite contains both mono- and polycrystalline, rectangular clasts of plagioclase, up to 5 mm in length. Chromite clasts are typically spherical and up to 0.5 mm in diameter. These clasts are disseminated throughout the plagioclase-dominated pseudotachylite but contribute <20% of the pseudotachylite volume. Chromite-dominated pseudotachylite lacks both mono- and polycrystalline clasts of plagioclase. Chromite clasts within these pseudotachylites are ≤0.5 mm with most clasts being ≤0.1 mm.

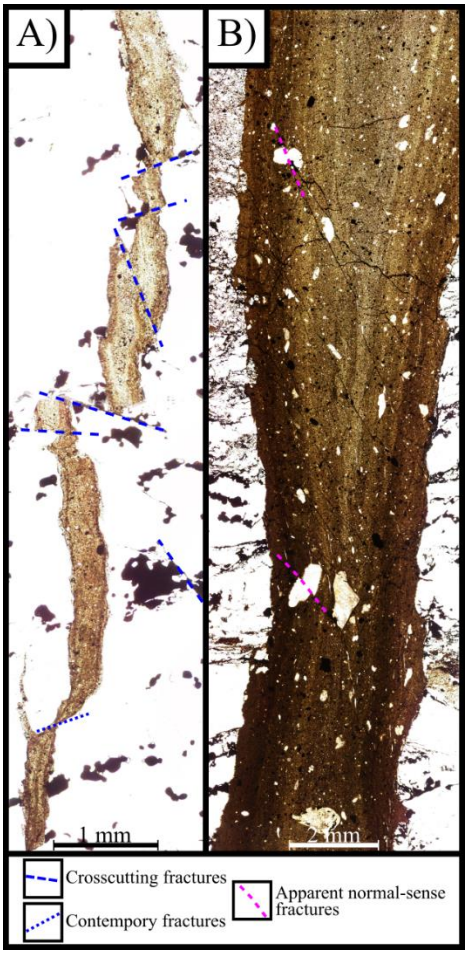


Figure 3.28: PPL photomicrographs of pseudotachylite injection veins from MHJL-006A (A) and MHJL-008D (B). A) shows light brown, chromite clast-dominated pseudotachylite with banding, pseudotachylite-crosscutting fractures with a consistent top-to-right displacement sense and a fracture contemporaneous with pseudotachylite generation. B) shows dark brown, plagioclase clast-dominated pseudotachylite. Several clasts within pseudotachylite appear to be crosscut by oblique, normal-sense shear fractures, however, these displacements are not observed within the colour banding adjacent to the clasts. A) has higher exposure than B) so that the colour banding is visible, giving the appearance that A) has a lighter colour than B). See Chapter 4 for TIMA analysis of both samples. The samples are unoriented, therefore the directions are relative.

3.3.4 Cataclasite and breccia

The eastern outcrop (35J 0793114 mE 7312863 mN, Figure 3.29) of the chromite-foliated anorthosite exposed on Jagdlust Farm displays cataclasite, which underlies the GPPDs. The cataclasite under each GPPD grades into breccia on a mm-scale. The cataclasites underlying the GPPDs are up to 5 cm thick. The breccia underlying each cataclasite is up to 30 cm thick and typically grades into fractured chromite-foliated anorthosite over 10 cm but may have sharp lower contacts, locally. Where breccia underlies cataclasite (and locally GPPDs) the breccia is interpreted as a damage zone around the fractures, which contain cataclasite or pseudotachylite (Chester and Logan, 1987; Torabi and Berg, 2011). Therefore, fault rock, which occurs as a gradation of cataclasite into breccia is referred to as cataclasite.

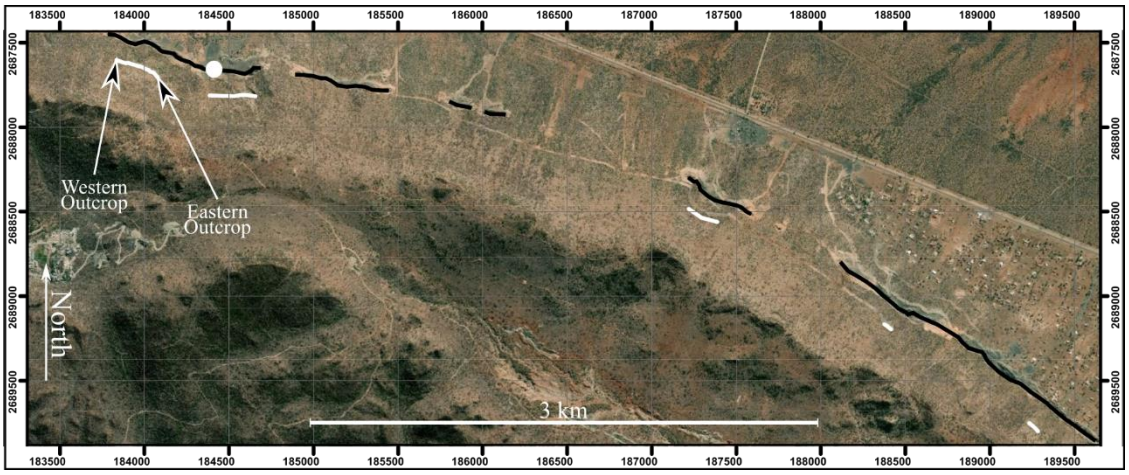


Figure 3.29: Satellite image of the study area with Western and Eastern outcrop on Jagdlust Farm indicated. The white and black lines trace outcrop of the chromite-foliated anorthosite and LG-6 chromitite, respectively. The white dot marks the location of The LG-6 chromitite reverse fault. UTM Grid 35J (Esri, 23 June 2013).

Cataclasite, which underlies the GPPD at the MG-4 chromitite contact is <5 cm thick, having a smaller (~10 cm) underlying brecciated zone compared to the cataclasites toward the middle of the chromite-foliated anorthosite. Clasts within the cataclasites are ≤2 mm and constitute <30% volume of the fault rock (Higgins, 1971; Passchier and Trouw, 2005). The upper contact of these cataclasites is typically sharp with the overlying GPPD, the lower contacts are irregular with the fault rock filling the space created by the intersection of east and west-dipping normal-sense shear fractures with the layer-parallel GPPDs (Figure 3.19). The east and west-dipping shear fractures have displacement <2 cm (Figure 3.30).

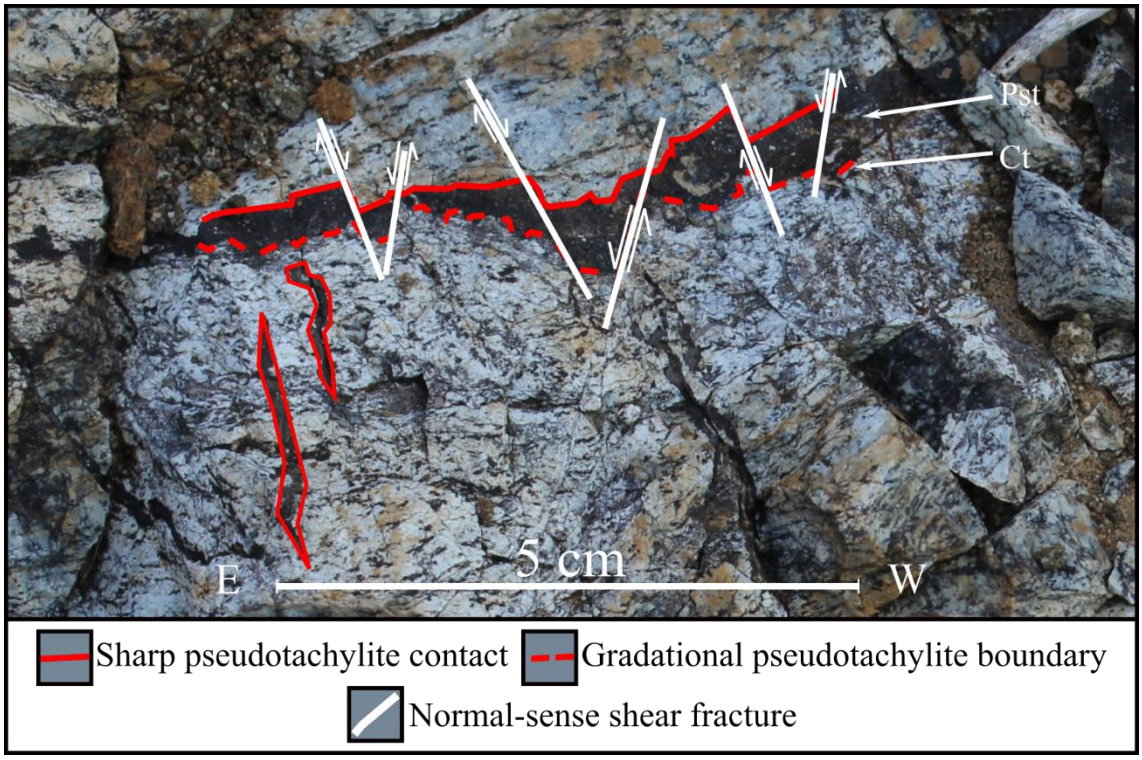


Figure 3.30: Outcrop photograph showing normal-sense shear fractures, which displace a GPPD and underlying breccia. See Figure 3.10 for photograph location.

The cataclasite fault rock underlying the GPPDs towards the middle of the chromite-foliated anorthosite is ≤5 cm thick and the breccia that underlies the cataclasite is up to 30 cm thick. The cataclasite gradation here is ~5 cm; the maximum clast size increases from ≤2 mm to >10 cm. The matrix volume decreases from >50% to <1% as the cataclasite grades into the breccia.

Cataclasite is aphanitic in hand sample, ranging in colour from brown to grey. The matrix within the breccias is also aphanitic, with colours ranging between light grey, brown and black, matching the colour of the cataclasite from which it grades. The clast size in the breccias depends on the thickness of the zone; the thickest zones, ~30 cm, have clasts 10's cm in diameter (Figure 3.31). In both, clast-shape also varies between subrounded to angular, with clasts displaying a greater rotation of the magmatic foliation being more rounded than those displaying less rotation.

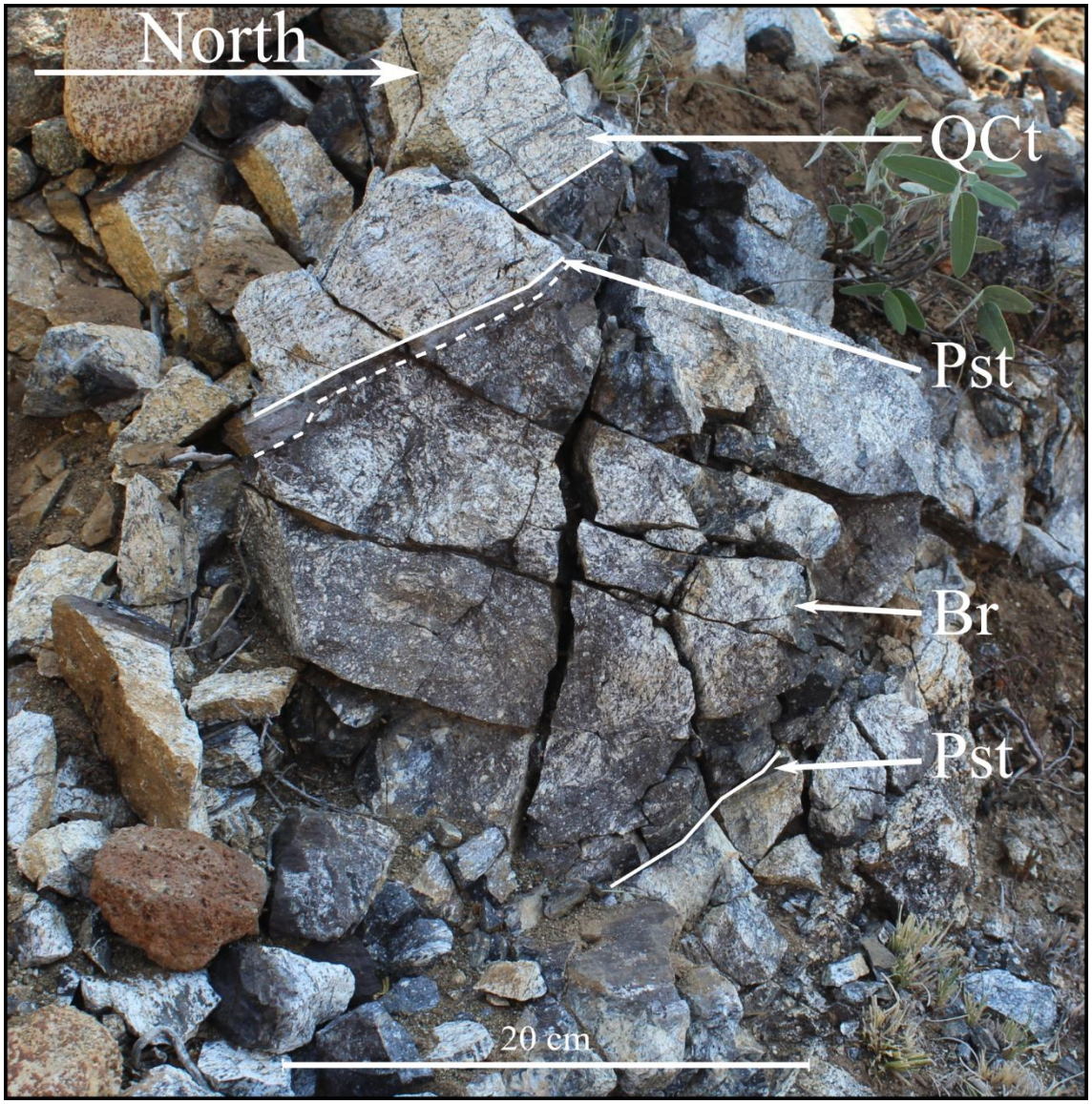


Figure 3.31: Outcrop photograph of two GPPDs (Pst) bounding a breccia (Br). The upper GPPD crosscuts a sigmoidal-fabric, quasi-ductile cataclasite (QCt). Both GPPDs are underlain by cataclasite, which grades into breccia. The solid white line traces the sharp contact between the quasi-ductile cataclasite and pseudotachylite. The dashed white line shows the transition from pseudotachylite to cataclasite or breccia. See Figure 3.10 for photograph location.

The fault rock exposed in the western outcrop (35J 0793009 mE 7312898 mN, Figure 3.29) of the chromite-foliated anorthosite on Jagdlust Farm has comparably less cataclasite than the fault rock exposed in the eastern portion. In this area, cataclasite fills anastomosing fractures and does not grade into breccia but rather has sharp boundaries with the brecciated chromite-foliated anorthosite (Figure 3.32). Furthermore, these cataclasite-fill fractures have a P'-fracture orientation with respect to the GPPD orientation, although the displacement sense is unclear (Figure 3.32A). These P' fractures are crosscut by steeply north-dipping fractures with a reverse displacement sense, forming an angle with the GPPDs comparable to R'-shear fractures (Figure 3.32A).

The chromite-foliated anorthosite is brecciated by P-, P'- and R'-shear fractures with the magmatic foliation rotated variably through the zone (Figure 3.32A). The clast sizes within the breccia are obscured owing to a lack of matrix (<1%). As the clasts are defined by fractures and the magmatic foliation is moderately rotated, the fault rock is interpreted as a crackle breccia (Norton, 1917; Shukla and Sharma, 2018).

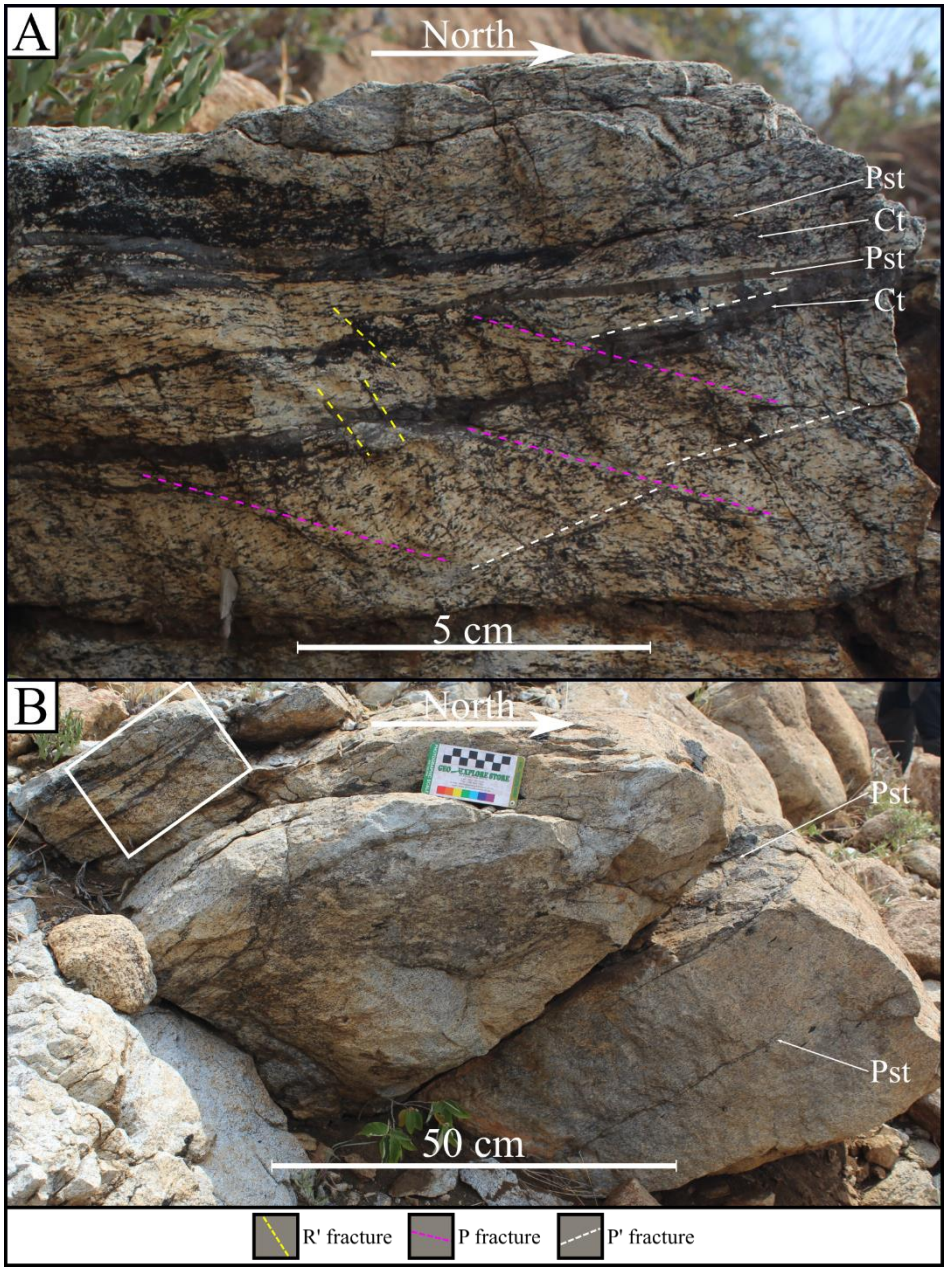


Figure 3.32: Outcrop photograph showing the pseudotachylite, cataclasite and fracture relationships in the Jagdlust Farm western outcrop. A) Shows the cataclasite relationship as well as the P'-fracture orientation of the cataclasite to the pseudotachylite GPPD. B) is a broader photograph of the outcrop from which photograph A) was taken. The white box indicates the position of A). See Figure 3.10 for photograph location.

In thin section, the matrix of the cataclasite ranges in colour from pale green to brownish-green, with grain size ranging from cryptocrystalline to ~0.1 mm (Figure 3.33). Visible matrix grains range from subrounded to subangular and comprise of monocrystalline plagioclase and chromite grains. Clasts within the matrix consists of monocrystalline plagioclase to polymineralic chromite-foliated anorthosite or fault rock.

The boundary between cataclasite and breccia is gradational with larger clasts becoming dominant downwards (Figure 3.34). Clast size within the breccia is bimodal with clast lengths of ≤1 mm and ≥2 mm (Figure 3.34). The matrix comprises of cryptocrystalline to ~0.1 mm and constitutes ≤30 % volume of the breccia.

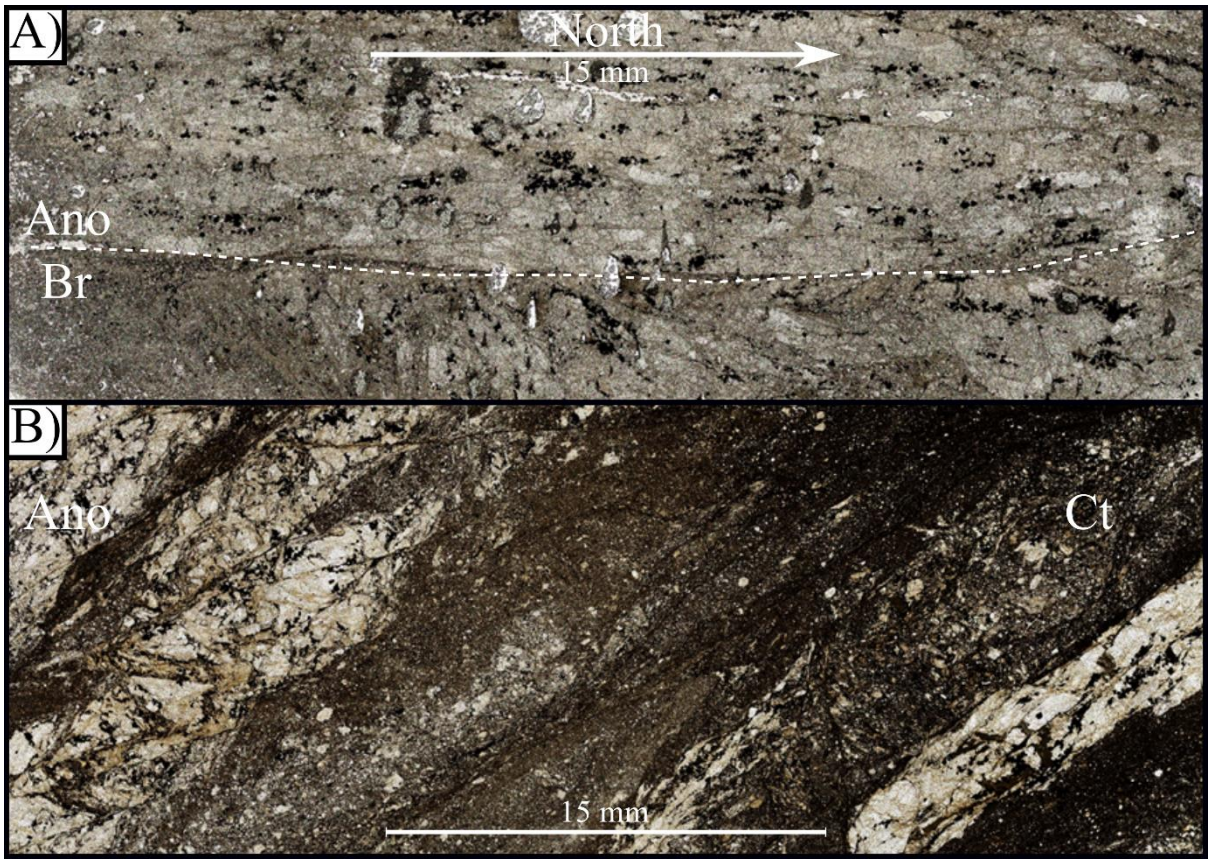


Figure 3.33: A) PPL photomicrograph of the lower part of MHJL-002 thin section showing the contact of the overlying anorthosite with the underlying cataclasite. B) PPL photomicrograph the lower part of MHJL-008C thin section showing cataclasite and polycrystalline clasts of chromite-foliated anorthosite.

Alteration is pervasive throughout the cataclasite, producing various shades of green within the cataclasite and associated fractures. The product of alteration is cryptic owing to the cryptocrystalline nature.

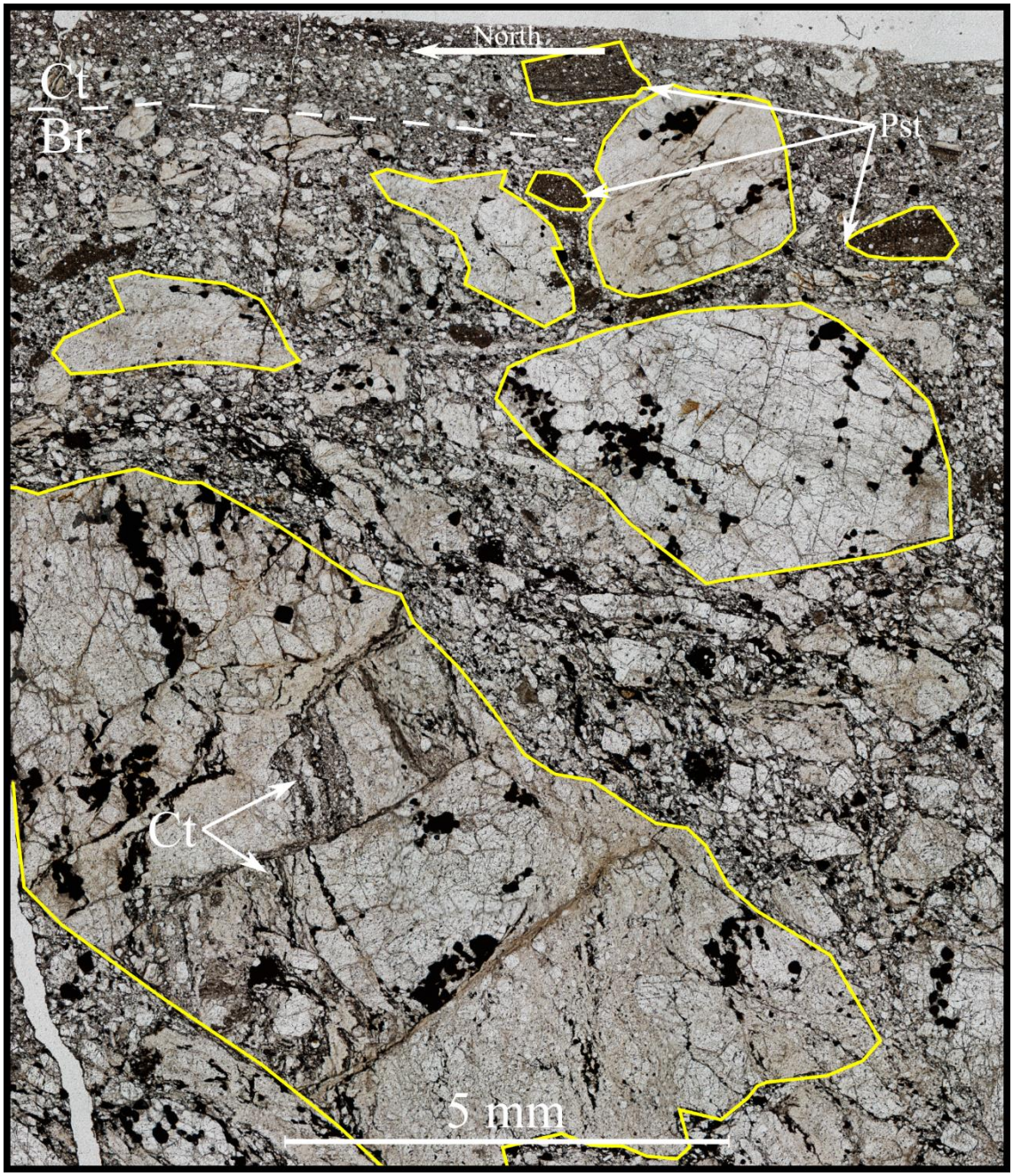


Figure 3.34: PPL photomicrograph of the MHJL-003 thin section showing the diffuse to gradational boundary of cataclasite with underlying breccia (dashed white line, see Chapter 4 for TIMA analyses of the various clasts). Several polymineralic clasts of pseudotachylite, cataclasite and chromite-foliated anorthosite are evident (outlined in yellow). Clasts with cataclasite show fractures that crosscut the cataclasite at a high-angle.

3.3.5 Crosscutting relationships between fault rock types

Fault rocks

Both the upper and lower quasi-ductile cataclasites are crosscut by the pseudotachylite and cataclasite fault rocks (Figure 3.14 and Figure 3.31).

Pseudotachylite may crosscut older generations of pseudotachylite; GPPDs and injection veins both crosscut each other. Typically, GPPDs only crosscut injection veins if the source and crosscutting GPPDs are within 2 cm of each other. Upward injection veins are not seen to crosscut GPPDs overlying the GPPD from which they extend. Downward extending injection veins may crosscut GPPDs up to 15 cm below the GPPD from which they extend. These injection veins, however, may be displaced along the upper contact of the GPPD even where they crosscut the pseudotachylite within the GPPD.

Furthermore, pseudotachylite is seen to crosscut, comingle and be crosscut by cataclasite. GPPDs that overlie cataclasite typically have sharp boundaries, however, a few have diffuse to comingled boundaries. Injection veins extending down from these GPPDs crosscut the cataclasite and underlying GPPDs. The injection veins typically have sharp boundaries with the fault rocks underlying the GPPD from which they extend, however, locally the injection veins may have diffuse boundaries with the cataclasite in direct contact with the GPPD from which they extend (Figure 3.21C). Also, clasts within the cataclasite locally consist of pseudotachylite as well as the other fault rocks (Figure 3.34 and Figure 3.35A).

Fractures

Throughout all the samples, foliation-parallel fractures are seen in chromite-foliated anorthosite clasts within the various fault rocks and in the wallrock (Figure 3.12, Figure 3.13, Figure 3.16 and Figure 3.33). The fractures have anastomosing to discrete planar forms and are <1 mm thick. The fractures are crosscut by both steep and shallow foliation-oblique fractures described within the chromite-foliated anorthosite fault.

Pseudotachylite-bearing fractures and the cataclasites are crosscut by both reverse- and normal-sense shear fractures of various orientations (Figure 3.31 and Figure 3.35B). The degree of displacement varies along the shear fracture; younger pseudotachylite generations have the least to no displacement and the older have the greatest degree of displacement along the shear fractures. The maximum displacement parallel to movement direction is unclear owing to the layer-parallel nature of the fault and unfavourable outcrop orientation. The maximum displacement observed, in an E-W direction, for layer-parallel and layer-oblique fractures is 2 cm and 5 cm, respectively (Figure 3.19 and Figure 3.35B)

Layer-oblique fracture density within the chromite-foliated anorthosite increases upwards from the base of the layer to the contact with the MG-4 chromitite. The density increase, from ≥10 to ≤2 cm spacing, is accompanied by decreased fracture length from >10 to ≤2 cm. Poles to various fracture surfaces are plotted in Figure 3.36, however, fracture orientations are not sufficiently consistent to obtain general fracture trends from the pole data.

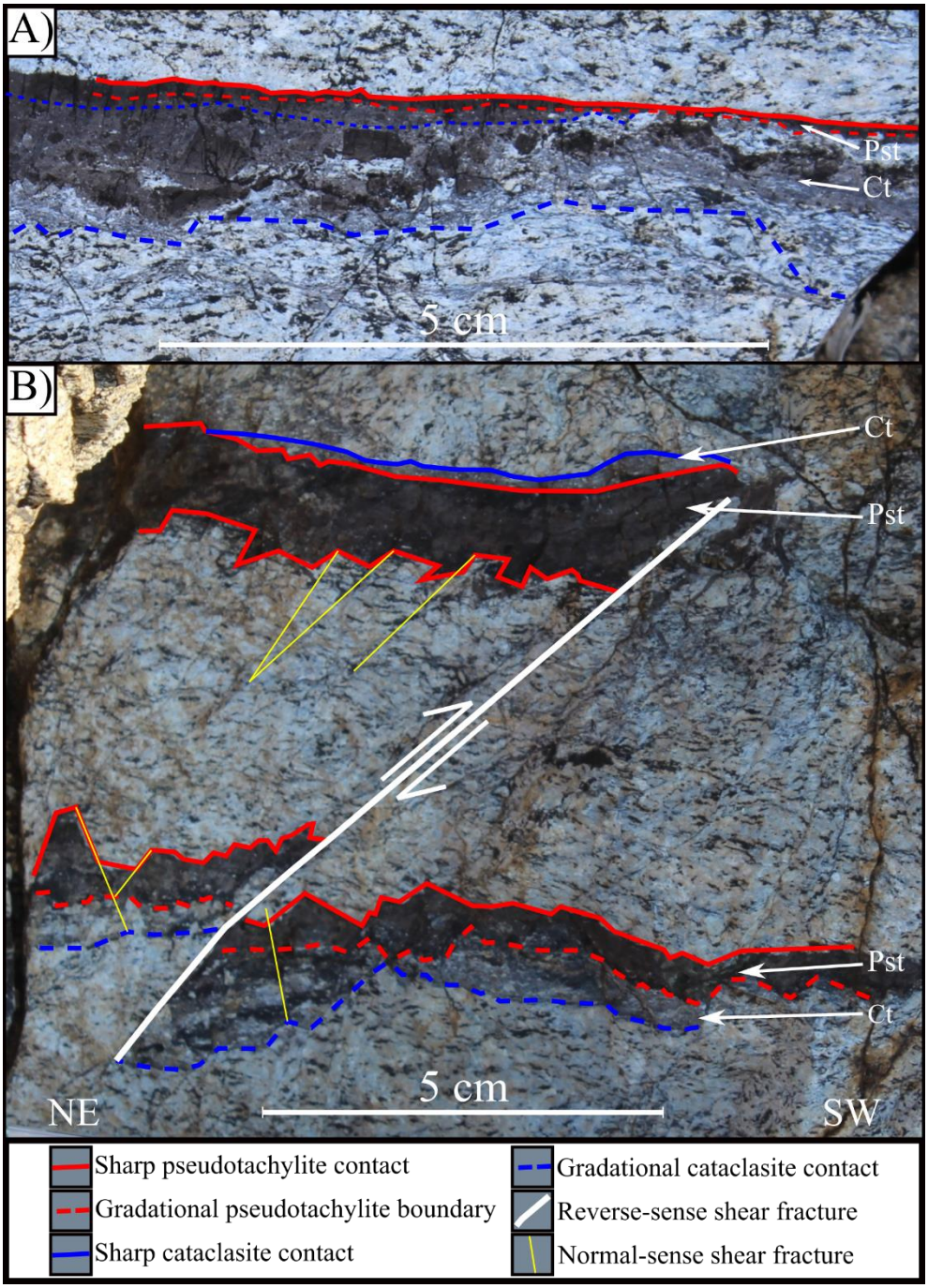


Figure 3.35: Outcrop photographs of the various crosscutting relationships of fault rocks. A) shows pseudotachylite clasts within a younger pseudotachylite-cataclasite generation. B) shows a reverse-sense displacement shear fracture crosscutting two GPPDs. The lower GPPD is disrupted to a greater degree by crosscutting fractures than the upper GPPD. The lower surface of the upper GPPD is disrupted by normal-sense and reverse-sense shear fractures. The upper surface, however, is not crosscut by these fractures and neither is the overlying and crosscut cataclasite, implying the normal- and reverse-sense shear fractures were coeval to the generation of the upper GPPD as the fractures do not propagate into the pseudotachylite. See Figure 3.10 for photograph location.

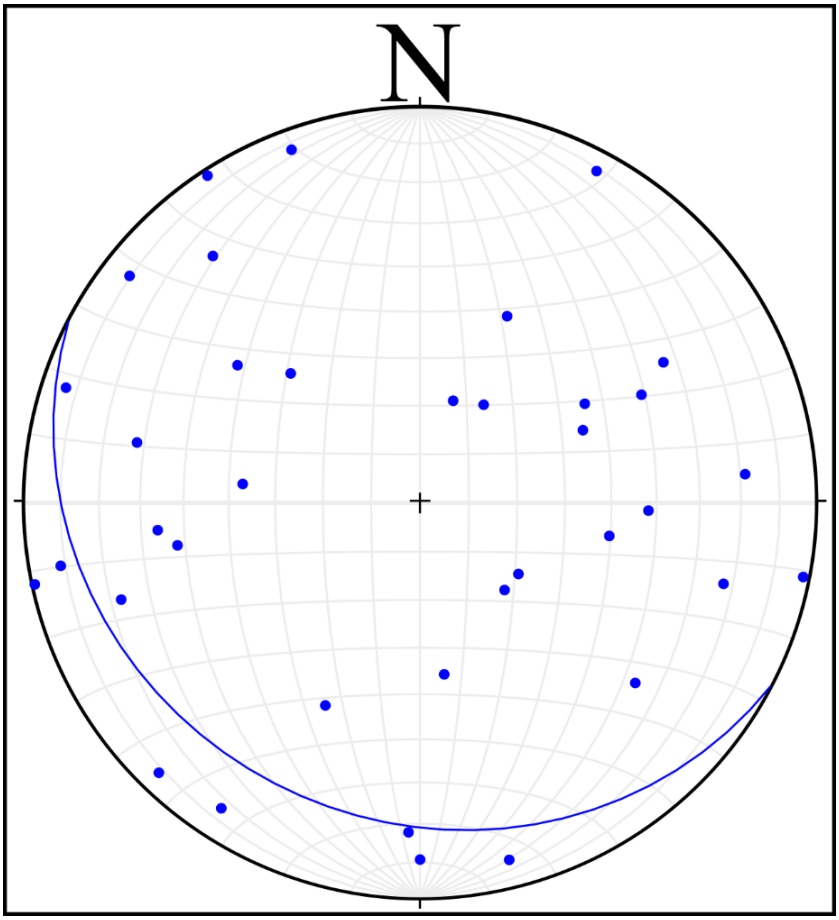


Figure 3.36: Equal area stereoplot of the poles to pseudotachylite-absent fractures within the chromite-foliated anorthosite layer (n=33). The blue line is the average plane to magmatic layering.

Dykes and sills

The various dykes and sills that were seen within the study area all terminated against the chromitite-foliated anorthosite, albeit those crosscutting the stratigraphy below the chromite-foliated anorthosite fault terminate against the base of the layer rather than at the fault surfaces. Those that crosscut the overlying stratigraphy terminate against the chromitite-anorthosite fault surface.

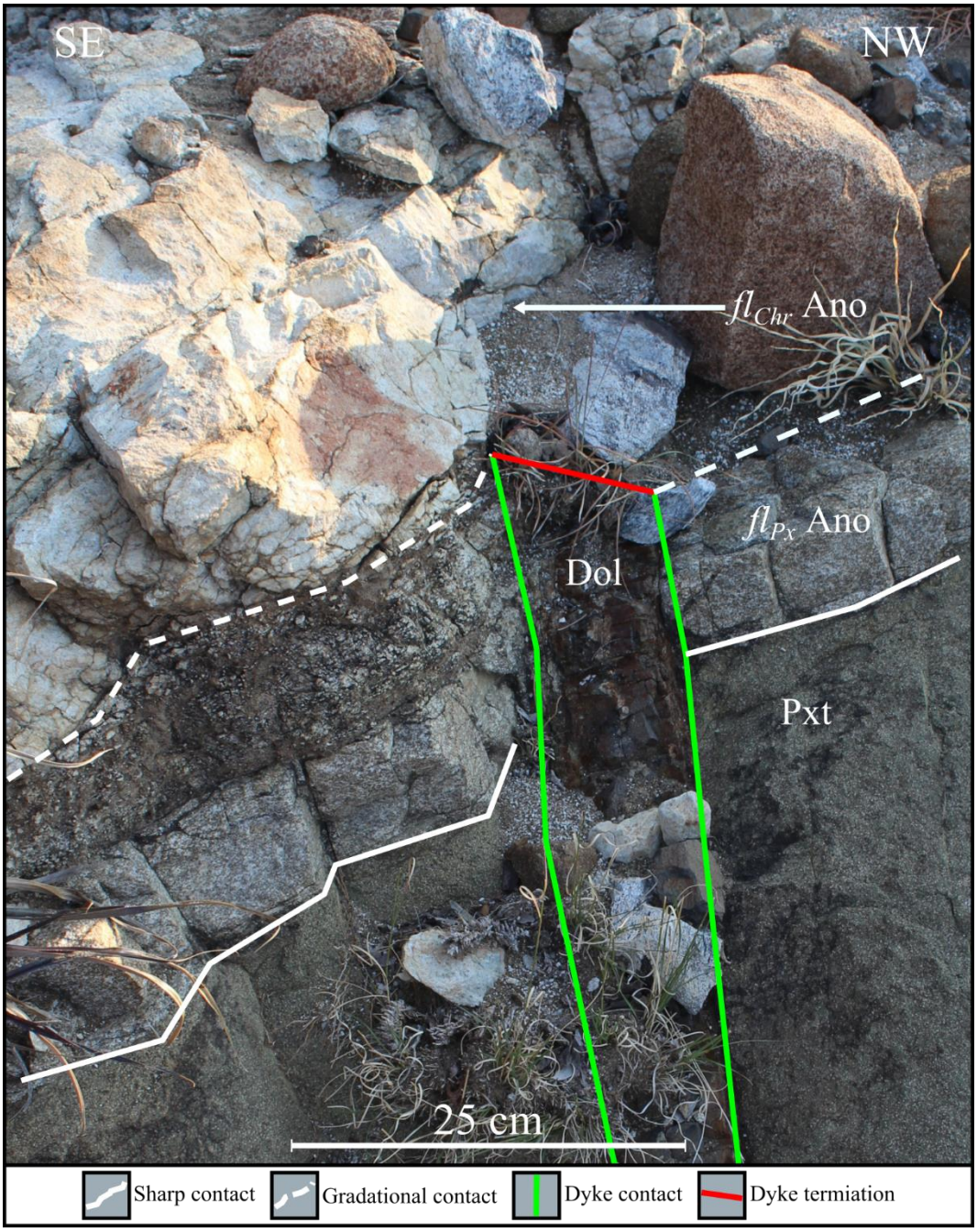


Figure 3.37: Outcrop photograph of a dolerite dyke (Dol) terminating against the base of the chromite-foliated anorthosite (fl_{Chr} Ano). The dyke crosscuts the underlying pyroxenite (Pxt) and pyroxene-foliated (fl_{Px} Ano) base of the chromite-foliated anorthosite.

3.3.6 Comparison of the chromite-foliated anorthosite to the other magmatic lithologies

The various fault rocks described above are absent in the pyroxenites and anorthosites near the lower-upper Critical Zone boundary. Furthermore, the pyroxene-foliated sub-layer at the base of the chromite-foliated anorthosite lacks the described fault rocks, which are restricted to the middle and top of the chromite-foliated anorthosite layer. It is unclear whether the fault rocks are present in the base of the MG-4 chromitite overlying

the chromite-foliated anorthosite owing to the friable nature and poor preservation of the base, however, the fault rocks are absent in the upper portion of the MG-4 chromitite layer and overlying pyroxenite.

Fractures within the upper and middle pyroxenites, pyroxene-foliated anorthosite and lower pyroxenite series have >10 cm spacing-densities with all fractures being >20 cm in length. Fractures are typically open, a few, however, have a white aphanitic fill. Poles to the various fractures are plotted in Figure 3.38, however, fracture orientations are not sufficiently consistent to determine fracture trends from the data.

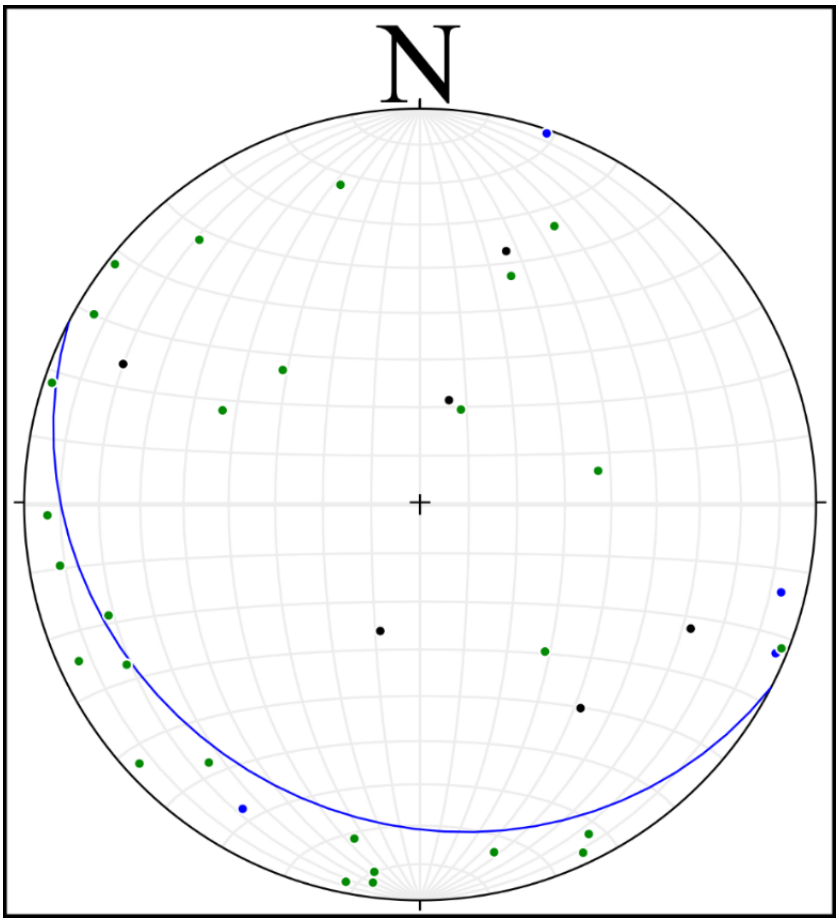


Figure 3.38: Equal area stereoplot of poles to fractures from the various lithologies outside the chromite-foliated anorthosite and chromite-foliated anorthosite fault. The blue, black, and green dots are poles to fractures in the pyroxene-foliated anorthosite (n=4), chromitites (n=6) and pyroxenites (n=27), respectively. The blue line is the average plane to magmatic layering.

The plagioclase within all the layers has undulatory extinction and deformation twins. Orthopyroxene grains show subvertical and subhorizontal cleavage fracture fabrics; one trend may dominate in individual samples (Figure 3.39). These intracrystalline fractures do not propagate into the adjacent clinopyroxene and plagioclase grains.

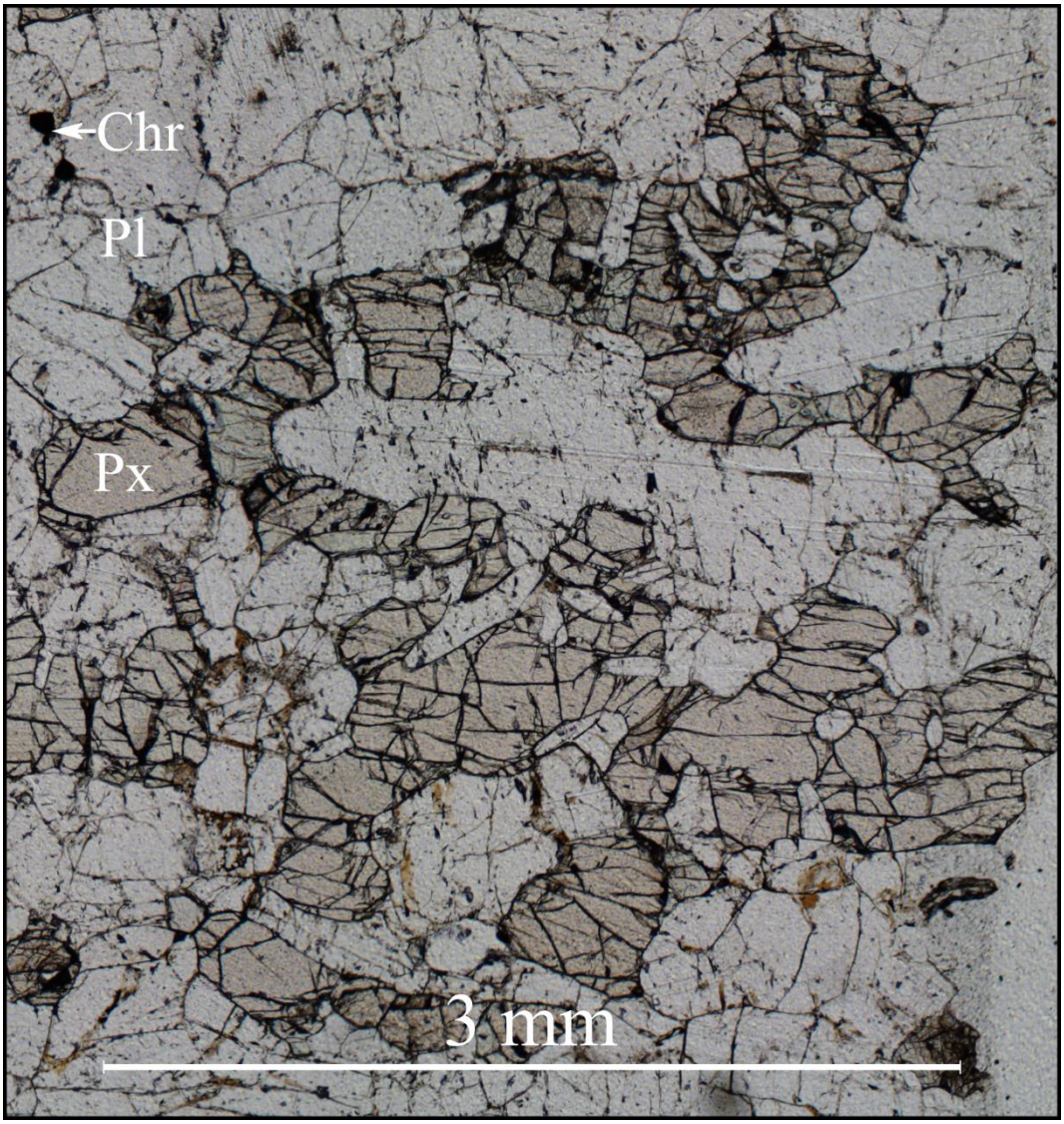


Figure 3.39: Photomicrograph of pyroxene grains within norite in thin section MHJL-005B emphasizing the greater density of intracrystalline fractures within the pyroxene grains compared to the surrounding plagioclase grains.

The green, cryptocrystalline alteration product described in the chromite-foliated anorthosite was not observed within any of the samples collected outside of the chromite-foliated anorthosite. The white aphanitic fracture fill observed in hand sample and outcrop was not preserved during thin section production.

3.4 The LG-6 chromitite reverse fault

The artisanal diggings on Jagdlust Farm and adjacent farms have exploited the LG-6 chromitite. These diggings have exposed an ~10 cm wide fault that crosscuts the LG-6 chromitite (Figure 3.29, Figure 3.10 and Figure 3.40). The fault has a similar strike to the chromite-foliated anorthosite fault further up stratigraphy but dips SSW more steeply, dipping at 67°→206° (Figure 3.41). The fault displays internal shear fractures with slickenlines plunging

at 59°→167° and displaces the LG-6 by 1.8 m along the digging's N-S wall profile in a top-to-north, reverse-sense.

The fault is highly altered and has both a pale olive-green, and a black aphanitic matrix. The black matrix has a weakly anastomosing form within the pale green matrix; the black matrix comprises <10% of the fault rock. Furthermore, a single injection vein extends from the fault into the footwall (Figure 3.42). The injection vein is ~2 mm wide and extends <10 cm, in a jagged fashion, into the footwall.

A second, <1 cm thick fault crosscuts the LG-6 chromitite (Figure 3.43). The fault is in the footwall of the reverse fault described above (Figure 3.40). The fault is subparallel to the diggings wall (dipping at 44°→260°, Figure 3.41) and has an apparent, ~10 cm, top-to-south displacement along the wall.

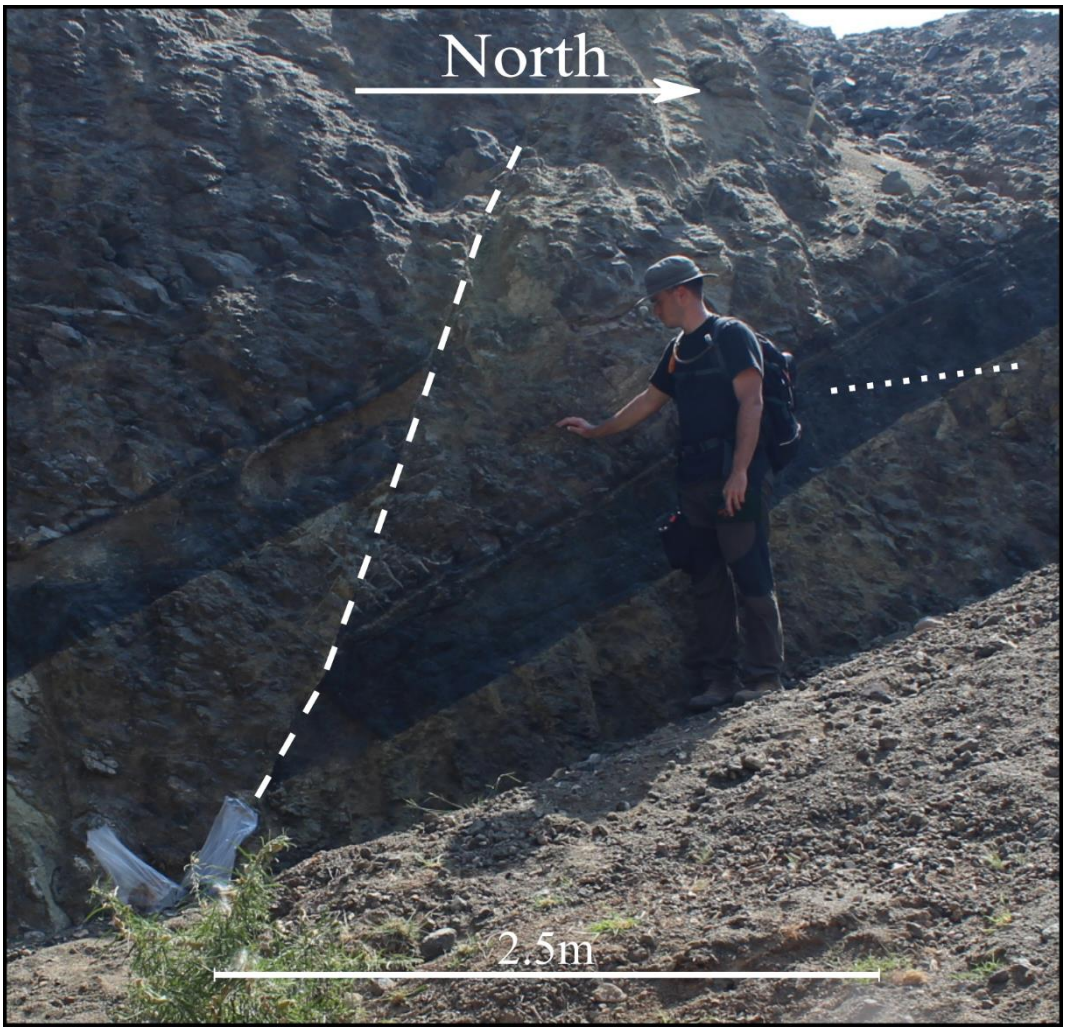


Figure 3.40: Outcrop photograph of the LG-6 chromitite and crosscutting faults. The main SSW-dipping fault is traced by the dashed white line. A smaller fault, subparallel to the diggings wall is traced by the dotted white line (Expanded in Figure 3.43). See Figure 3.10 for location (UTM 35J 0793361 mE 7312893 mN)

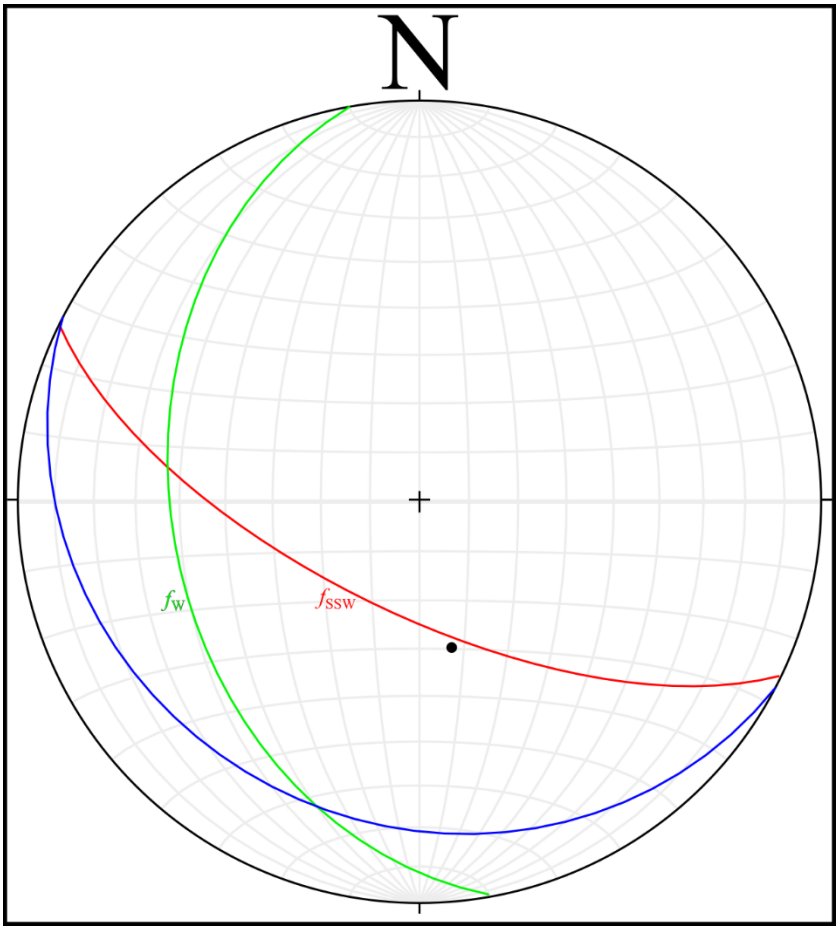


Figure 3.41: Equal area stereoplot of orientation data from the reverse fault crosscutting the LG-6 chromitite, SSW-dipping fault (red line labelled f_{SSW}, dipping at 67°→206°) and slickenlines on the reverse fault (black dot, dipping at 59°→176°), diggings wall-parallel fault (green line labelled f_W, dipping at 44°→260°) and average plane to magmatic layering (blue line labelled L_m).

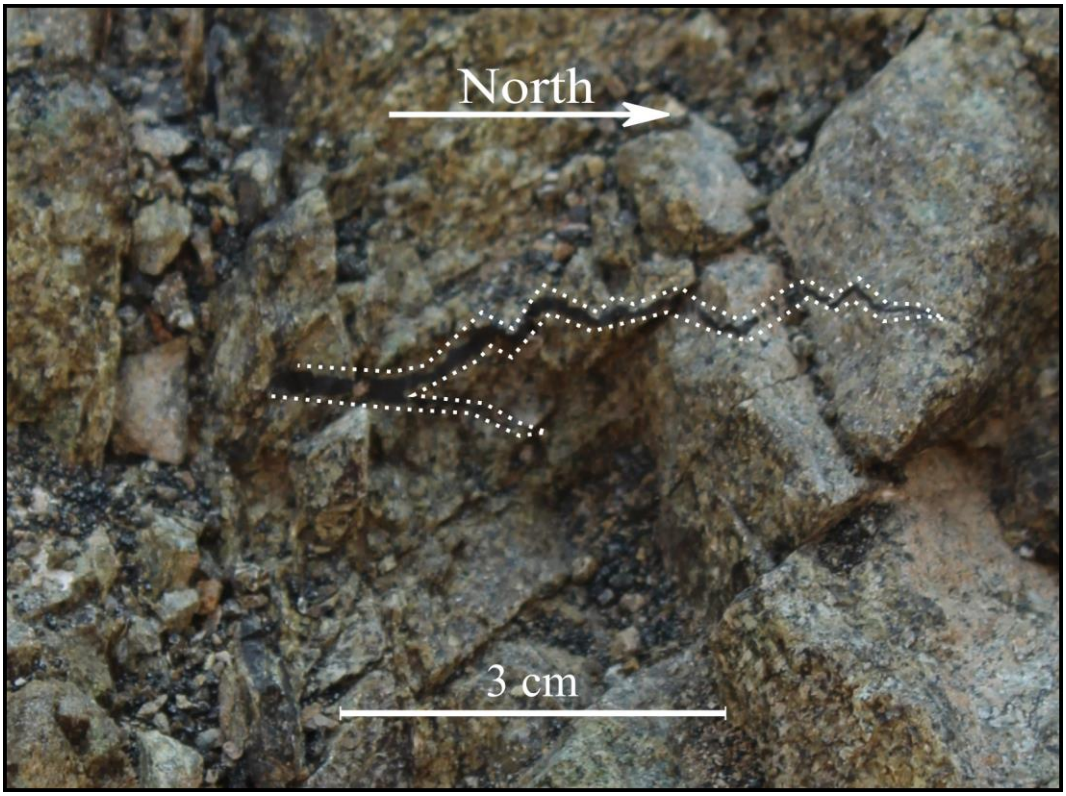


Figure 3.42: Outcrop photograph of an injection vein extending from the reverse fault crosscutting the LG-6 chromitite. The injection vein extends horizontally northward into the footwall of the fault and is outlined by the dotted white lines.

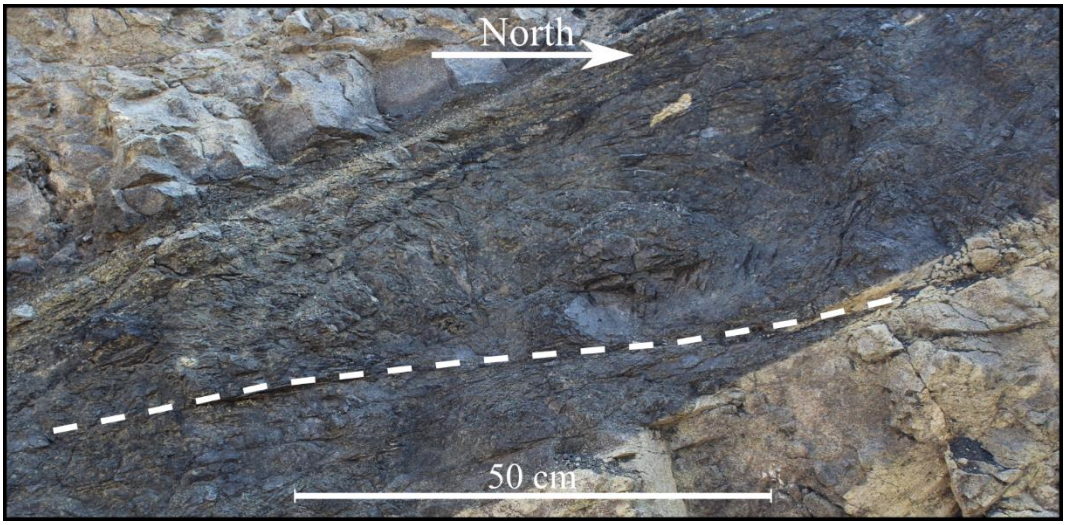


Figure 3.43: Outcrop photograph of the diggings wall parallel fault, traced by the dashed white line. The fault crosscuts the LG-6 chromitite in the footwall of the SSW-dipping reverse fault.

Layer-parallel fractures with ~8 cm fracture spacing are seen in the footwall chromitite layer (Figure 3.44). Between the layer-parallel fractures are (with respect to the layer-parallel fractures) oblique, north-dipping fractures with an ~2 cm fracture spacing. These oblique fractures are accompanied by gently oblique south-dipping fractures with an ~12 cm spacing.

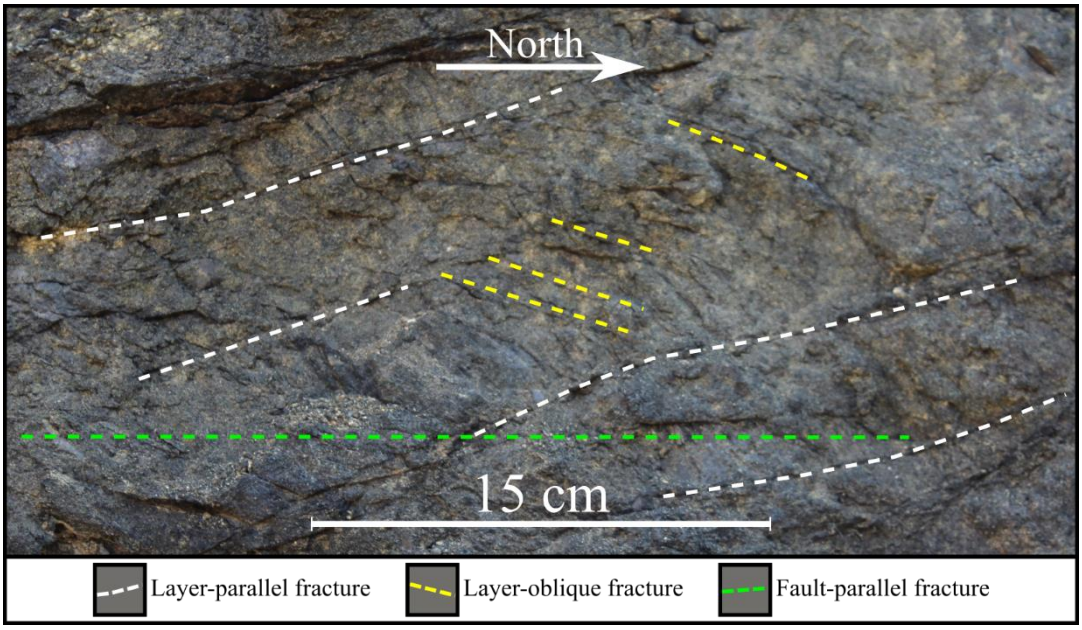


Figure 3.44: Outcrop photograph of the layer-parallel and oblique-fractures within the LG-6 chromitite in the footwall of the reverse fault. The fault-parallel fracture is parallel to the W-dipping fault in Figure 3.43.

A single large thin section was produced from the fault rock within the south-dipping reverse fault. The thin section shows feldspathic pyroxenite clasts within comminuted feldspathic pyroxenite, quasi-ductile cataclasite and fault-parallel, cataclasite-filled fractures (Figure 3.45).

The largest feldspathic pyroxenite clasts are >5 cm. The clasts show ~2 mm, equant orthopyroxene grains and interstitial plagioclase. The pyroxene grains are highly fractured by intracrystalline fractures. These fractures, however, do not propagate into the interstitial plagioclase. The clasts are surrounded by comminuted feldspathic pyroxenite. Within this comminuted matrix are subangular, mono- and polycrystalline plagioclase (<1.5 mm) and pyroxene (<1. mm) clasts. Epidote is pervasive through the cataclasite and along pyroxene fractures.

The fault-parallel fractures crosscut the feldspathic pyroxenite clasts and comminuted matrix. The fractures are planar but, locally have kinks or splays. The fractures are ~1 mm thick with cataclasite-fill consists of subrounded pyroxene and plagioclase grains (<0.1 mm). These fractures may have either a greenish-black or pale green colour. The fault-parallel fractures are displaced in a reverse-sense by steeply south-dipping fractures. These south-dipping fractures are interpreted as P’ fractures owing to the displacement sense and relative angle to the shear fractures (~20°). Furthermore, R fractures may form between the fault-parallel shear fractures.

The quasi-ductile cataclasite consists of <0.1 mm comminuted chromite aggregates that define a sigmoidal fabric within an olive-green cryptocrystalline matrix. The sigmoidal, comminuted-chromite aggregates form between fault-parallel shears.

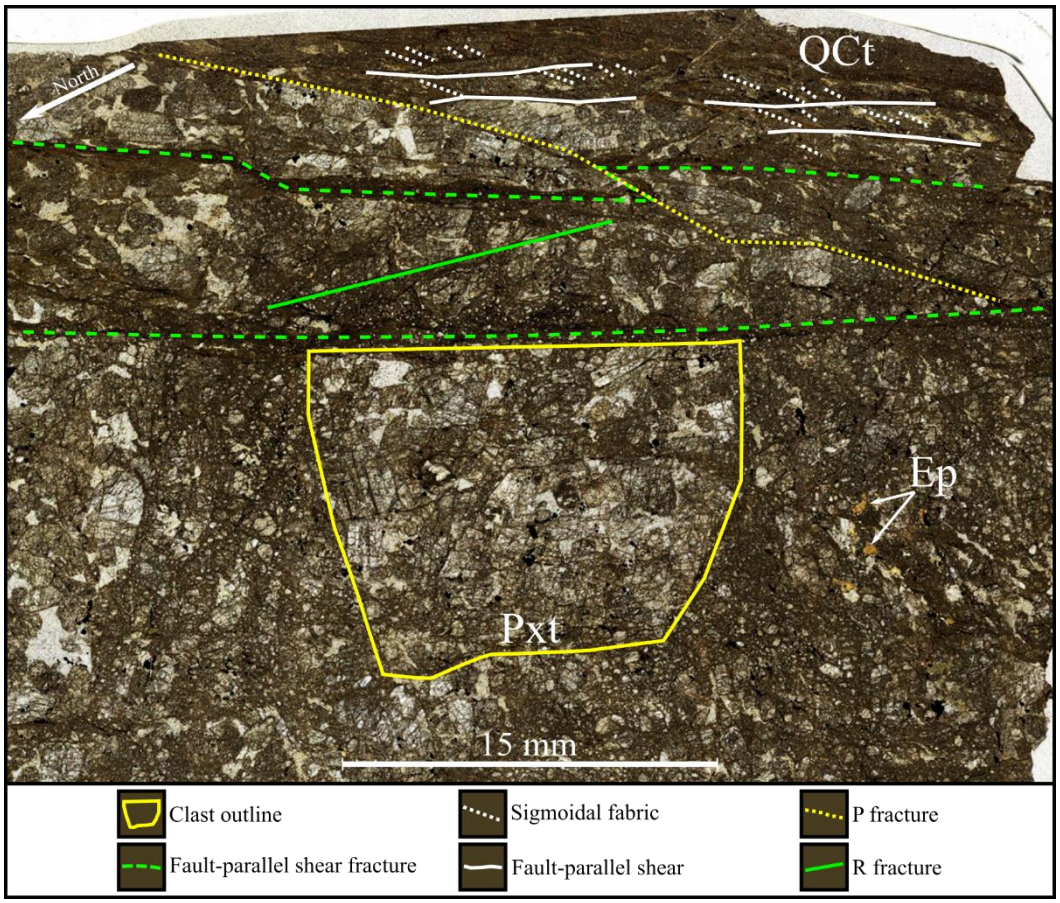


Figure 3.45: Photomicrograph of the fault rocks within the main, SSW-dipping fault crosscutting the LG-6 (Figure 3.40) in thin section MHJL-023. The thin section displays quasi-ductile cataclasite (QCt) with sigmoidal chromite-aggregate fabric, fault-parallel shears, P' fractures and R fracture. A feldspathic pyroxenite (Pxt) clast is traced for comparison of intracrystalline fracturing of pyroxene and plagioclase. Epidote (Ep) is observed in the matrix surrounding the outlined pyroxenite clast. Note that north is obliquely inclined to the edges of the thin section.

3.5 Kinematic Indicators

The primary form of kinematic indicator within the study area is slickenlines occurring on both fracture surfaces and the top surfaces of GPPDs. Slickenlines typically occur on layer-parallel fractures and are used in conjunction with P'-, R- and R'-fracture orientations, sigmoidal chromite aggregates and the reverse fault crosscutting the LG-6 chromitite to show a top-to-north displacement sense.

Slickenlines are found on fractures in the chromite-foliated anorthosite as well as in the underlying pyroxenites and chromitites. Within the chromite-foliated anorthosite, slickenlines form on pseudotachylite-deficient and

pseudotachylite-bearing fracture surfaces (Figure 3.46). The majority of slickenlines found on pseudotachylite-bearing fracture surfaces plunge 10° to 20° between SSE and SSW (Figure 3.47). It is only slickenlines on pseudotachylite-deficient fractures and fractures within the underlying chromitites that deviate from this grouping.

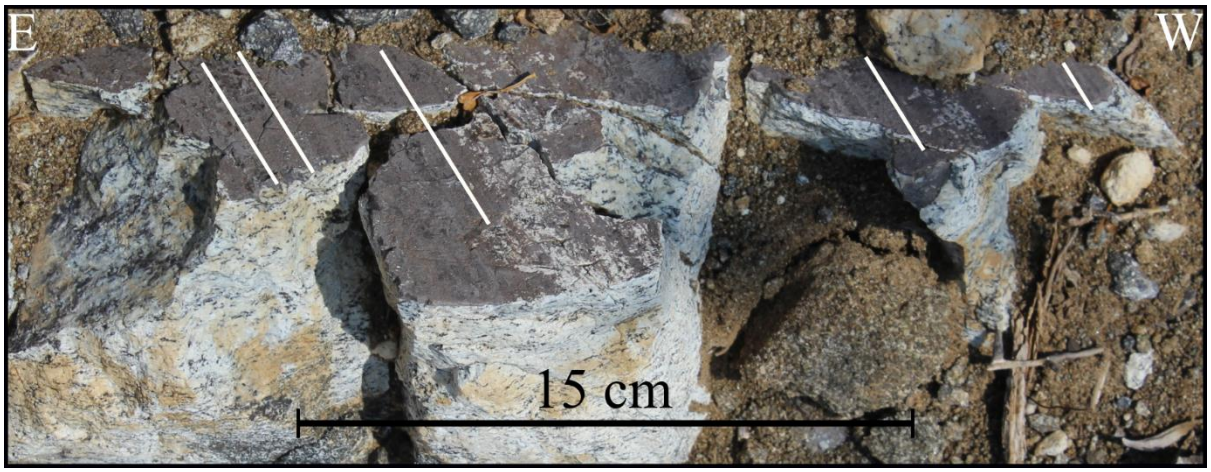


Figure 3.46: Outcrop photograph of slickenlines on the top surface of a pseudotachylite GPPD. Several slickenlines are traced by the solid white lines.

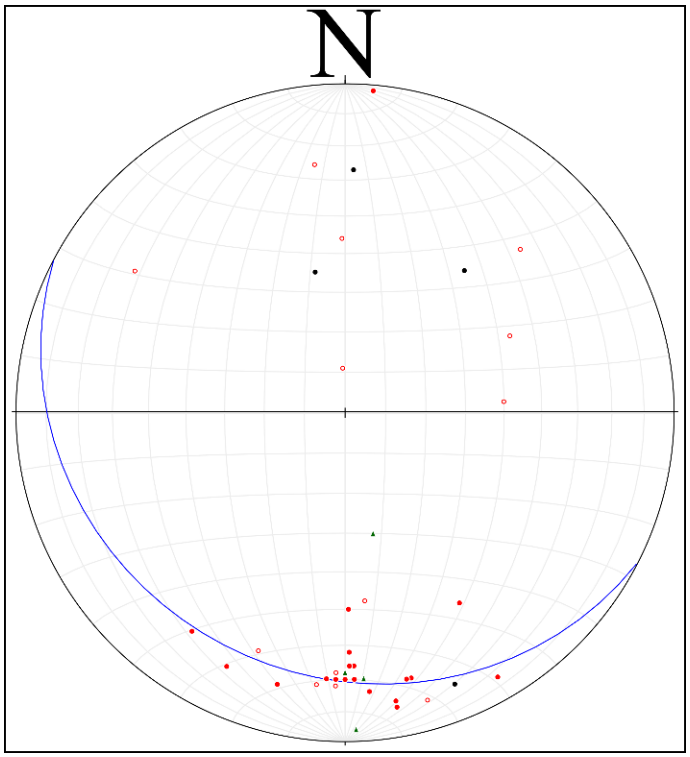


Figure 3.47: Equal area stereoplot of slickenlines within the various lithologies exposed at Jagdlust Farm and surrounding study area. The black dots are slickenlines within the chromitites (n=4). The green triangles are slickenlines within the pyroxenites (n=4). The red dots are slickenlines within the chromite-foliated anorthosite; hollow dots are on fractures without pseudotachylite (n=13), solid red dots are on pseudotachylite-bearing fractures (n=19). The blue line is the average plane to magmatic layering.

By interpreting the observed fault parallel shears and fractures as Y shears (Figure 3.48), numerous observed shear fractures have orientations and kinematics comparable to those of ideal R-R' and P-P" shears (Logan, 1979; Swanson, 1988; Davis et al., 2000); as such, these fractures are used as kinematic indicators. Therefore, as observed R-R' fractures dip north (Figure 3.44, Figure 3.16 and Figure 3.45), and P-P" fractures (Figure 3.32 and Figure 3.45) dip south, a top-to-north displacement sense is inferred for the layer-parallel fault.

Polycrystalline plagioclase clasts and chromite-aggregate fabrics (Figure 3.14, Figure 3.16 and Figure 3.45) within the quasi-ductile cataclasite have a sigmoidal shape. The sigmoidal fabrics and clasts have asymptotic tops to the north and bottoms to the south and dip south suggesting a top-to-north sense of shear (Lister and Snoke, 1984).

Within the hand samples, two trends in tension gashes with pseudotachylite-fill are observed. These trends were N-S to NW-SE and E-W. The E-W trend is interpreted as T_1 to T_2 fractures (Figure 3.48) (Swanson, 1988). The N-S to NW-SE trend accompanied by the E- and W-dipping, normal-sense shear fractures indicate E-W extension that was contemporaneous with the top-to-north displacement observed within the layer-parallel fault (Figure 3.19 and Figure 3.35).

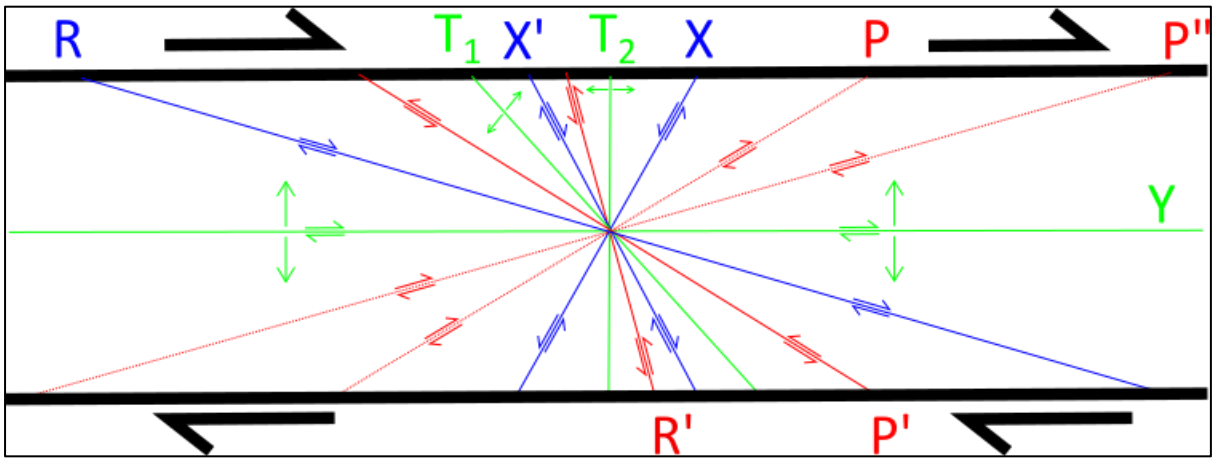


Figure 3.48: Schematic diagram of the expected orientation of fractures forming between two paired GPPDs in a top-to-north fault zone, after Swanson (1988). R, R', P to P" and P' shears should dip at 15° N, 75° N, 20°-15° S and 30° N, respectively, for a top-to-north displacement sense (Logan, 1979; Swanson, 1988; Davis et al., 2000).

4 TIMA analysis and description

Owing to the cryptocrystalline nature of the pseudotachylite and alteration within the fault zone the mineralogy could not be determined using optical microscopy. Initially, electron probe micro-analysis was chosen to determine the composition of the various pseudotachylites as well as the alteration products. Standards for this method, however, could not be compiled as the total oxide percentage for most samples was below 90% despite using multiple different standards. These poor results are likely owing to the dehydration of the alteration products under the electron beam. It was, therefore, decided to use the TIMA as the results are produced by the comparison of the produced EDS spectra to standards of mineral spectra. This method, albeit qualitative, is less sensitive to dehydration as it compares the peak heights of the various elements present (Hrstka et al., 2018).

By comparing the obtained spectra to the mineral spectra within the TIMA database, it was determined that the major minerals present within the host rock and fault rocks are Ca-rich plagioclase (anorthite with minor Mg-enrichment, Figure 4.1), chromite (forming a solid solution of spinels, Figure 4.2) (Liipo et al., 1994) and chlorite (chamosite with minor constituents of clinochlore, Figure 4.3) (Brindley, 1949; Welch, 2004; Wu et al., 2019). The TIMA is able to compile mineral phase maps using this data by assigning the identified minerals to BSE values at the corresponding point of spectral analysis; using the BSE values to map the mineral phases (Hrstka et al., 2018). However, owing to the small differences in BSE values between the plagioclase and the chloritization (Figure 4.4B), the TIMA software did not adequately map the chloritization textures using the phase mapping method (Figure 4.4C).

Furthermore, pseudotachylite could not be adequately distinguished from the wallrock using the phase mapping method. This is likely owing to the fact that pseudotachylite is expected to be compositionally similar to the wallrock (Higgins, 1971; Sibson, 1975; Allen, 1979) as well as small BSE differences between the rock types and fine-grained nature of the pseudotachylite (Figure 4.4).

As the composite elemental maps revealed more textural information for chloritization textures as compared to the phase maps, the composite elemental maps were favoured for the description and analysis of textures and relationships thereof (Figure 4.4D, see 2.2.5 for methodology)

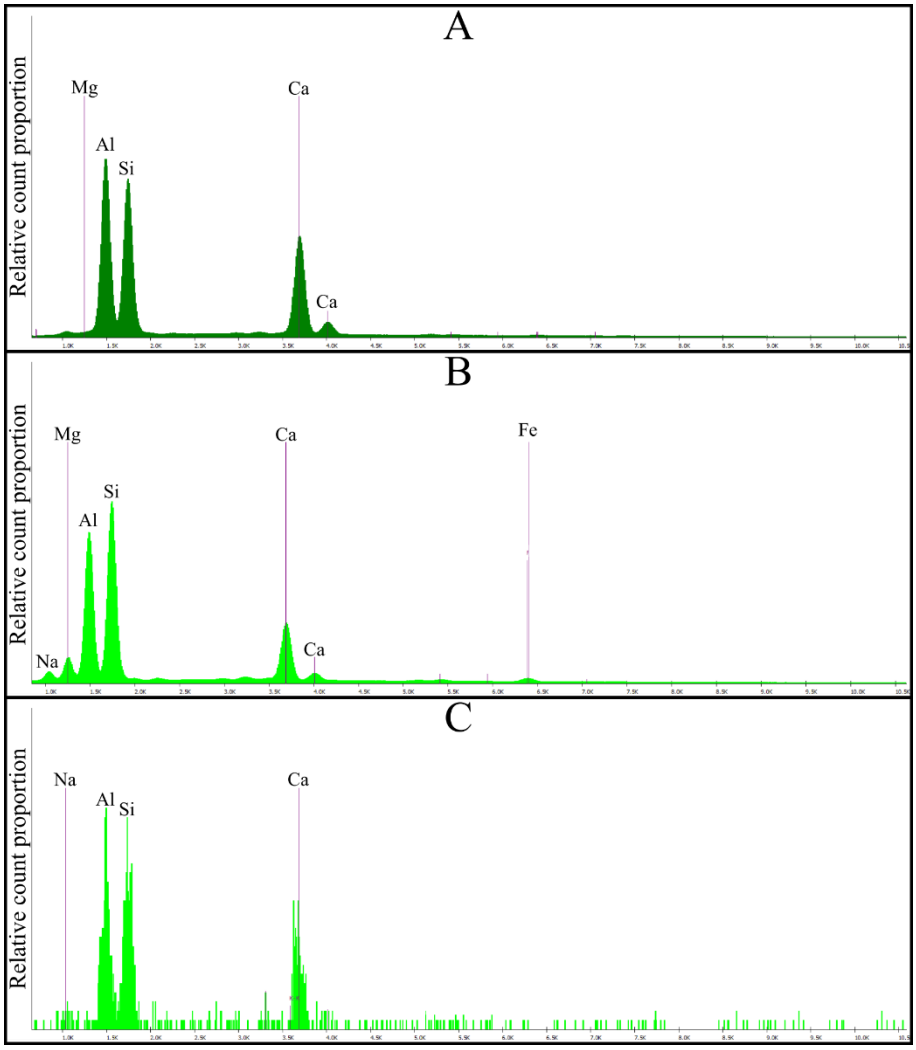


Figure 4.1: Comparison between the EDS spectra for the TIMA anorthite standard (A) and plagioclase from the chromite foliated anorthosite (B) and plagioclase from the pyroxene-foliated anorthosite (C). Plagioclase from the chromite foliated anorthosite has slight enrichment of Mg and minor amounts of Na. A large line spacing for the pyroxene-foliated anorthosite has resulted in the discrete data form of C.

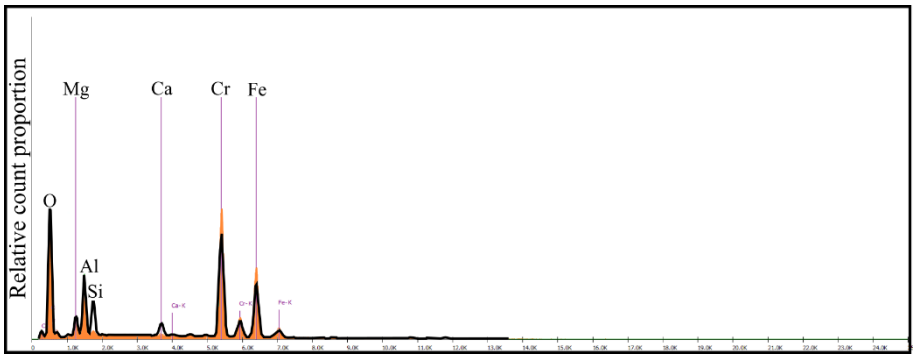


Figure 4.2: Comparison between the EDS spectra for the TIMA xieite standard (chromite polymorph, orange) and chromite within the chromite-foliated anorthosite (black line). Chromite within the anorthosite has slight enrichment of Mg, Al and Si, which form a part of the chromite-spinel solid solution series (Liipo et al., 1994). Ca is also present in minor proportions within chromite in the sample set.

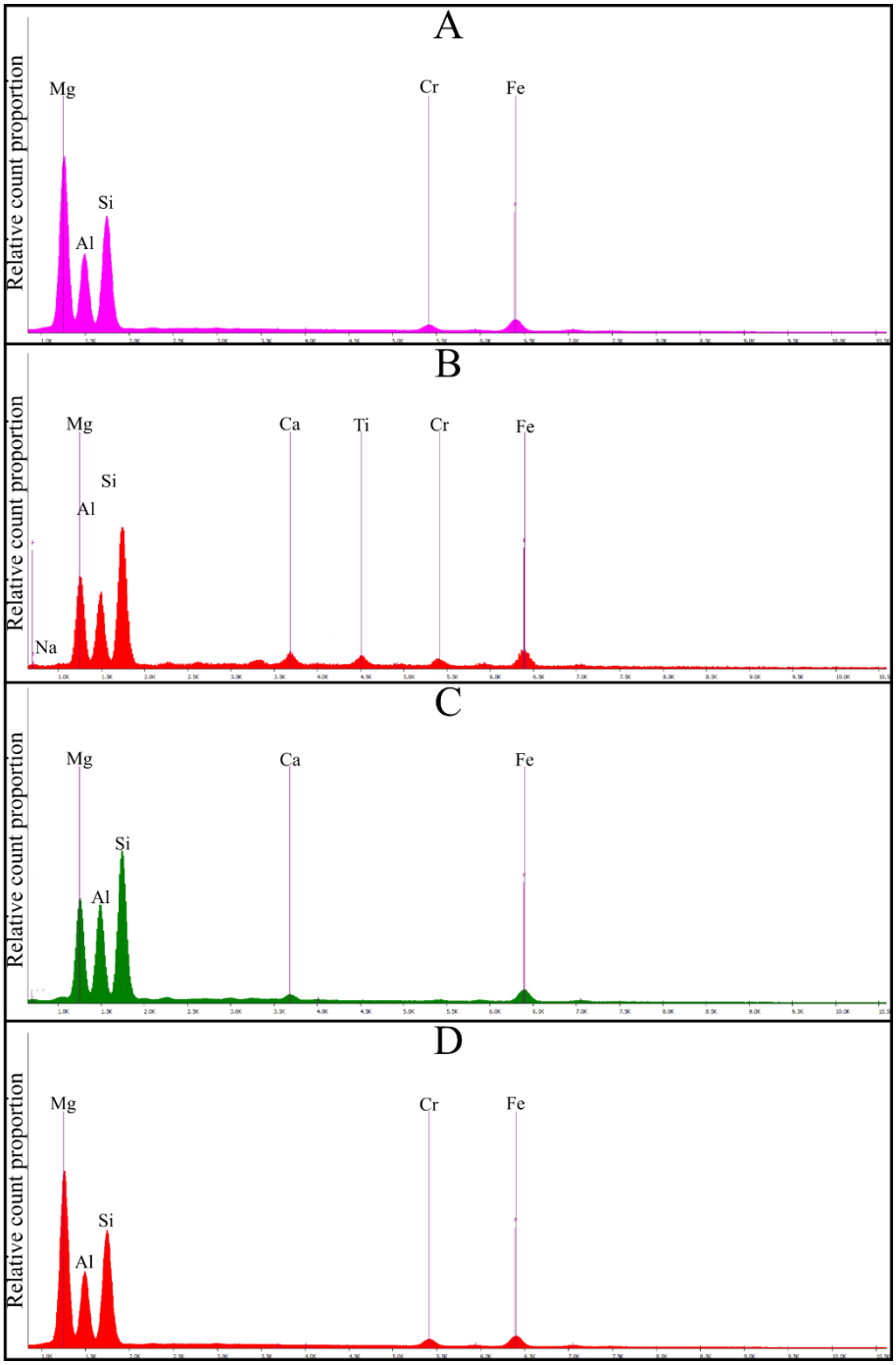


Figure 4.3: Comparison between the energy-dispersive spectroscopy spectra for the TIMA chlorite standard (A) and chlorites of various Mg proportions within the chromite-foliated anorthosite fault (B, C and D). The chlorite is likely chamosite with clinochlore solid solution (Brindley, 1949; Welch, 2004; Wu et al., 2019).

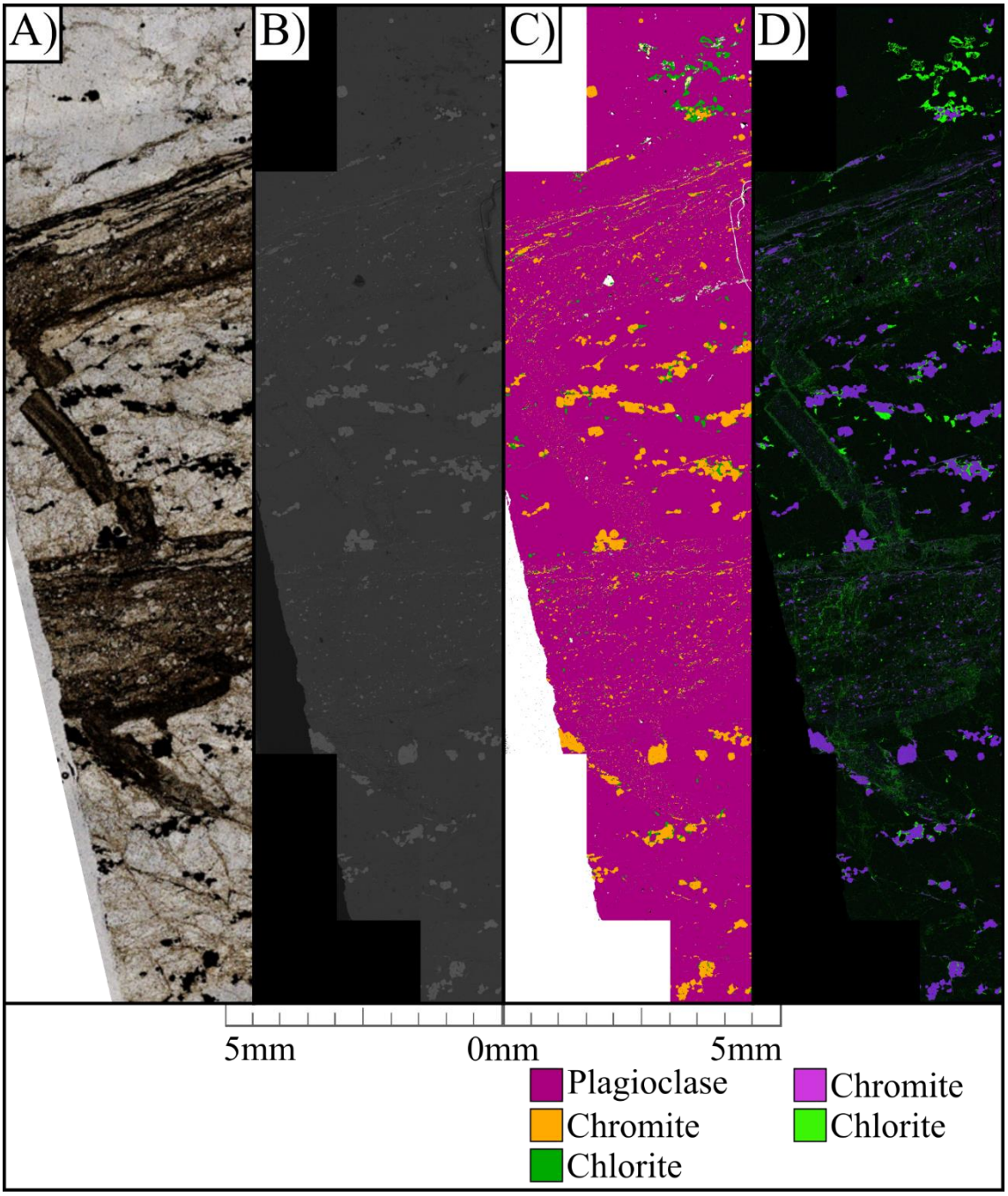


Figure 4.4: An example of the differences in textural and mineralogical detail of pseudotachylite, cataclasite and chloritization as revealed by optical microscopy (A), BSE imaging (B), phase mapping (C) and Fe-Mg-Cr composite elemental mapping (D). The images are of the only scanning area within the MHJL-009 thin section. See section 2.2.5 for (C) and (D) production methodology.

4.1 Alteration mineralogy and textures

Using primarily the Fe-Mg-Cr composite elemental maps, three chloritization textures were described within the chromite-foliated anorthosite fault rocks, viz. blebby-, webbed and fleck-textured chloritization.

The blebby-textured chloritization is observed as luminous green, blebby to bulbous patches within the Fe-Mg-Cr composite maps (Figure 4.4). The blebs are typically along foliation-parallel fractures and spatially associated with magmatic chromite aggregates, grading into webbed-textured chloritization away from the magmatic chromite. Locally, blebby-textured chloritization may occur within fractures devoid of magmatic chromite; this, however, may be a 3D effect. Blebs are up to 0.2×1 mm and may surround several magmatic and comminuted chromite grains (Figure 4.4). The grain size of the chlorite within the blebby-texture is either indistinct using this method or cryptocrystalline.

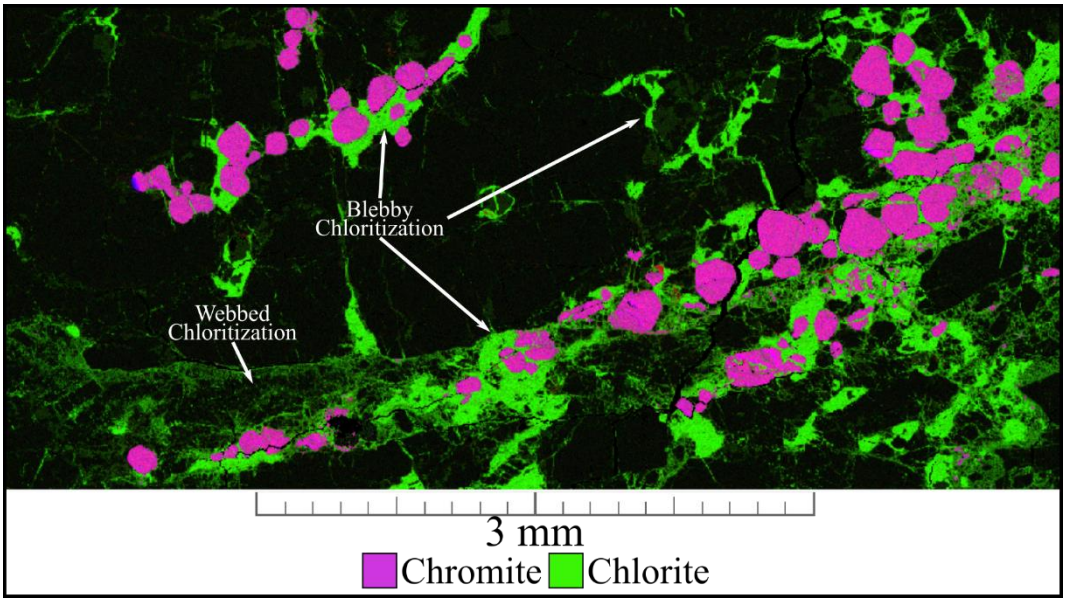


Figure 4.5: A section from the Fe-Mg-Cr elemental composite map of MHJL-001 scanning area A. The image shows the blebby-textured chloritization (bright green) and its association with magmatic chromite aggregates (purple). See section 2.2.5 for image production methodology.

The webbed-textured chloritization is observed as a well-disseminated, luminous green colour (within the Fe-Mg-Cr composite maps) anastomosing in a web-like pattern throughout fractures and comminuted fault rock (Figure 4.6). The webbed-texture grades into the blebby-texture near magmatic chromite aggregates (Figure 4.5), however, near comminuted chromite aggregates, the chloritization has a webbed-texture (Figure 4.6 and Figure 4.7). Grain size is indistinct owing to the gradational nature of the chloritization; spot spacing has produced a pixelated appearance suggesting that grain size is <3 µm.

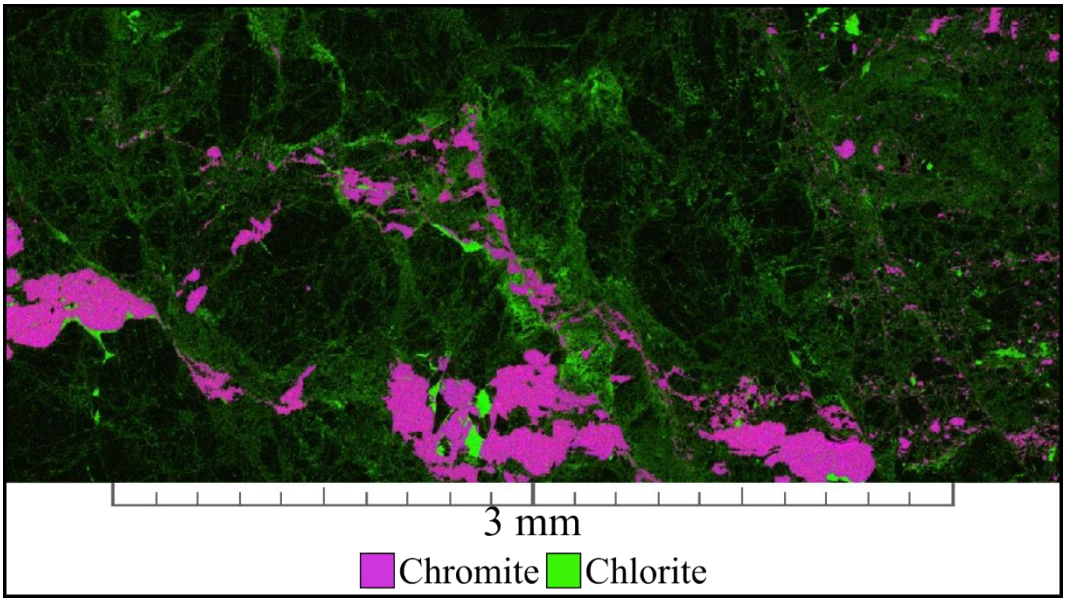


Figure 4.6: A section from the Fe-Mg-Cr elemental composite map of MHJL-003 scanning area A. The image shows the webbed-textured chloritization (bright green). See section 2.2.5 for image production methodology.

Within the Fe-Mg-Cr composite maps, the fleck-textured chloritization appears as luminous green (within the Fe-Mg-Cr composite maps), subangular to angular polygons or flecks (Figure 4.7). The flecks are up to 0.5×10 µm and are disseminated amongst comminuted grains of plagioclase and chromite within cataclasite matrix. There does not appear to be a spatial association of the flecks with magmatic or comminuted chromite grains.

The fleck-texture is interpreted as disaggregation of the blebby-textured chlorite during comminution. This is because the fleck-textured chloritization is observed in both the quasi-ductile cataclasite and is surrounded by pervasive, webbed-textured chloritization as well as being disseminated through cataclasite matrix, in which the webbed-textured chlorite is absent (Figure 4.7, see 4.2.2 Quasi-ductile cataclasite). Therefore, the webbed-textured chloritization is interpreted as the product of fluid flow synchronous with comminution, as the texture grades into the blebby-textured chloritization along fractures, but surrounds the flecked-textured chlorite (Figure 4.8).

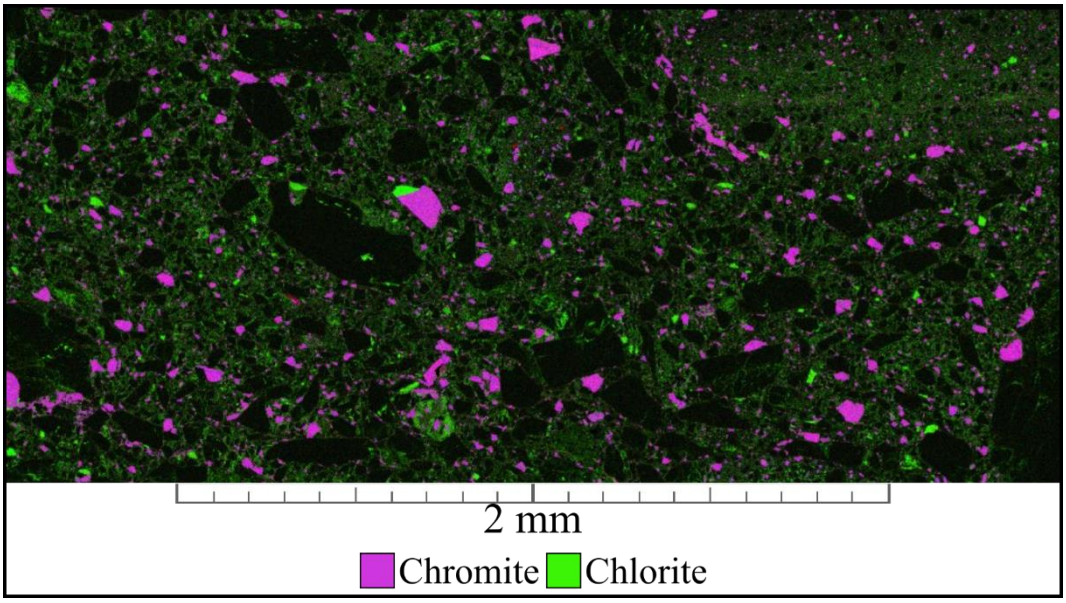


Figure 4.7: A section from the Fe-Mg-Cr elemental composite map of MHJL-003 scanning area C. The image shows the flecked-texture chloritization (bright green). See section 2.2.5 for image production methodology.

4.2 Fault rocks hosted in the chromite-foliated anorthosite

4.2.1 Fractured chromite-foliated anorthosite

The chromite-foliated anorthosite is found as both relatively intact footwall, and as clasts within the cataclasite and breccia (Figure 3.34). Fracture density varies in the footwall, with both foliation-parallel and foliation-oblique fractures being present (see Chapter 3.3.1). The foliation-parallel fractures are typically ≤0.1 mm in width, except near magmatic chromite aggregates where the fractures are up to 1 mm in width and have an anastomosing form (Figure 4.8 and Figure 4.9). Likewise, the foliation-oblique fractures have an anastomosing form up to 1 mm in width, which appears to be controlled by the magmatic plagioclase grain boundaries (Figure 4.9).

Within the fractures, both blebby and webbed-textured chloritization is present. Blebby-textured chlorite typically occurs near the magmatic chromite aggregates but may also occur along relatively thicker foliation-oblique fractures (Figure 4.8). Webbed-textured chloritization occurs along grain boundaries as well as the foliation-parallel and foliation-oblique fractures. This texture may occur adjacent to magmatic chromite aggregates within foliation-parallel fractures, but these fractures truncate the magmatic chromite aggregates (Figure 4.8).

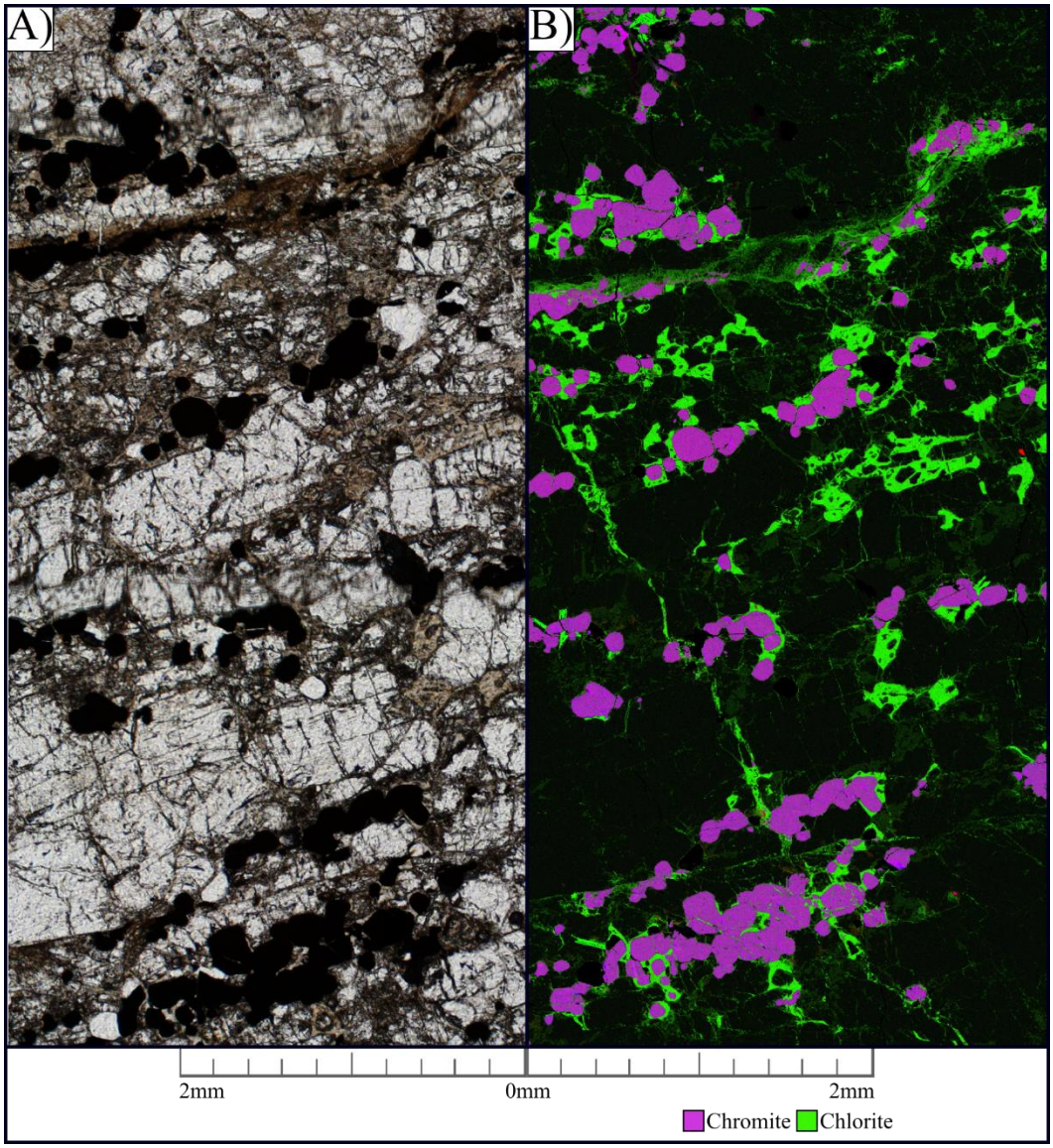


Figure 4.8: Photomicrograph (A) and corresponding Fe-Mg-Cr composite map (B) of the MHJL-001 scanning area A. The composite element map shows the blebby-textured chloritization along foliation-oblique and foliation-parallel fractures. The blebby-textured chloritization typically grades into the webbed-textured chloritization away from magmatic chromite aggregates. The webbed-textured chloritization occurs along grain boundaries and foliation-parallel and foliation-oblique fractures. See section 2.2.5 for image production methodology.

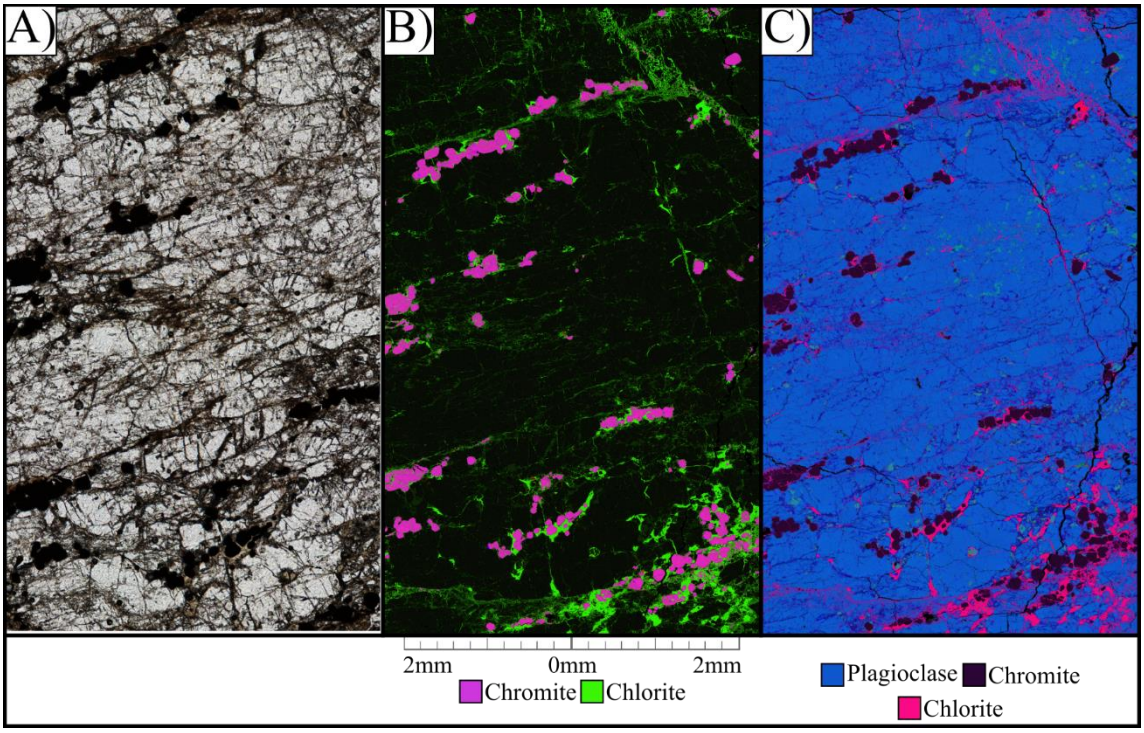


Figure 4.9: A) Photomicrograph of foliation-parallel and foliation-oblique fractures within the chromite-foliated anorthosite and corresponding RGB composite elemental maps of B) Fe-Mg-Cr and C) Mg-Ca-Al. The images emphasize the distribution of chlorite along fractures as well as the relationship between the webbed-textured chlorite, blebby-textured chlorite, and magmatic chromite aggregates. The images are of MHJL-001 scanning area B. See section 2.2.5 for B) and C) production methodology.

4.2.2 Quasi-ductile cataclasite

The quasi-ductile cataclasite consists of subrounded comminuted and altered grains of plagioclase up to 0.2 mm and irregular-shaped chromite, which has a smeared appearance (Figure 4.10). The grain size within the sigmoidal chromite-aggregate fabric is indistinct but is assumed to be comminuted owing to the shape of the aggregates and the surrounding matrix consisting of comminuted plagioclase grains and chlorite. The comminuted chromite aggregates are elongate, up to 0.1×0.4 mm, and are subparallel to each other (Figure 4.10B).

Chloritization is pervasive throughout the quasi-ductile cataclasite, forming a webbed-texture. A few flecks of chlorite are observed within the quasi-ductile cataclasite but are ≤50 μm and subrounded to subangular (Figure 4.10B and C).

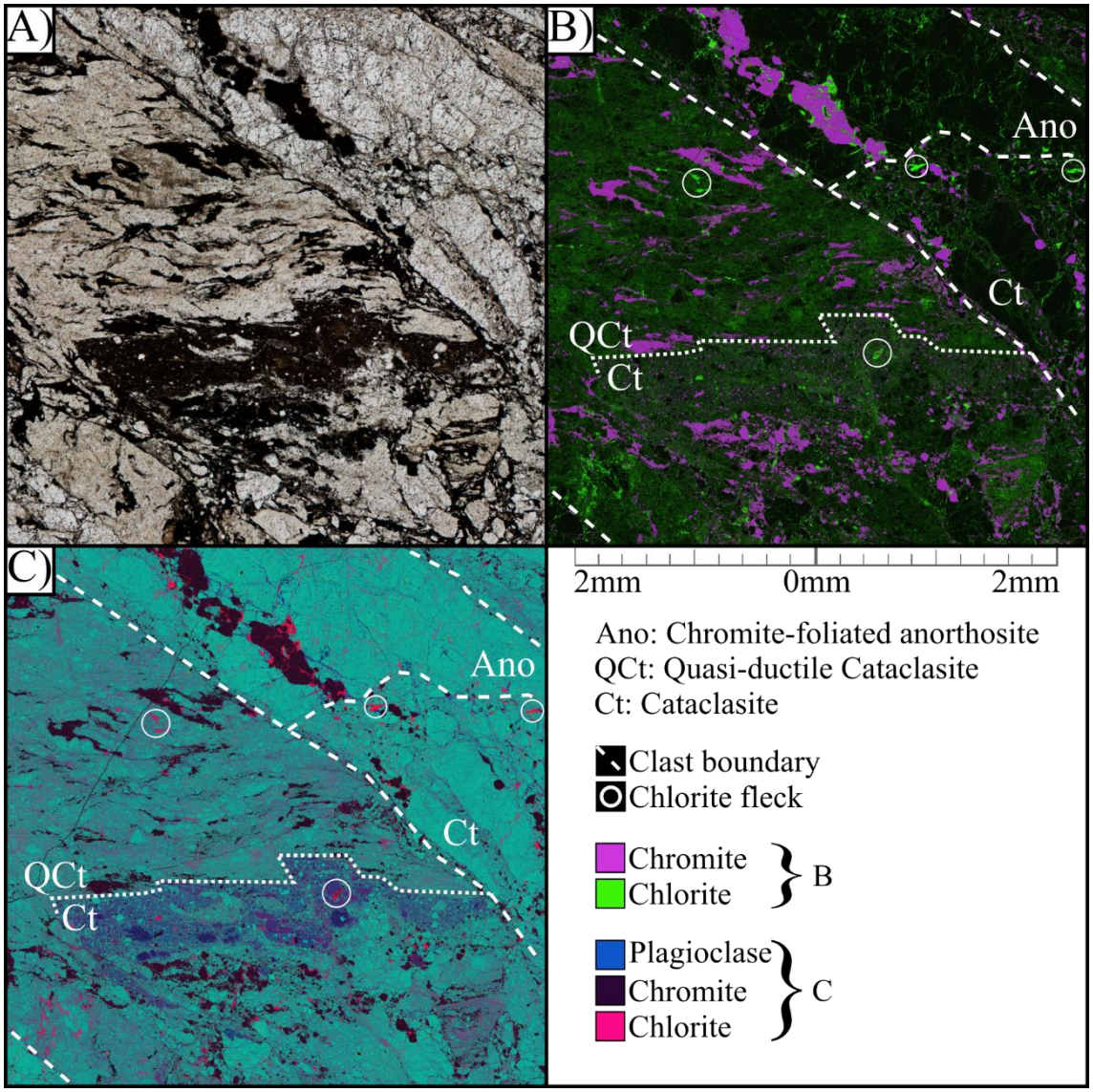


Figure 4.10: Photomicrograph (A), Fe-Mg-Cr composite map (B) and Mg-Ca-Al composite map (C) of MHJL-003 scanning area B. The images emphasize the chloritization textures (B) and clast-shape (C) within the quasi-ductile cataclasite and two generations of cataclasite. The quasi-ductile cataclasite and older cataclasite generation are within a clast of the younger cataclasite. The quasi-ductile cataclasite and older cataclasite generation have pervasive webbed-textured chlorite. The younger cataclasite has flecked-textured chloritization. A chromite-foliated anorthosite clast is also observed. This clast has a blebby-textured chloritization. The disaggregation of the anorthosite clast has produced the flecked texture. See section 2.2.5 for B) and C) production methodology.

4.2.3 Pseudotachylite

Several pseudotachylite dykes were scanned using the TIMA, however, grain sizes within the pseudotachylite dykes are indistinct, indicating an exceptionally fine-grained nature of the fault rock (<3 µm). Clasts within the various dykes are up to 0.2 mm, with the majority consisting of subangular to rounded comminuted chromite (Figure 4.11).

Using optical microscopy, several pseudotachylite generations were observed to display internal colour banding (see Ch3.3.3). Colour banding is the result of internal compositional variation, crosscutting chloritization or, possibly, internal grain size variation.

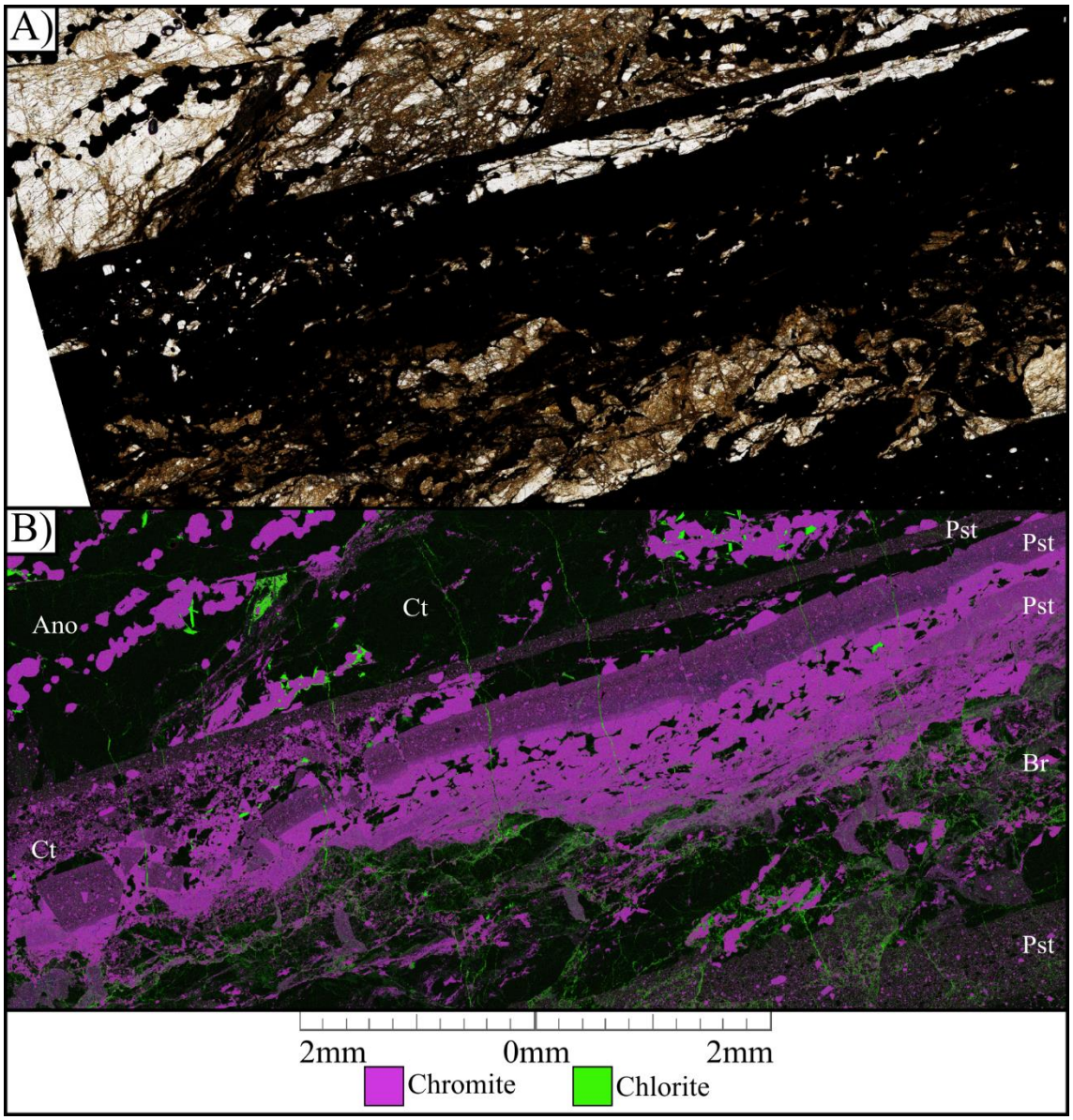


Figure 4.11: Photomicrograph (A) and corresponding Fe-Mg-Cr composite map (B) showing the webbed-textured chloritization crosscutting pseudotachylite GPPDs (Pst) and injection veins within the breccia (Br) consisting of anorthosite (Ano) clasts. The pseudotachylite dykes are fractured to varying degrees with older generations forming clasts within cataclasite (Ct) associated with younger pseudotachylite generations. The more deformed pseudotachylites are crosscut by webbed-textured chloritization. It is unclear if the near-perpendicular fractures are associated with deformation or production of the thin section. The images are of the MHJL-006A thin section scanning area B. See section 2.2.5 for B) production methodology.

The majority of pseudotachylite generations do not show compositional variation. However, chromium-rich pseudotachylite has chromium-enrichment along the edges of the pseudotachylite dykes (Figure 4.11).

Colour banding also appears to be the result of chloritization of the pseudotachylite matrix (Figure 4.4 and Figure 4.12). The chloritization of the matrix is not pervasive but is restricted to the margins of dykes and crosscutting fractures with the centre of the dykes being relatively weakly chloritized by comparison (Figure 4.12). This localization of chloritization could be the result of the chloritization sealing the pseudotachylite to fluids (Manatschal, 1999) or variation in matrix grain size from the margins to the centre of the dykes, which would cause preferential chloritization at the margins.

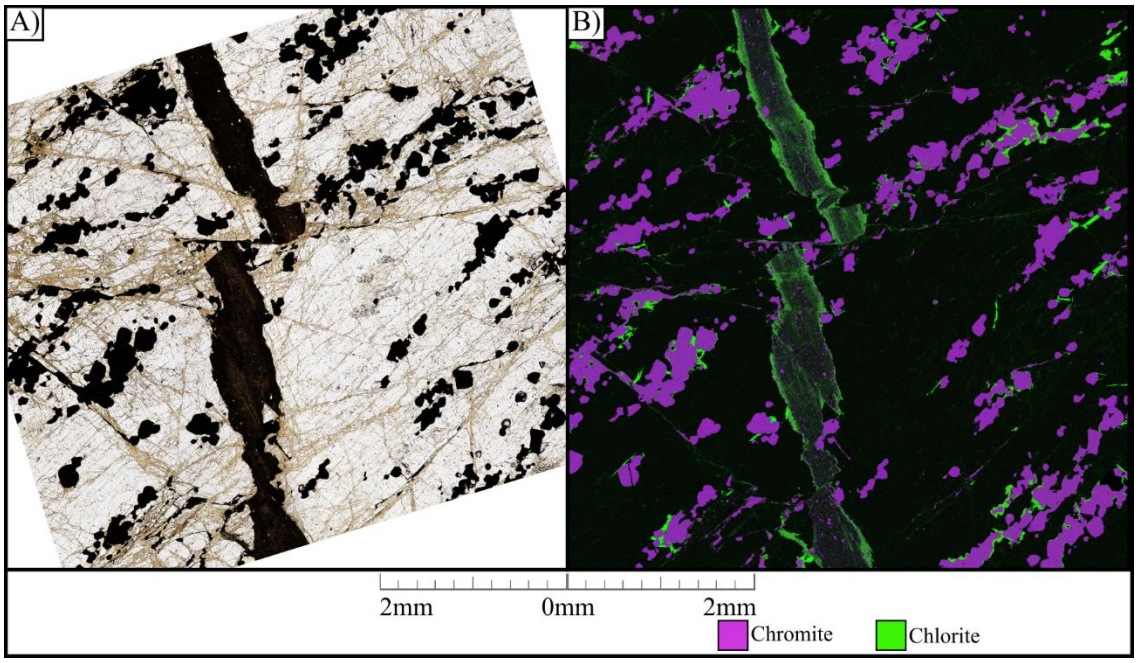


Figure 4.12: Photomicrograph (A) and corresponding Fe-Mg-Cr composite elemental map (B) showing the webbed-textured chloritization along the edges of a pseudotachylite injection vein. The chloritization also weakly pervades the crosscutting fractures, altering the pseudotachylite. The images are of MHJL-006A scanning area A. See section 2.2.5 for B) production methodology.

Colour banding also occurs in pseudotachylite dykes with no clear compositional variation or crosscutting chloritization (Figure 4.13). Banding in these samples is presumably the result of variation in the grain size of the matrix despite remaining cryptocrystalline.

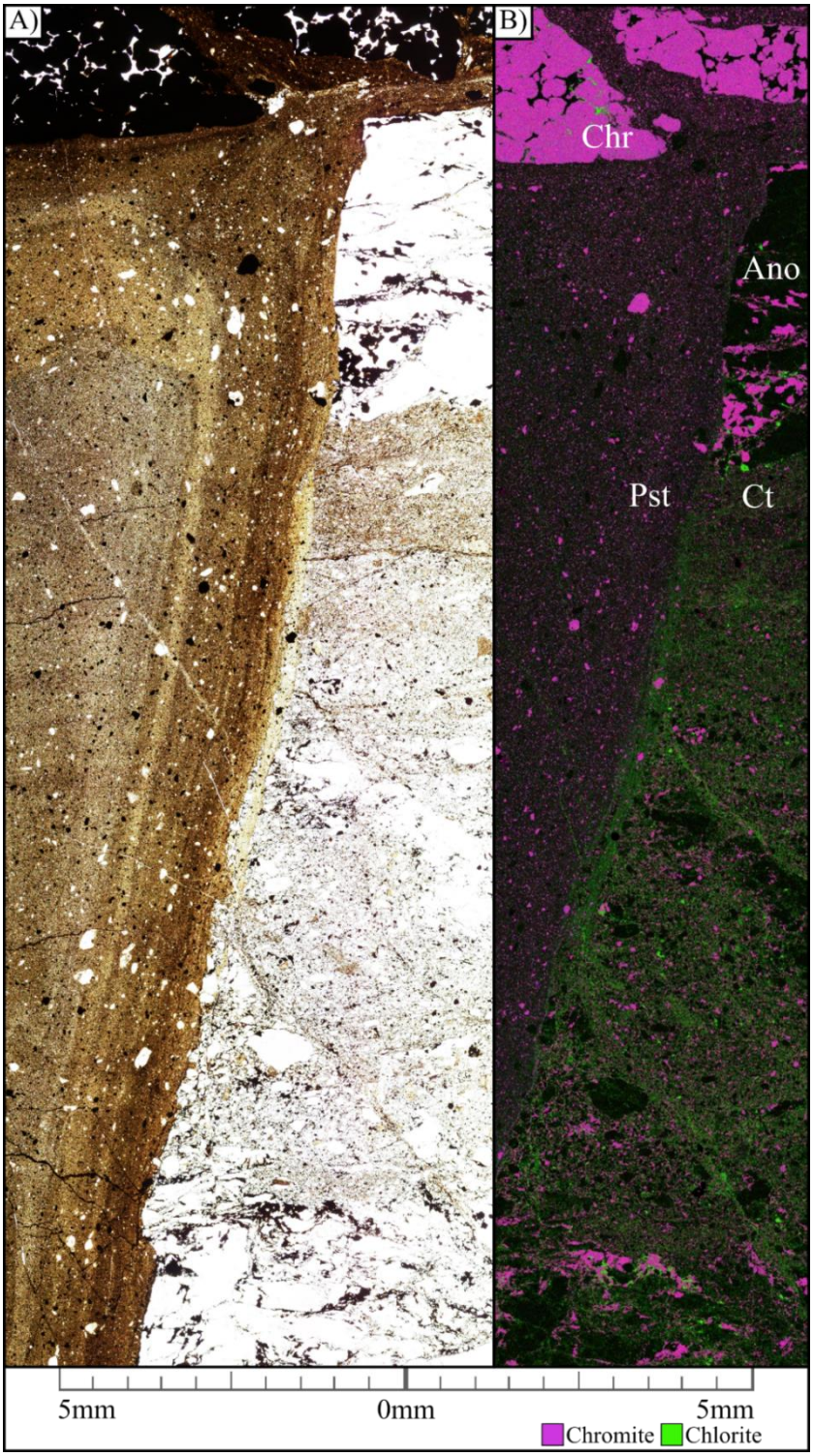


Figure 4.13: High exposure photomicrograph (A) of colour banding within a pseudotachylite (Pst) injection vein and corresponding Fe-Mg-Cr composite map (B). The colour composite map shows that the colour banding is neither the result of crosscutting chloritization nor compositional banding. The banding is presumed to be the result of grain size variation within the matrix. The injection vein crosscuts chromite-foliated anorthosite (Ano), cataclasite (Ct) and a chromitite (Chr) nodule. The images are of the only scanning area within the MHJL-008D thin section. See section 2.2.5 for B) production methodology.

Chloritization that crosscuts pseudotachylite has a webbed-texture but not all pseudotachylite generations are crosscut by alteration (Figure 4.11, Figure 4.12 and Figure 4.13). Deformation associated with the unaltered generations is observed to crosscut the chloritized pseudotachylite (Figure 4.11). Furthermore, fractures, which crosscut pseudotachylite may not be chloritized to the same degree as the pseudotachylite, which they crosscut (Figure 4.12).

4.2.4 Cataclasite and breccia

The matrix of the cataclasites consists of comminuted grains up to 0.2 mm (Figure 4.10, Figure 4.13 and Figure 4.14), which range in shape from rounded (typically smaller at ≤50 µm, Figure 4.10 and Figure 4.13) to angular (Figure 4.10 and Figure 4.14). Clasts within the cataclasites and breccias, into which the cataclasites grade (Figure 4.14), consist of fault rocks and chromite-foliated anorthosite (Figure 4.10 and Figure 4.14). Polymineralic and polycrystalline clasts exhibit all three chloritization textures (Figure 4.10 and Figure 4.14) whereas monomineralic clasts and matrix grains typically do not show internal chloritization (Figure 4.14). Chloritization within the matrix may be webbed-textured, flecked-textured or a combination of the two textures (Figure 4.14), however, the webbed-texture appears to be absent from the final stages of slip as the matrix, which surrounds clasts of the various fault rocks has only the flecked-texture (Figure 4.10 and Figure 4.14).

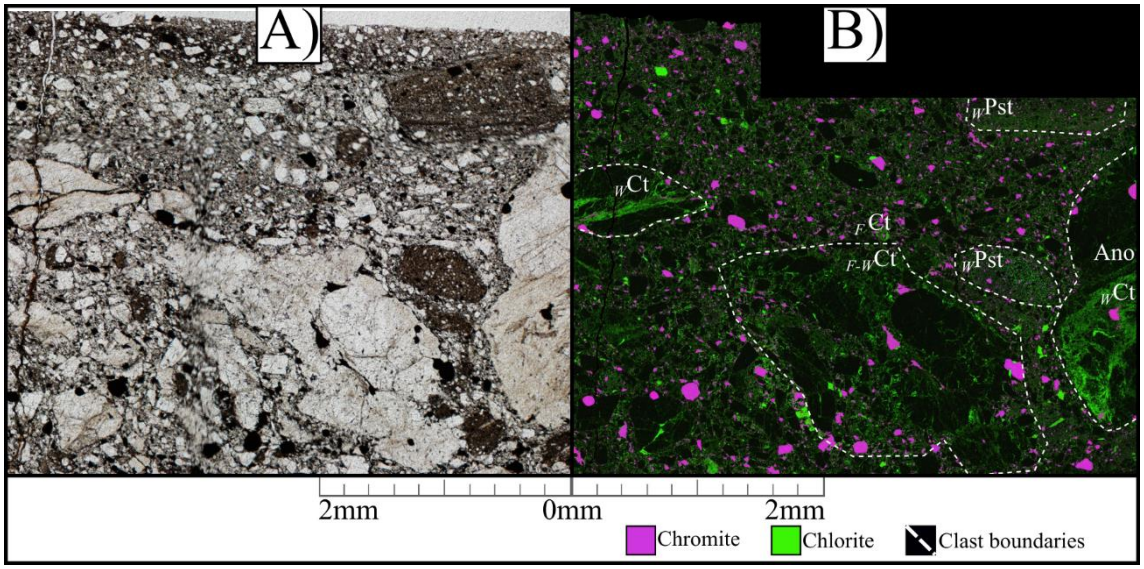


Figure 4.14: Photomicrograph (A) and corresponding Fe-Mg-Cr composite elemental map (B) showing the webbed-textured (subscript W) and flecked-textured (subscript F) chloritization within clasts of cataclasite (Ct), anorthosite (Ano) and pseudotachylite (Pst) within a cataclasite matrix. The images are of MHJL-003 scanning area C. See section 2.2.5 for B) production methodology.

5 Discussion

5.1 The presence of pseudotachylite

Evidence for determining the presence of pseudotachylite can be categorized into two classes. The first class is evidence for conditions, both morphological and mineralogical, that would facilitate the generation of friction melt phase. The second class of evidence includes proxies for and indicators of the presence of a friction melt phase.

5.1.1 Prerequisite processes

For friction melting to occur, frictional contact must be maintained along a fault surface during seismic slip (Sibson, 1975; Bjørnerud and Magloughlin, 2004). This, however, is a self-limiting process in that any melt produced will immediately lubricate the surface removing the frictional contact resulting in the production of low melt volumes (Bjørnerud and Magloughlin, 2004; Sibson and Toy, 2006). Slip along discrete fault planes is expected to produce very little melt as the frictional contact would be lost at the onset of melting. If, however, comminution precedes the seismic slip, the surface area of the fault is increased, allowing for frictional sliding to be maintained as the melt is produced (Allen, 1979; Magloughlin and Spray, 1992). Furthermore, the reduction of grain size by comminution through the prevention of heat loss into the wallrock through conduction, facilitates the melting of the fault rock, particularly the fine-grained material (Allen, 1979; Spray, 1995; Lin and Shimamoto, 1998; Bjørnerud and Magloughlin, 2004). As such, the comminution that produced the quasi-ductile cataclasite provided a favourable environment for the generation of a friction melt.

Pseudotachylite is a product of friction melting during high slip-rate events as it is only during these events that sufficient heat can be produced for the melting of the mineral phases present at the fault surface interface (Sibson, 1975; Allen, 1979; Magloughlin and Spray, 1992; Bjørnerud and Magloughlin, 2004). Considering that hydrous mineral phases act as a flux, reducing the melting temperatures of the mineral phases; hydrous phases are an important precursor to the generation of friction melts (Sibson, 1975; Allen, 1979; Sibson and Toy, 2006; Bjørnerud, 2010). The precursor of hydrous phases could be considered particularly important for the generation of pseudotachylite within the Bushveld Complex where the mafic-to-ultramafic minerals have solidus temperatures >1000°C (Keith, 1954; Drake, 1976; Passchier and Trouw, 2005; Rowe and Griffith, 2015). As such, the presence of epidote and chlorite within the quasi-ductile cataclasite and anorthosite wallrocks further supports the notion that the conditions were favourable for friction melt generation during slip events as these minerals would act as a flux for the anhydrous, mafic phases.

The presence of pseudotachylite is taken to be an indicator of coseismic slip (Sibson, 1975; Sibson, 1977). This is because at seismic slip-velocity the rate of frictional heat production exceeds the rate of heat dissipation within the fault, resulting in friction melting of the fault rocks (Sibson, 1975; Sibson, 1977; Bjørnerud and Magloughlin, 2004; Rowe and Griffith, 2015). However, heat generation is only the predominant mechanism amongst others for the dissipation of the stored elastic strain released during faulting (Sibson, 1977; Pittarello et al., 2008; Faulkner et al., 2010; Faber et al., 2014; Rowe and Griffith, 2015). As such, it is possible to infer coseismic slip by identifying other coseismic features. Rowe et al. (2012) showed that the width-to-length ratios of injection veins, irrespective of whether the fracture fill was fluidized gouge or pseudotachylite, could not be accounted for by non-seismic failure and pressure gradients. Therefore, the presence of pseudotachylite injection veins within the Jagdlust Farm fault system is indicative that slip was coseismic; favouring the hypothesis that a friction melt was generated when accompanied with the evidence of other prerequisite conditions being satisfied.

5.1.2 Friction melt indicators

Although it is important to show that the fault conditions where favourable to the generation of friction melt, it only shows that it was possible to produce such a melt. As such, evidence for melt indicators and proxies must be presented. Such indicators and proxies include; flow banding, the absence of a log-normal grain distribution, and comparative compositions between melt and wallrocks (Higgins, 1971; Sibson, 1975; Spray, 1995; Lin and Shimamoto, 1998; Di Toro and Pennacchioni, 2004; Price et al., 2012; Rowe and Griffith, 2015).

As mentioned previously, frictional contact must be maintained on the fault surface to produce friction melts (Sibson, 1975; Bjørnerud and Magloughlin, 2004). Another process that facilitates frictional sliding during friction melting is the flow of melt into dilatational sites (Sibson, 1975; Bjørnerud and Magloughlin, 2004). Flow in the fault system at Jagdlust Farm is evidenced by flow banding in cryptocrystalline discordant fractures with differing compositions to the immediate host rock. Several samples were noted to have banding in a cryptocrystalline matrix that traces the edges of both discordant and concordant fractures. In particular, the MHJL-008D thin section (see Figure 4.13) shows banding within the cryptocrystalline matrix that is not related to compositional variation under SEM, suggesting that banding is related to flow rather than alteration, as seen in MHJL-006A (see Figure 4.12). Rowe et al. (2012) showed that injection vein aspect ratios were similar, irrespective of whether the fracture fill had undergone melting or fluidization. However, it is reasonable to conclude that the injection vein matrix underwent a melt phase as the fluids present within the fault system are seen to produce a chloritic alteration assemblage within comminuted material through which they flowed, yet chloritization is comparatively absent

within the injection vein observed in MHJL-008D (see Figure 4.13) and only occurs along vein boundaries and crosscutting fractures in MHJL-006A (see Figure 4.12). Furthermore, the compositional contrast between the MHJL-008D injection vein and wallrock (see Figure 4.13) indicates that melt was produced along a frictional surface, to which the melt should be relatively similar compositionally, and flowed into a dilatational site to which the host composition is dissimilar (Sibson, 1975; Bjørnerud and Magloughlin, 2004; Bjørnerud, 2010).

During cataclasis, a power-law grain-size distribution is produced (Evans, 1988; Ray, 2004; Lin, 2008; Pittarello et al., 2008). As such, several authors have shown that the grain-size distribution within concordant and discordant veins deviates from this distribution, concluding that the deviation is a result of the smallest grains being incorporated into a melt phase (Spray, 1995; Ray, 2004; Lin, 2008; Pittarello et al., 2008). This is owing to the finer-grained clasts absorbing more heat per unit mass, resulting in preferential melting of the smaller grains (Sibson, 1975; Ray, 2004; Lin, 2008). Although a quantitative grain size analysis was not conducted during this study, it was noted that, in most cases, chromite grains within concordant and discordant veins are not only more abundant but are smaller than mono- and polycrystalline plagioclase grains. This supports the notion that a friction melt phase was generated, as smaller clasts consisting of less refractory minerals are expected to be less abundant owing to the preferential incorporation of these clasts into the melt phase (Lin, 1994b; Fabbri et al., 2000); chromite is more refractory than plagioclase solidus temperatures of 2265°C (Keith, 1954; Irvine, 2015) and 1095-1400°C (Drake, 1976), respectively; therefore, a greater abundance of smaller chromite clasts are expected in melt rocks produced in the study area.

5.1.3 Limiting factors

Pseudotachylite-cogenetic incohesive fault rocks

Although the importance of preseismic comminution is well-established (Allen, 1979; Magloughlin, 1989; Spray, 1995; Bjørnerud, 2010), the general perception, historically, is that fault rocks had to be cohesive for the generation of friction melt (Bjørnerud, 2010; Rowe and Griffith, 2015). However, with an increase in attention given to seismic slip and improved methodology in recognising pseudotachylite in field and laboratory studies, evidence for cogenetic pseudotachylite-cataclasite, amongst other incohesive fault rocks, has mounted, invalidating this perception (Fabbri et al., 2000; Di Toro and Pennacchioni, 2004; Bjørnerud, 2010; Bestmann et al., 2012; Rowe et al., 2012; Rowe and Griffith, 2015). Several samples from the Jagdlust Farm fault system displayed tortuous, comingled or diffusive pseudotachylite-cataclasite contact forms, and thus indicate that cataclasite was incohesive during seismic-slip events and cogenetic to the generated friction melt, adding to the

body of evidence for pseudotachylite-cogenetic incohesive fault rocks (Fabbri et al., 2000; Bjørnerud, 2010; Bestmann et al., 2012; Rowe and Griffith, 2015).

Bjørnerud (2010) noted that where pseudotachylite and cataclasite were cogenetic, the fault zone had highly fractured but cohesive and incohesive fault walls and that cataclasite formed a part of the incohesive fault-wall and pseudotachylite was generated at the cohesive-incohesive fault-wall interface. This fault morphology is observed within the chromite-foliated anorthosite fault; the hangingwall is typically cohesive and relatively undeformed, whereas the footwall typically has a pseudotachylite-cogenetic cataclasite-breccia-anorthosite gradation.

This morphology can be accounted for by asymmetric stress distribution across the fault plane (Rowe and Griffith, 2015) and facilitates the generation of pseudotachylite through localizing slip while simultaneously increasing the surface area within the fault (Figure 5.1) (Sibson, 1975; Sibson, 1977; Allen, 1979; Sibson and Toy, 2006; Bjørnerud, 2010). The cohesive hangingwall acts as a rigid surface, providing a stark competency contrast at the footwall-hangingwall interface, localising the majority of the slip (Magloughlin, 1989; Ord and Hobbs, 2013; Crider, 2015). The footwall, by comparison, undergoes delocalised slip as cataclasite flow; the amount of slip decreases away from the footwall-hangingwall interface (Bjørnerud, 2010; Rowe and Griffith, 2015). Delocalization of slip in the footwall is compensated for by the increased surface area produced during comminution, facilitating the generation of a friction melt (Sibson, 1977; Allen, 1979; Bjørnerud, 2010). The cataclasite that remains unmelted and incohesive during the coseismic production, prepares the fault for friction melt production during the next seismic cycle, provided the primary faulting mechanism remains stick-slip and does not revert to cataclastic-flow owing to the incohesive fault rock (Macaudière and Brown, 1982; Magloughlin, 1989; Bjørnerud, 2010). It is at this point that the circulation of hydrothermal fluids becomes important for the resetting of the seismic cycle (Manatschal, 1999; Bjørnerud, 2010; Caine et al., 2010; Speckbacher et al., 2013).

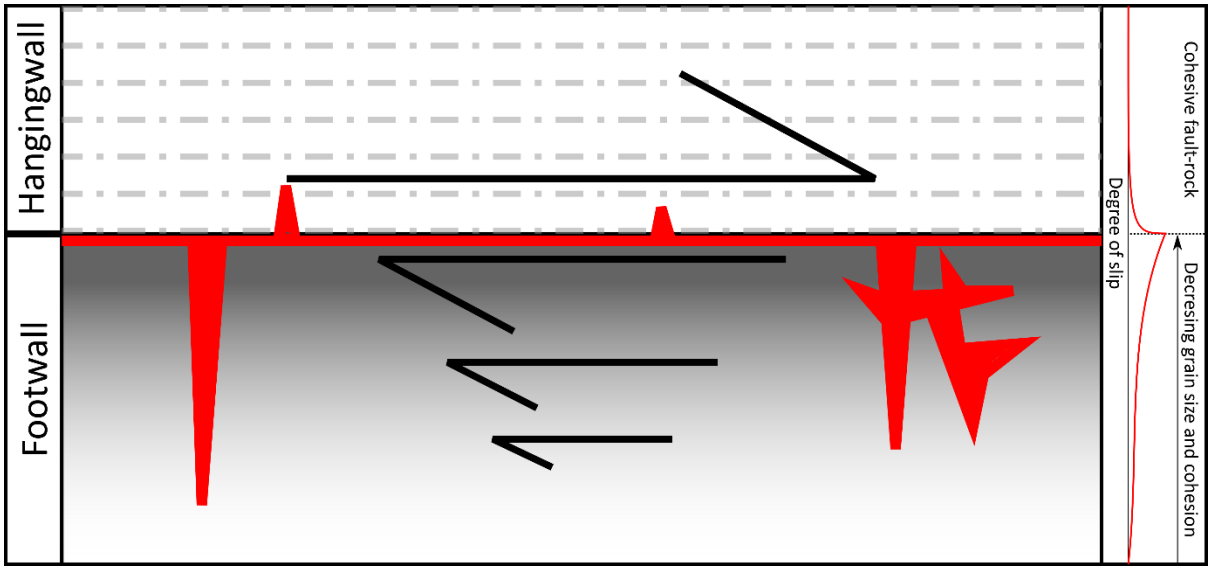


Figure 5.1: Diagrammatic representation of the chromite-foliated anorthosite fault of the Jagdlust Farm fault system. The hangingwall is cohesive fault rock with slip occurring at the footwall-hangingwall interface. The footwall colour gradation represents clast-size distribution within the footwall, with the smallest clasts at the pseudotachylite GPPD (red). Slip within the footwall is distributed through the incohesive fault rock and decreases away from the footwall-hangingwall interface.

Fluid presence

The mutually crosscutting relationship between pseudotachylite and chlorite-bearing fractures within the chromite-foliated anorthosite indicates that fluids were circulating during the inter-seismic periods of the seismic cycle (Sibson et al., 1988). Previously, this would be thought to pose a problem for the generation of pseudotachylite, which requires low pore fluid pressures so that the rock can accommodate sufficient strain for seismic slip (Allen, 1979; Spray, 1995; Sibson and Toy, 2006). However, there is a growing body of evidence showing that the circulation of fluids during the seismic cycle is important in the generation of multiple pseudotachylites within a seismically active fault zone (Smith et al., 2008; Bjørnerud, 2010; Caine et al., 2010; Bestmann et al., 2016). This is because fluids react with the rock producing the hydrous phases with lower melting temperatures preferable for pseudotachylite generation, replacing the phases consumed in the previous pseudotachylite generation (Sibson, 1977; Allen, 1979; Bjørnerud, 2010). Furthermore, as the fluids react with the rock, the alteration products, observed as webbed-textured chlorite here, seal the fault, allowing for the fault to dry (Manatschal, 1999; Bjørnerud, 2010; Caine et al., 2010). The sealing of the fault results in a change of faulting mechanism, which allows for strain build-up and resetting of the seismic cycle (Manatschal, 1999; Bjørnerud, 2010; Caine et al., 2010; Speckbacher et al., 2013). Therefore, the circulation of fluids during the seismic cycle of the Jagdlust Farm fault system would not prevent the formation of pseudotachylite but rather

would have facilitated the production of multiple generations through preventing the coseismic, incohesive cataclasite reverting the primary faulting mechanism to cataclasite-flow.

5.2 Fault zone P-T conditions

The presence of pseudotachylite is often taken to represent the brittle-ductile (B-D) transition within the crust (Sibson, 1975; Sibson, 1977; Sibson, 1990; Spray, 1995; Rowe and Griffith, 2015). This is owing to the coincidence of the seismogenic zone with the B-D transition (Sibson, 1975; Sibson, 1977; Sibson and Toy, 2006; Rowe and Griffith, 2015). Although conditions for the formation of pseudotachylite are favourable at the B-D transition, pseudotachylite is known to form at shallower and deeper crustal levels as the formation has a greater dependence on the slip-rate, amongst other factors, than the P-T conditions (Sibson, 1975; Allen, 1979; Spray, 1995; Bjørnerud and Magloughlin, 2004; Rowe and Griffith, 2015). As such the presence of pseudotachylite cannot be used to conclude a B-D transition regime.

As the formation of pseudotachylite is not restricted to the B-D transition, consideration must, therefore, be given to the depth of the fault as well as to the composition of the host rock as, under a normal geotherm, quartzo-feldspathic rocks have a B-D transition estimated at 10-15 km (Sibson, 1977). This is in contrast to the RLS where pressures equivalent to these depths were only attained at the base of the intrusion (Figure 5.2) (Nel, 1984; Buick et al., 2000; Mavimbela, 2013). Furthermore, the RLS has an ultramafic-mafic composition (Cawthorn and Walraven, 1998; Clarke et al., 2005; Cawthorn, 2015) with the chromite-foliated anorthosite being devoid of quartz and near monomineralic.

As the chromite-foliated anorthosite fault has a predominantly anorthositic composition, 500°C is the minimum temperature, irrespective of pressure, at which crystal-plastic deformation occurs and below which fluid-assisted cataclastic-flow becomes the primary slip mechanism (Tullis and Yund, 1987; Tullis, 1990; Hadizadeh and Tullis, 1992). The quasi-ductile cataclasite samples from the Jagdlust Farm fault system have a ductile appearance in hand sample but shows brittle failure in thin section through comminuted natured of the chromite aggregates defining the sigmoidal fabrics and angular clasts at the edges of the quasi-ductile cataclasite (Sibson, 1977; House and Gray, 1982; Passchier and Trouw, 2005). This indicates that the fault system underwent brittle failure as cataclastic-flow despite a temperature regime that likely exceeded that of the greenschist facies (Sibson, 1977; Hadizadeh and Tullis, 1992; Sibson, 1995; Fusseis and Handy, 2008).

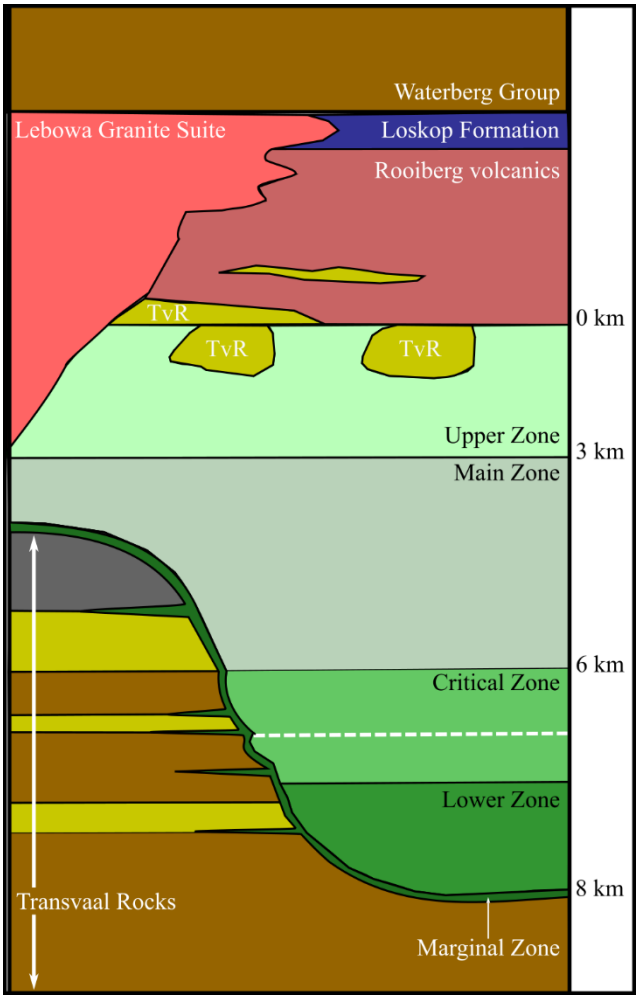


Figure 5.2: Simplified stratigraphy of the Bushveld Complex and the relationship thereof with the Transvaal Supergroup, Rooiberg Volcanics, Loskop Formation and Waterberg Group rocks, after von Gruenewaldt et al. (1985). The Bushveld Complex is estimated to be 8 km thick with an unknown amount of overburden at the time of emplacement. The dashed white line is the approximate stratigraphic level of the chromite-foliated anorthosite fault. Garnet geobarometry estimates greenschist facies pressures of 3-5 kbar at the base of the intrusion (Nel, 1984; Buick et al., 2000; Mavimbela, 2013).

A cataclastic-flow regime also adequately explains deformation twins, the apparent subgrain rotation and banding observed within the mylonitic samples while maintaining brittle failure mechanisms on the microscopic scale. Deformation twinning develops at temperatures <400°C as an initial strain response, before the onset of fracturing (Passchier and Trouw, 2005). Subgrain rotation is a crystal-plastic strain response occuring in plagioclase at temperatures >500°C (Tullis and Yund, 1987; Passchier and Trouw, 2005), however Tullis and Yund (1987) noted extinction patterns that developed in plagioclase while undergoing cataclastic-flow were similar to the subgrain rotation patterns observed in plagioclase having undergone ductile deformation. In the aforementioned study, these authors noted that the cataclastic-flow extinction patterns were patchy, irregular and lacking definitive boundaries rather than discrete grains with sweeping extinction patterns associated with subgrain rotation formed

by dislocation creep. Therefore, the apparent subgrain rotation observed in clasts of the quasi-ductile cataclasite (Figure 3.17) is not indicative of temperatures >500°C.

Banding within the quasi-ductile cataclasite can be produced by cataclastic-flow at temperatures between 300°C and 500°C through the development of anastomosing comminution zones, which reduce grain sizes to <0.1 μm (Tullis and Yund, 1987; Hadizadeh and Tullis, 1992). It is possible within these zones to produce undulatory extinction with comminution, frictional sliding and rotation of the clasts, which mimics the textures seen in crystal-plastic deformation products (House and Gray, 1982; Tullis, 1990).

Although the presence of pseudotachylite is not indicative of the B-D transition regime (Maddock et al., 1987; Bestmann et al., 2012; White, 2012), it does show a change in the primary faulting mechanism from continuous sliding, as cataclastic-flow, to stick-slip failure (Sibson, 1975; Macaudière and Brown, 1982; Spray, 1995). This change in faulting mechanism could be attributed to an increased strain-rate, decreased fluid pressure or a decrease in the ambient fault temperature (Sibson, 1975; Sibson, 1977; Sibson, 1985, 1990; Tullis, 1990; Hadizadeh and Tullis, 1992; Morley and Guerin, 1996; Passchier and Trouw, 2005; Sibson and Toy, 2006). A decrease in ambient fault temperature to below 300°C is favoured as the primary cause for the faulting mechanism transition from cataclastic-flow to stick-slip (Tullis, 1990; Hadizadeh and Tullis, 1992). This transition was possibly assisted by a decrease in fluid-pressure (Tullis, 1990; Hadizadeh and Tullis, 1992; Morley and Guerin, 1996) as late-stage cataclasite and fractures have little-to-no webbed-textured chloritization, suggesting that fluid flow within the chromite-foliated anorthosite fault ceased. However, this only occurred after the faulting mechanism transitioned from cataclastic-flow to stick-slip.

An increase in strain-rate as the cause for the transition from cataclastic-flow to stick-slip faulting is rejected, as cataclastic-flow is a continuous response to applied strain (Tullis, 1990; Hadizadeh and Tullis, 1992). Therefore, an increase in strain-rate would be expected to increase the slip-rate of cataclastic-flow and thickening of the fault rather than cause a transition from cataclastic-flow to stick-slip faulting (Sibson, 1977).

Although the chromite-foliated anorthosite fault records a temperature decrease to that equivalent of greenschist temperatures, <300°C (Sibson, 1975; Tullis, 1990; Hadizadeh and Tullis, 1992), the burial depth is of the fault would not have been sufficient for greenschist facies metamorphism (Sibson, 1977). This would indicate, firstly, that the fault formed outside the seismogenic zone and, secondly, the ambient fault temperature is the result of an abnormal geotherm; suggesting an external heat source (Sibson, 1975; Sibson, 1977; Rowe and Griffith, 2015; Fossen and Cavalcante, 2017).

5.3 Structures and kinematics

Jagdlust Farm has two faults exposed in outcrop. The stratigraphically-lower fault is the S-dipping reverse fault, which crosscuts the LG-6 chromitite (referred to as the LG-6 reverse fault hereafter). S-plunging slickenlines on fault-parallel shear fractures within the fault indicate a top-to-north displacement of the LG-6 chromitite. The fault is highly altered, and a single pseudotachylite injection vein extending horizontally into the footwall was observed.

The stratigraphically-higher fault is the chromite-foliated anorthosite fault, exposed near the lower-upper Critical Zone boundary. This fault is parallel to the magmatic layering. This fault has N- and S-plunging slickenlines on fault-parallel shear fractures as well as spatially-associated R-, R'-, P-, P'-fracture orientations (Logan, 1979; Swanson, 1988; Logan et al., 1992), which indicate a top-to-north displacement. Furthermore, the chromite-foliated anorthosite fault has N-S striking, normal-sense shear fractures and pseudotachylite-filled tensions gashes, both of which indicate E-W extension during the N-S compression.

As both faults display top-to-north displacements and are pseudotachylite-bearing, the faults are interpreted as being subsections of a larger fault system. Therefore, to determine the Bushveld Complex deformation event to which the faults are likely associated, the deformation event should account for N-S compressional and E-W extensional structures. Furthermore, the deformation should also account for a decrease in temperature from <500°C to <300°C, as recorded by the chromite-foliated anorthosite fault cataclastic-flow to stick-slip transition. As such, the P-T conditions and stress field of the footwall diapirism and RLS flexural-slip folding deformation events are considered for their suitability as a model for the development of the Jagdlust Farm fault system.

5.3.1 Diapirism

Diapirism of the Transvaal floor rocks was initiated at the onset of the emplacement of the RLS (Gerya et al., 2003; Clarke et al., 2005). Diapirism occurred at temperatures between 750°C and 550°C, resulting in the ductile deformation of the metasediments within the diapirs and the RLS rocks draped around the diapirs (Buick et al., 2000; Johnson et al., 2004; Longridge et al., 2009; Montjoie, 2018). Furthermore, Du Plessis and Walraven (1990) shows that the footwall diapirs within the Eastern Limb have a N-S extensional regime during emplacement. Therefore, considering the estimated P-T conditions at which the Jagdlust Farm fault system developed, and the top-to-north thrusting of the LG-6 reverse fault, diapirism does not account for the metamorphic grade, deformation regime or stress field orientation observed for the Jagdlust Farm fault system.

5.3.2 Flexural-slip folding induced by lithostatic loading

Perritt and Roberts (2007) proposed that the current, non-cylindrical fold geometry of the Bushveld Complex is the result of lithostatic loading owing to the mass of the RLS. In their model, low-temperature folding was achieved through flexural slip along newly-developed, chromitite-silicate contact controlled, layer-parallel faults, which are connected by layer-crosscutting ramp faults (Tanner, 1992a; Ismat and Mitra, 2005; Ismat, 2013). Across all localities within their study, layer-parallel faults have centripetal dips with slickenlines plunging in a dip-slip direction. This led the authors to conclude that the flexural slip was not driven by a regional compressive stress. As such, if lithostatic loading were the driving force for the development of the Jagdlust Farm fault system, layer-parallel faults would be expected to be SW-dipping with slickenlines on layer-parallel fracture surfaces plunging in the same SW-direction rather than being S-plunging. Owing to the discrepancy between the slickenlines plunging direction, flexural-slip folding induced by lithostatic loading, as proposed by Perritt and Roberts (2007) is rejected as the driving force for the development of the Jagdlust Farm fault system.

5.3.3 Proposed stress field

Several key features within the Jagdlust Farm fault system show that faulting occurred through layer-parallel shortening in the N-S direction (Logan, 1979; Swanson, 1988). The features that support top-to-north displacement are the south-dipping LG-6 reverse fault, the south-plunging slickenline cluster, the north-dipping R-R' fractures and south-dipping P-P" fractures, and the south-dipping sigmoidal fabric (Logan, 1979; Lister and Snoke, 1984; Swanson, 1988; Davis et al., 2000). The P-P" fractures and fault-parallel Y-shears with pseudotachylite-fill are also indicative of subhorizontal layer-parallel shortening in the N-S direction (Swanson, 1988).

The E- and W-dipping extensional shear fracture set was coeval with the generation of the cataclasite. Cataclasite is in turn, syngenetic with the pseudotachylite within the seismic cycle. Therefore, N-S layer-parallel shortening was synchronous with an E-W layer-parallel extension. Furthermore, scattering of slickenlines, particularly S-plunging slickenlines, indicates that strain within the system was three-dimensional (Tanner, 1989). Therefore, strain within the Jagdlust Farm fault system was heterogeneous in three dimensions with σ_1 being a compressional stress and both σ_2 and σ_3 being extensional stresses, producing an oblate strain ellipsoid with the orientation of the principal stress axes being N-S, E-W and subvertical for σ_1, σ_2 and σ_3, respectively (Figure 5.3) (Anderson, 1905; Sanderson and Marchini, 1984; Fossen and Cavalcante, 2017).

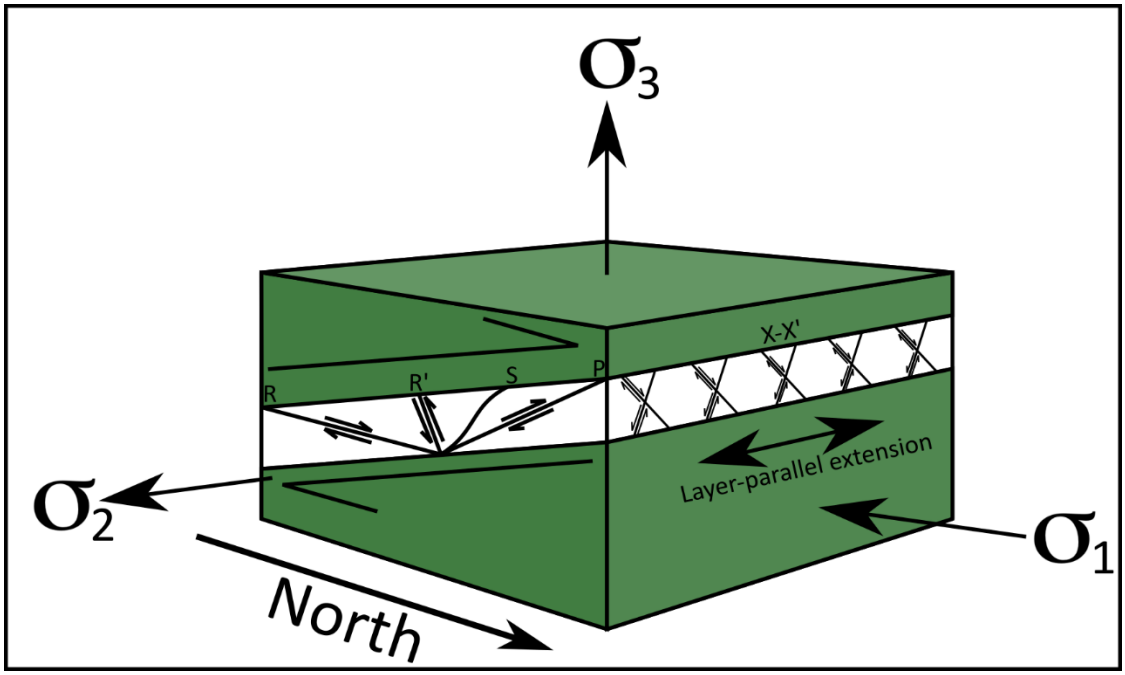


Figure 5.3: Block model of the chromite-foliated anorthosite fault, Jagdlust Farm fault system. The σ_1, σ_2, σ_3, principal stress axes are oriented subhorizontal N-S, subhorizontal E-W and subvertical, respectively. The σ_2 stress axis was tensile and therefore produced N-S trending extensional shear fractures associated with layer-parallel extension. Layer-parallel shortening in the N-S direction produced south-dipping sigmoidal fabric and P fractures, and north-dipping R-R' fractures.

5.4 Strain partitioning within the Jagdlust Farm stratigraphy

Despite the Jagdlust Farm chromite-foliated anorthosite fault being morphologically comparable to layer-parallel faults associated with flexural slip described within the Bushveld Complex (Tanner, 1989; Tanner, 1992b; Perritt and Roberts, 2007), the rheological controls in the development of the respective faults appear to be different. This is because there are several chromitite-silicate contacts within the Jagdlust Farm stratigraphic section, at which layer-parallel faults could form, but did not. Therefore, it is likely that layering was not the only heterogeneity controlling strain localization for the development of the layer-parallel fault (Sibson, 1977; Passchier, 1984; Ismat and Mitra, 2005; Sibson and Toy, 2006; Bjørnerud, 2010).

It is possible that the thicker overlying noritic and underlying pyroxenitic sequences (Cameron, 1963) exposed at Jagdlust Farm were more competent owing to the greater thickness and homogeneity of the layering, therefore distributing strain over a greater volume of rock (Torabi and Berg, 2011; Ord and Hobbs, 2013). This would partition the strain into the relatively thinner anorthosites (~2 m thick) at the lower-upper Critical zone boundary (Torabi and Berg, 2011; Ord and Hobbs, 2013). Furthermore, plagioclase dominated lithologies may preferentially accommodate slip owing to the poor cohesion of plagioclase cleavage planes (Macaudière and Brown, 1982; Brown and Macaudiére, 1984).

The layer-parallel fault, however, developed preferentially within the chromite-foliated anorthosite over the pyroxene-foliated anorthosite despite both anorthosite layers being predominantly plagioclase, having similar thicknesses and contacts with chromitite layers (Macaudière and Brown, 1982; Brown and Macaudiére, 1984; Perritt and Roberts, 2007; Torabi and Berg, 2011; Ord and Hobbs, 2013). Therefore, it is likely that the chromite-aggregate foliation within the anorthosite underlying the MG-4 chromitite was a significant controlling factor in the development of the layer-parallel fault. This is likely owing to the similarity in rheological response of pyroxene and plagioclase (He et al., 2013) and the contrast between plagioclase and chromite (Macaudière and Brown, 1982; Christiansen, 1986; He et al., 2013). Thus, owing to the chromite-plagioclase rheological contrast, the chromite aggregates provided enough heterogeneity for the localization of strain (Sibson, 1980; Crider, 2015), leading to the development of microfaults, seen as the foliation-parallel shear fractures, which are prolific throughout the sample set. This initial fracturing controlled the development of the fault through constraining failure to the layer by reactivating the pre-existing fractures and allowing crosscutting fractures to develop from the strain-softening of the layer (Manatschal, 1999; Speckbacher et al., 2013; Crider, 2015).

Chlorite is commonly associated with chromite deposits, particularly where deformation of the chromite has led to Mg exsolution (Liipo et al., 1994; Schulte et al., 2010). This phenomenon would explain the source of Mg for chloritization as well as the spatial association of the blebby-textured chloritization with chromite. As such, the chromite-aggregate foliation not only provided the rheological heterogeneity for strain partitioning at the chromite-foliated anorthosite-chromitite contact, but encouraged the chloritization of plagioclase (see Fletcher et al. (1997) and Ciesielczuk (2007) for possible direct and indirect reaction pathways) adjacent to the chromite grains, producing the blebby-textured chlorite. This chloritization of plagioclase would further emphasize the rheological contrast within the layer and overall stratigraphy (Manatschal, 1999; Caine et al., 2010; Bose et al., 2014), constraining the development of new slip-accommodating structures to the layer through fault zone weakening (Speckbacher et al., 2013).

It is concluded that the chromite-aggregate foliation was both directly, and indirectly fundamental in the strain partitioning that led to the development of the layer-parallel fault system at Jagdlust Farm and adjacent properties on the northern portion of the Eastern Limb.

5.5 Progressive evolution of faulting within the chromite-foliated anorthosite

The Jagdlust Farm chromite-foliated anorthosite fault, records layer-controlled, N-verging thrusting through a faulting mechanism transition from continuous cataclastic-flow to seismic stick-slip (Figure 5.4). Faulting was

initiated and controlled by strain partitioning at the chromite-plagioclase heterogeneity, with the initiation of foliation-parallel fractures (Figure 5.4A) (Sibson, 1980; Christiansen, 1986; He et al., 2013; Crider, 2015). These foliation-parallel fractures linked through propagation and the formation of R' fractures and sigmoidal shear fabrics, comminuting material into the fractures to produce the quasi-ductile appearance (House and Gray, 1982), resulting in the sigmoidal-fabric quasi-ductile cataclasite (Figure 5.4B). With continued shearing, comminution and cataclastic-flow, the sigmoidal-fabric quasi-ductile cataclasite zones grew in width and matrix volume, producing the sigmoidal-clast, quasi-ductile cataclasite (Figure 5.4C). Under the continuous cataclastic-flow regime, fluids freely circulated, producing the webbed-textured chloritization observed in the Fe-Mg-Cr composite elemental maps (Figure 5.4C).

As the ambient temperature in and around the fault system cooled below 300°C, the failure mechanism transitioned from cataclastic-flow to stick-slip (Tullis and Yund, 1987; Tullis, 1990; Hadizadeh and Tullis, 1992). With this transition, chloritization sealed the fault, reducing fluid circulation, which would allow for sufficient strain to be stored so as to produce coseismic slip (Figure 5.4C to D) (Manatschal, 1999; Bjørnerud, 2010; Caine et al., 2010), generating pseudotachylite and cataclasite (Figure 5.4D) (Fabbri et al., 2000; Di Toro and Pennacchioni, 2004; Bjørnerud, 2010; Bestmann et al., 2012; Rowe et al., 2012; Rowe and Griffith, 2015). Immediately after coseismic slip, the fault was permeable enough to allow the circulation of fluids (Figure 5.4D), which then resealed the fault through chloritization, preventing the primary failure mechanism reverting to cataclastic-flow and re-initiating the seismic cycle (Figure 5.4F) (Manatschal, 1999; Bjørnerud, 2010; Caine et al., 2010; Speckbacher et al., 2013).

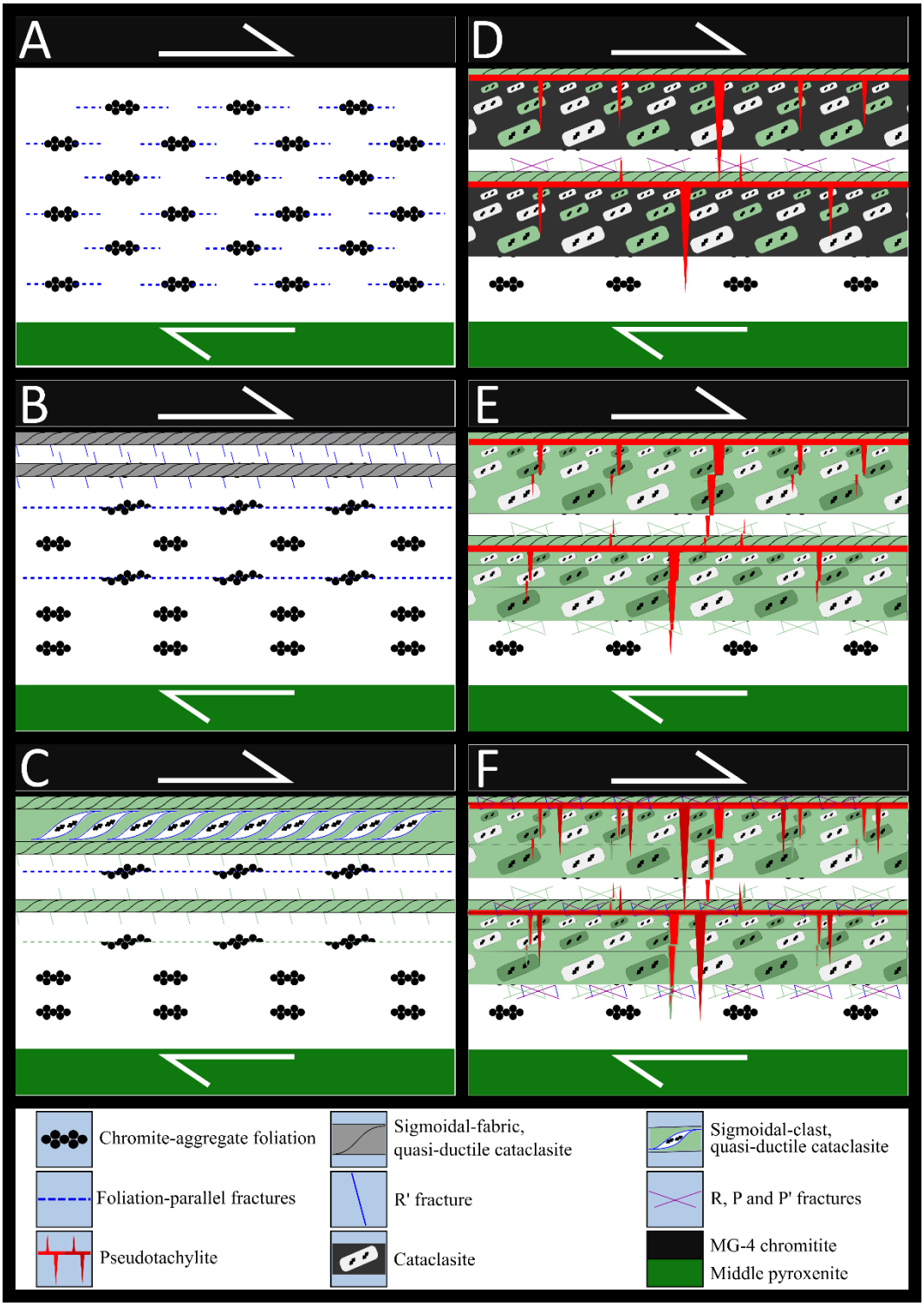


Figure 5.4: Fault development model for the chromite-foliated anorthosite fault. A) through C) sketch the initiation of the fault through to the development of sigmoidal-clast, quasi-ductile cataclasite. The transition from continuous cataclastic-flow to stick-slip occurs between C) and D). D) through F) sketch the development and chloritization of structures formed during stick-slip events. Chloritization is represented by a change in feature colour to light green.

5.6 Relative age for the development of the Jagdlust Farm Fault system

The Bushveld Complex emplacement, ca. 2061-2055 Ma (Buick et al., 2001; Zeh et al., 2015), and cooling, ca. 2054 Ma (Cawthorn and Walraven, 1998; Letts et al., 2009; Scoates and Wall, 2015), provide an upper age limit of the Jagdlust Farm fault system. However, as previously discussed, the chromite-foliated anorthosite fault records a temperature-dependent failure mechanism transition from cataclastic-flow to stick-slip, ca. 300°C (Hadizadeh and Tullis, 1992). This transition occurred under a N-S compressive stress regime and is associated with interseismic fluid circulation and chloritization. It is, therefore, possible to constrain the relative age of the Jagdlust Farm fault system by considering the cooling history of the Bushveld Complex, hydrothermal events, and regional stress fields post-Bushveld Complex emplacement.

5.6.1 Cooling history of the Bushveld Complex

The cooling history of the Bushveld Complex has been confined by tracking the closure temperatures of various thermochronology minerals within the Merensky Reef, the UG2, and the Critical Zone gabbros (Nomade et al., 2004; Cassata et al., 2009; Coggon et al., 2012; Scoates and Wall, 2015). This method reveals two periods of cooling over the cataclastic-flow to stick-slip temperature transition (Hadizadeh and Tullis, 1992; Scoates and Wall, 2015). The first is associated with the emplacement and cooling of the Bushveld Complex (Scoates and Wall, 2015). This period is associated high-temperature (>750°C-550°C) fluid circulation and diapirism of the Transvaal footwall (Du Plessis and Walraven, 1990; Buick et al., 2000; Buick et al., 2001; Gerya et al., 2003; Clarke et al., 2005).

The second is a hydrothermal resetting event postulated from apatite, biotite, plagioclase and PGM geochronology studies producing discordant ages to those produced by zircon and rutile geochronology studies (Nomade et al., 2004; Cassata et al., 2009; Coggon et al., 2012; Scoates and Wall, 2015). These studies show resetting occurred, including error brackets, between 2.04 Ga and 1.95 Ga (Scoates and Wall, 2015), and is associated with chloritization (Nomade et al., 2004). Furthermore, these ages coincide with the Limpopo belt orogeny (Kramers et al., 2011a; Kramers et al., 2011b; Scoates and Wall, 2015). This second period of cooling better suits the conditions under which the faults developed, for several reasons, including; the Curie and closure temperatures for magnetite and apatite, respectively, hydrothermal chlorite growth and documented evidence for N-S directed, compressive stress based on observed deformation within the Transvaal Supergroup and Bushveld Complex rocks as well as the northern block of the Kaapvaal Craton.

The apatite closure temperature ranges between 620°C and 375°C (Krogstad and Walker, 1994; Kirkland et al., 2018); an upper limit that exceeds the magnetite Curie temperature of 580°C (Letts et al., 2009). The overlapping of these temperatures leaves the possibility open that, had the rotation of the RLS layering occurred before the hydrothermal resetting of apatite occurred, the magnetite palaeomagnetic properties would be reset to show inclined layering (Clarke et al., 2005; Perritt and Roberts, 2007; Letts et al., 2009). Therefore, albeit not definitive, the resetting of apatite suggests that Jagdlust Farm fault system could have developed after the hydrothermal resetting of apatite within the Bushveld Complex, which occurred ca. 2029-1997 Ma (Scoates and Wall, 2015).

Retrograde hydrothermal fluid circulation associated with the cooling of the Bushveld Complex produced high-grade (>750°C) metamorphic mineral assemblages within the Transvaal Supergroup host rocks (Buick et al., 2000; Buick et al., 2001; Johnson et al., 2004; Longridge et al., 2009). These assemblages are in contrast to the chloritization of the Jagdlust Farm fault system, which would occur <550°C (James et al., 1976; de Caritat et al., 1993; Battaglia, 1999). Furthermore, the most age-discordant $^{40}Ar/^{39}Ar$ biotite ratios from the Merensky Reef, are produced by highly chloritized biotite grains (Nomade et al., 2004), suggesting that the hydrothermal reset of biotite, ca. 2.04 Ga (Nomade et al., 2004), was associated with chloritizing fluids. Therefore, the chloritization of the Jagdlust Farm fault system during cataclastic-flow and later interseismic periods, suggests that the development of the system is synchronous with the second cooling period.

5.6.2 Regional stress field

Several transpressional and hydrothermal structures and systems in the Bushveld Complex and surrounding Transvaal rocks indicate a broadly N-S compressional stress following the emplacement of the Bushveld Complex (Du Plessis and Walraven, 1990; De Wit and Good, 1997; Basson, 2019). The most notable of these is the Mhlapitsi Belt, which is directly north of Jagdlust Farm and the surrounding study area.

The Mhlapitsi Belt is a pre-Bushveld Complex fold and thrust belt within the Chuniespoort Group and Penge Formation of the Transvaal Supergroup (Miyano et al., 1987; McCourt, 1995; Basson and Koegelenberg, 2016; Smith and Beukes, 2016). The belt is an ENE-trending subsection of the TML, which formed by syn- to post-Bushveld Complex age, N-verging thrusting along reactivated normal faults (Du Plessis and Walraven, 1990; McCourt, 1995; De Wit and Good, 1997; Anhaeusser, 2006; Basson and Koegelenberg, 2016). Sills associated with Bushveld Complex magmatism and Pilanesberg dykes intruded the belt (Basson and Koegelenberg, 2016). As both intrusive events exhibit deformation structures, with the Pilanesberg dykes being less-deformed than the Bushveld Complex sills (Basson and Koegelenberg, 2016), the Mhlapitsi Belt appears to have undergone long-

lived deformation post-Bushveld Complex emplacement. Furthermore, it possible to tentatively associate this deformation of the Mhlapitsi belt to the chromite-foliated anorthosite fault through the observed termination of the dykes against the chromite-foliated anorthosite layer.

Other notable structures include the post-Bushveld Complex, strike-slip reactivation of the Rustenburg, Steelpoort and Wonderkop faults (Molyneux and Klinkert, 1978; Du Plessis and Walraven, 1990; Bumby et al., 1998; Uken, 1998; Basson, 2019) as well as TML hydrothermal and strike-slip activity, dated at 2.02-1.85 Ga within Goedgedacht, Buffalo fluorspar mine and various Waterberg transpressional systems (De Wit and Good, 1997), thrusting within the Merensky Reef (Nomade et al., 2004; Basson, 2019) and N-verging compressional structures within the Pretoria Group north of the Johannesburg Dome (Courtnage, 1995; Gibson et al., 1999).

Low-angle thrusting is observed within the Merensky Reef of the RLS Critical zone (Nomade et al., 2004; Basson, 2019). The vergence of the thrusting is not mentioned, however, the faulting is associated with hydrothermal biotite growth, which has been dated at 2.04 Ga (Nomade et al., 2004; Basson, 2019).

N-verging structures within the Pretoria Group exposed between the Johannesburg Dome and Bushveld Complex are described by Courtnage (1995) and Gibson et al. (1999). These structures include N-verging folding and layer-parallel faults (Courtnage, 1995; Gibson et al., 1999) as well as S-verging folding and localised E- and W-verging structures (Courtnage, 1995). All structures are post-Bushveld Complex and pre-Pilanesberg dyke swarm in age with Gibson et al. (1999) attributing the development of the structures to the 2.02 Ga Vredefort Impact. However, Alexandre et al. (2006) showed that the cleavages that developed within these rocks formed separately at 2.04 Ga, and therefore, as Courtnage (1995) suggested, it is possible that the observed structures developed during a long-lived deformation event.

Furthermore, high-grade, W- to WSW-trending, transpression-accommodating shears within the Northern Margin and Central zones of the Limpopo belt orogeny have been dated at 2.04-1.95 Ga and 2.02 ± 0.02 Ga, respectively (Kramers et al., 2011a; Kramers et al., 2011b). The displacement sense along these structures is debated, however, they appear to have developed under a broadly N-S compressional regime (Kramers et al., 2011a; Kramers et al., 2011b). These structures provide important insight into the structural history of the TML, providing a regional context for the strike-slip reactivation of the TML post-Bushveld Complex emplacement. This is because the development and reactivation of the Limpopo orogenic belt has contributed to reactivation of and hydrothermal activity within the greater TML (De Wit and Good, 1997).

Therefore, having considered the structures within the Bushveld Complex and surrounding Transvaal Supergroup rocks along with structures at the northern margins of the Kaapvaal Craton, the Jagdlust Farm fault system is likely to have formed in response to a broadly N-S compressional stress regime dated at 2.04-1.85 Ga (Du Plessis and Walraven, 1990; Courtnage, 1995; De Wit and Good, 1997; Gibson et al., 1999; Alexandre et al., 2006; Basson and Koegelenberg, 2016). This age is in agreement with the second period of cooling and hydrothermal resetting of the Bushveld Complex (Nomade et al., 2004; Coggon et al., 2012; Scoates and Wall, 2015).

5.7 Structural relationship of the Jagdlust Farm fault system to the Thabazimbi-Murchison Lineament

The sinistral, strike-slip displacement that occurred along the TML post-Bushveld Complex emplacement was possibly accompanied by up to 10 km of northern block up-lift (Du Plessis and Walraven, 1990; De Wit and Good, 1997; Basson, 2019). This may provide key insight into the formation of the Jagdlust Farm fault system and Mhlapitsi Belt.

Shear studies of analogue materials with crosscutting elements have produced flanking-structures comparable to natural structures, which form adjacent to crosscutting faults, shear fractures and veins (Grasemann and Stuwe, 2001; Grasemann et al., 2003; Exner et al., 2004). Regarding this study, the most notable of these structures are S-type flanking folds. These folds are convex in the direction of shear and form along crosscutting elements, which are at low-angles to the shear direction (Figure 5.5A) (Grasemann and Stuwe, 2001; Grasemann et al., 2003).

Within the context of a NE-stress field and sinistral-slip along the TML, the ENE-trending TML would have a low-angle with respect to the direction of shear (Du Plessis and Walraven, 1990; Anhaeusser, 2006). This low-angle with respect to the TML shear direction would be favourable for the development of flanking S-folds (Grasemann and Stuwe, 2001; Grasemann et al., 2003; Exner et al., 2004) within the Transvaal Supergroup and RLS rocks adjacent to the TML (Figure 5.5B and C). This folding would result in the observed steepening of the Mhlapitsi Belt and RLS rocks south of and adjacent to TML (Du Plessis and Walraven, 1990; McCourt, 1995; De Wit and Good, 1997; Basson and Koegelenberg, 2016; Basson, 2019).

The Jagdlust Farm fault system is proposed to form in response to the folding of the RLS and reactivation of the Mhlapitsi Belt (Figure 5.5C). Failure of the chromite-foliated anorthosite fault was controlled by mineralogical variation across and within layering. This control mimics the low-temperature, brittle failure associated with

folding via flexural slip (Tanner, 1989; Tanner, 1992b; Tanner, 1992a). The LG-6 thrust formed either as a ramp fault associated with flexural slip or as antithetic thrusting associated with the general S-verging thrusting observed within RLS rocks abutting the TML (Tanner, 1989; Tanner, 1992b; Tanner, 1992a; De Wit and Good, 1997; Basson, 2019).

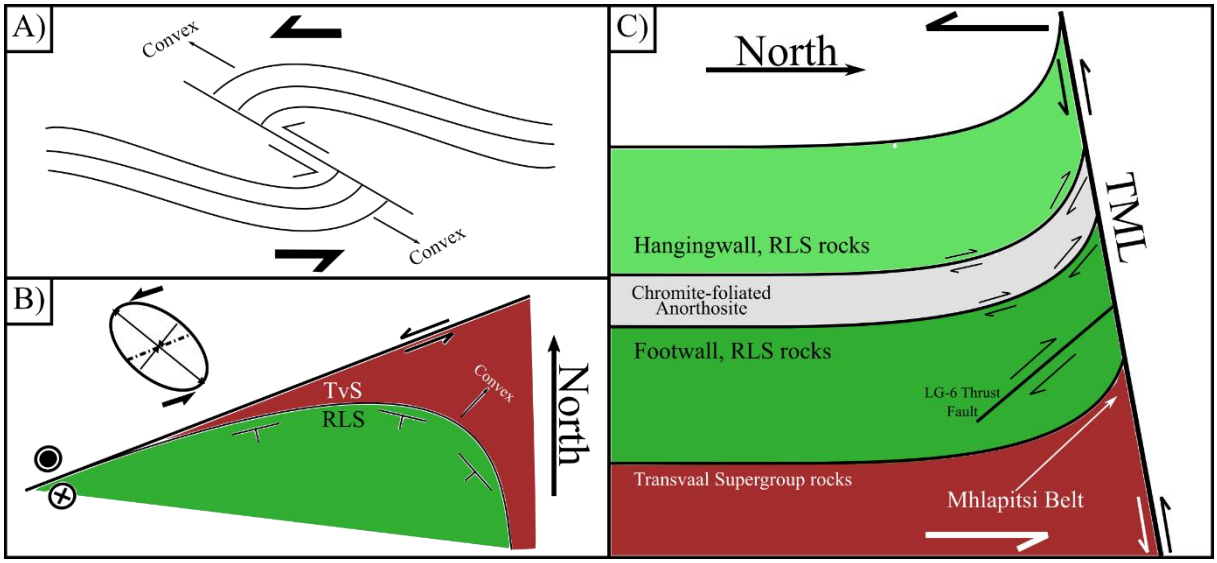


Figure 5.5: A) Schematic diagram, after Grasemann et al. (2003) of an S-type flanking fold developing under a sinistral shear-sense. B) Schematic diagram, in plan-view, showing the relationship of the TML with the RLS and Transvaal Supergroup (TvS) rocks. Sinistral-shear, with up-throw of the northern block, along the TML, is thought to produce a regional S-type flanking fold within the RLS layering (approximate strike and dip-direction shown). Shearing is a response to the approximately NE-SW compression and NW-SE extension proposed by Du Plessis and Walraven (1990). The Wonderkop and Steelpoort faults are omitted from the diagram. C) West-facing, schematic cross-section of the TML and abutting down-thrown, southern block with the RLS and Transvaal Supergroup rocks represented. The relationship of the chromite-foliated anorthosite fault and LG-6 reverse fault, as well as the Mhlapitsi Belt, are shown in relation to the TML. Layer steepening of the RLS and TvS rocks abutting the TML is expected with northern block up-throw through the development of an S-type flanking fold.

5.8 Summary

Two faults are exposed at Jagdlust Farm and adjacent properties, within the northern portion of the Bushveld Complex Eastern Limb. The stratigraphically-lower fault crosscuts the LG-6 chromitite with a reverse-sense of displacement. The stratigraphically-higher fault is a layer-parallel fault within the chromite-foliated anorthosite near the lower-upper Critical Zone boundary. This fault is shown to have a top-to-north, reverse-sense displacement. Furthermore, the fault is shown to have undergone a transition at ~300°C from cataclastic flow to stick-slip as the primary faulting mechanism. The stick-slip faulting mechanism is shown to have undergone several seismic-interseismic cycles with coseismic slip producing friction melt preserved as pseudotachylite. The

LG-6 thrust and chromite-foliated anorthosite faults are interpreted to form part of the same fault system owing to the similar vergence and presence of pseudotachylite within both faults.

The fault system is proposed to have developed under a 2.04-1.95 Ga, broadly N-S compressive, regional stress regime covering the northern section of the Kaapvaal Craton. This stress field resulted in the reactivation of the TML with sinistral strike-slip movement accompanied by northern block up-throw. This displacement along the TML is suggested to have formed a S-type flanking folding within the RLS and Transvaal Supergroup rocks south of, and adjacent to, the TML. This folding would produce the observed dip-steepening of the RLS and Mhlapitsi Belt along the TML. Faulting within the chromite-foliated anorthosite was controlled by both layer thickness and a mineralogical competency contrast. Consequently, the chromite-foliated anorthosite fault has similarities with layer-parallel flexural slip, but does not conform to the flexural slip folding induced by lithostatic loading model proposed by Perritt and Roberts (2007).

References

Alexandre, P., Andreoli, M. A. G., Jamison, A., and Gibson, R. L., 2006, 40Ar/39Ar age constraints on low-grade metamorphism and cleavage development in the Transvaal Supergroup (central Kaapvaal craton, South Africa): implications for the tectonic setting of the Bushveld Igneous Complex: South African Journal of Geology, v. 109, no. 3, p. 393-410.

Allen, A., 1979, Mechanism of frictional fusion in fault zones: Journal of Structural Geology, v. 1, no. 3, p. 231-243.

Anderson, E. M., 1905, The dynamics of faulting: Transactions of the Edinburgh Geological Society, v. 8, no. 3, p. 387.

Anhaeusser, C., 2006, A reevaluation of Archean intracratonic terrane boundaries on the Kaapvaal Craton, South Africa: Collisional suture zones?, Volume 405, p. 193-210.

Basson, I., 2019, Cumulative deformation and original geometry of the Bushveld Complex: Tectonophysics, v. 750, p. 177-202.

Basson, I., and Koegelenberg, C., 2016, Structural Controls on Fe Mineralization at Thabazimbi Mine, South Africa: Ore Geology Reviews, v. 80.

Battaglia, S., 1999, Applying X-ray geothermometer diffraction to a chlorite: Clays and Clay Minerals, v. 47, no. 1, p. 54-63.

Bestmann, M., Pennacchioni, G., Mostefaoui, S., Göken, M., and de Wall, H., 2016, Instantaneous healing of micro-fractures during coseismic slip: Evidence from microstructure and Ti in quartz geochemistry within an exhumed pseudotachylyte-bearing fault in tonalite: Lithos, v. 254-255, p. 84-93.

Bestmann, M., Pennacchioni, G., Nielsen, S., Göken, M., and de Wall, H., 2012, Deformation and ultrafine dynamic recrystallization of quartz in pseudotachylyte-bearing brittle faults: A matter of a few seconds: Journal of Structural Geology, v. 38, p. 21-38.

Bjørnerud, M., 2010, Rethinking conditions necessary for pseudotachylyte formation: Observations from the Otago schists, South Island, New Zealand: Tectonophysics, v. 490, no. 1-2, p. 69-80.

Bjørnerud, M., and Magloughlin, J., 2004, Pressure-related feedback processes in the generation of pseudotachylytes: Journal of Structural Geology, v. 26, no. 12, p. 2317-2323.

Bose, S., Mandalb, N., Saha, P., Sarkar, S., and Lithgow-Bertelloni, C., 2014, Thrust initiation and its control on tectonic wedge geometry: An insight from physical and numerical models.

Brindley, G. W., 1949, Mineralogy and Crystal Structure of Chamosite: Nature, v. 164, no. 4164, p. 319-320.

Brown, W. L., and Macaudiére, J., 1984, Microfracturing in relation to atomic structure of plagioclase from a deformed meta-anorthosite: Journal of Structural Geology, v. 6, no. 5, p. 579-586.

Buick, I., Gibson, R., Cartwright, I., Maas, R., Wallmach, T., and Uken, R., 2000, Fluid flow in metacarbonates associated with emplacement of the Bushveld Complex, South Africa: Journal of Geochemical Exploration, v. 69, p. 391-395.

Buick, I. S., Maas, R., and Gibson, R., 2001, Precise U–Pb titanite age constraints on the emplacement of the Bushveld Complex, South Africa: Journal of the Geological Society, v. 158, no. 1, p. 3-6.

Bumby, A. J., Eriksson, P. G., and Van der Merwe, R., 1998, Compressive deformation in the floor rocks to the Bushveld Complex (South Africa): evidence from the Rustenburg Fault Zone: Journal of African Earth Sciences, v. 27, no. 3, p. 307-330.

Caine, J. S., Bruhn, R. L., and Forster, C. B., 2010, Internal structure, fault rocks, and inferences regarding deformation, fluid flow, and mineralization in the seismogenic Stillwater normal fault, Dixie Valley, Nevada: Journal of Structural Geology, v. 32, no. 11, p. 1576-1589.

Cameron, E. N., 1963, Structure and rock sequences of the Critical Zone of the eastern Bushveld Complex: Spec. Pap., mineral. Soc. Am, v. 1, p. 93-107.

Cassata, W., Renne, P., and Shuster, D., 2009, Argon diffusion in plagioclase and implications for thermochronometry: A case study from the Bushveld Complex, South Africa: Geochimica Et Cosmochimica Acta - GEOCHIM COSMOCHIM ACTA, v. 73.

Cawthorn, R., and Webb, S., 2001, Connectivity between the western and eastern limbs of the Bushveld Complex: Tectonophysics, v. 330, no. 3-4, p. 195-209.

Cawthorn, R. G., 2015, The Bushveld Complex, South Africa, *in* Charlier, B., Namur, O., Latypov, R., and Tegner, C., eds., Layered Intrusions: Dordrecht, Springer Netherlands, p. 517-587.

Cawthorn, R. G., and Walraven, F., 1998, Emplacement and crystallization time for the Bushveld Complex: Journal of Petrology, v. 39, no. 9, p. 1669-1687.

Chester, F. M., and Logan, J. M., 1987, Composite planar fabric of gouge from the Punchbowl Fault, California: Journal of Structural Geology, v. 9, no. 5, p. 621-IN626.

Christiansen, F. G., 1986, Deformation of chromite: S.E.M. investigations: Tectonophysics, v. 121, no. 2, p. 175-196.

Ciesielczuk, J., 2007, Hydrothermal activity in the Strzelin granite (Poland): Granitoids in Poland. AM Monograph, v. 1, p. 231-242.

Clarke, B., Uken, R., and Reinhardt, J., 2009, Structural and compositional constraints on the emplacement of the Bushveld Complex, South Africa: Lithos, v. 111, no. 1-2, p. 21-36.

Clarke, B. M., Uken, R., Watkeys, M. K., and Reinhardt, J. r., 2005, Folding of the Rustenburg layered suite adjacent to the Steelpoort pericline: implications for syn-Bushveld tectonism in the eastern Bushveld Complex: South African Journal of Geology, v. 108, no. 3, p. 397-412.

Coggon, J. A., Nowell, G. M., Pearson, D. G., Oberthür, T., Lorand, J. P., Melcher, F., and Parman, S. W., 2012, The 190Pt–186Os decay system applied to dating platinum-group element mineralization of the Bushveld Complex, South Africa: Chemical Geology, v. 302-303, p. 48-60.

Courtnage, P. M., 1995, Post-Transvaal deformation between the Johannesburg Dome and Bushveld Complex [Master of Science: University of the Witwatersrand.

Crider, J. G., 2015, The initiation of brittle faults in crystalline rock: Journal of Structural Geology, v. 77, p. 159-174.

Davis, G. H., Bump, A. P., García, P. E., and Ahlgren, S. G., 2000, Conjugate Riedel deformation band shear zones: Journal of Structural Geology, v. 22, no. 2, p. 169-190.

de Caritat, P., Hutcheon, I., and Walshe, J. L., 1993, Chlorite Geothermometry: A Review: Clays and Clay Minerals, v. 41, no. 2, p. 219-239.

De Wit, M. J., and Good, N., 1997, The Thabazimbi-Murchison Lineament of the Kaapvaal Craton, South Africa: 2700 Ma of episodic deformation: Journal of the Geological Society, v. 154, no. 1, p. 93-97.

Di Toro, G., and Pennacchioni, G., 2004, Superheated friction-induced melts in zoned pseudotachylytes within the Adamello tonalites (Italian Southern Alps): Journal of Structural Geology, v. 26, no. 10, p. 1783-1801.

Drake, M. J., 1976, Plagioclase—melt equilibria: Geochimica et Cosmochimica Acta, v. 40, no. 4, p. 457-465.

Du Plessis, C., and Walraven, F., 1990, The tectonic setting of the Bushveld Complex in Southern Africa, Part 1. Structural deformation and distribution: Tectonophysics, v. 179, no. 3-4, p. 305-319.

Eales, H., and Cawthorn, R., 1996, The bushveld complex, Developments in Petrology, Volume 15, Elsevier, p. 181-229.

Esri, 23 June 2013, High Resolution 30cm Imagery: Esri, https://www.arcgis.com/home/item.html?id=c1c2090ed8594e0193194b0193750d0193190d0193195f0193183, scale No scale given.

Evans, J., 1988, Deformation mechanisms in granitic rocks at shallow crustal levels, 437-443 p.:

Exner, U., Mancktelow, N. S., and Grasemann, B., 2004, Progressive development of s-type folds in simple shear: Journal of Structural Geology, v. 26, p. 2191-2201.

Fabbri, O., Lin, A., and Tokushige, H., 2000, Coeval formation of cataclasite and pseudotachylyte in a Miocene forearc granodiorite, southern Kyushu, Japan: Journal of Structural Geology, v. 22, no. 8, p. 1015-1025.

Faber, C., Rowe, C. D., Miller, J. A., Fagereng, Å., and Neethling, J. H., 2014, Silica gel in a fault slip surface: Field evidence for palaeo-earthquakes?: Journal of Structural Geology, v. 69, p. 108-121.

Faulkner, D. R., Jackson, C. A. L., Lunn, R. J., Schlische, R. W., Shipton, Z. K., Wibberley, C. A. J., and Withjack, M. O., 2010, A review of recent developments concerning the structure, mechanics and fluid flow properties of fault zones: Journal of Structural Geology, v. 32, no. 11, p. 1557-1575.

Feig, S. T., Koepke, J., and Snow, J. E., 2006, Effect of water on tholeiitic basalt phase equilibria: an experimental study under oxidizing conditions: Contributions to Mineralogy and Petrology, v. 152, no. 5, p. 611-638.

-, 2010, Effect of oxygen fugacity and water on phase equilibria of a hydrous tholeiitic basalt: Contributions to Mineralogy and Petrology, v. 160, no. 4, p. 551-568.

Ferry, J. M., 1979, Reaction mechanisms, physical conditions, and mass transfer during hydrothermal alteration of mica and feldspar in granitic rocks from south-central Maine, USA: Contributions to Mineralogy and Petrology, v. 68, no. 2, p. 125-139.

Fletcher, J., Stephens, C., Petersen, E., and Skerl, L., 1997, Greenschist facies hydrothermal alteration of oceanic gabbros: a case study of element mobility and reaction paths: Proceedings of the Ocean Drilling Program Scientific Results, v. 153.

Fossen, H., and Cavalcante, C., 2017, Shear zones – A review: Earth-Science Reviews, v. 171.

Fusseis, F., and Handy, M., 2008, Micromechanisms of shear zone propagation at the brittle–viscous transition, 1242-1253 p.:

Gerya, T. V., Uken, R., Reinhardt, J. r., Watkeys, M. K., Maresch, W. V., and Clarke, B. M., 2003, Cold fingers in a hot magma: Numerical modeling of country-rock diapirs in the Bushveld Complex, South Africa: Geology, v. 31, no. 9, p. 753-756.

Gibson, R. L., Courtnage, P. M., and Charlesworth, E. G., 1999, Bedding-parallel shearing and related deformation in the lower Transvaal Supergroup north of the Johannesburg Dome, South Africa: South African Journal of Geology, v. 102, no. 2, p. 99-108.

Glasser, F., and Osborn, E., 1958, Phase Equilibrium Studies in the System CaO-Cr2O3-SiO2: Journal of the American Ceramic Society, v. 41, no. 9, p. 358-367.

Grasemann, B., and Stuwe, K., 2001, The development of flanking folds during simple shear and their use as kinematic indicators: Journal of Structural Geology, v. 23, p. 715-724.

Grasemann, B., Stüwe, K., and Vannay, J.-C., 2003, Sense and non-sense of shear in flanking structures, 19-34 p.:

Greyvensteyn, R. M., 2001, A GIS-based structural analysis of the Bushveld Complex and surrounding areas [MSc MSc Dissertation]: University of Pretoria.

Hadizadeh, J., and Tullis, J., 1992, Cataclastic flow and semibrittle deformation of anorthite: Journal of Structural Geology - J STRUCT GEOL, v. 14, p. 57-63.

Hartzer, F. J., 1995, Transvaal Supergroup inliers: geology, tectonic development and relationship with the Bushveld complex, South Africa: Journal of African Earth Sciences, v. 21, no. 4, p. 521-547.

He, C., Luo, L., Hao, Q.-M., and Zhou, Y., 2013, Velocity-weakening behavior of plagioclase and pyroxene gouges and stabilizing effect of small amounts of quartz under hydrothermal conditions: Journal of Geophysical Research: Solid Earth, v. 118, no. 7, p. 3408-3430.

Higgins, M., 1971, Cataclastic rocks: Geological Survey Professional paper. 687, 79 p, Washington.

House, W. M., and Gray, D. R., 1982, Cataclasites along the Saltville thrust, U.S.A. and their implications for thrust-sheet emplacement: Journal of Structural Geology, v. 4, no. 3, p. 257-269.

Hrstka, T., Gottlieb, P., Skala, R., Breiter, K., and Motl, D., 2018, Automated mineralogy and petrology - applications of TESCAN Integrated Mineral Analyzer (TIMA): Journal of Geosciences, v. 63, no. 1, p. 47-63.

Irvine, T. N., 2015, Chromium: Its Physicochemical Behavior and Petrologic Significance: Papers from a Carnegie Institution of Washington Conference, Geophysical Laboratory, Elsevier Science.

Ismat, Z., 2013, Block-supported cataclastic flow within the upper crust: Journal of Structural Geology, v. 56, p. 118–128.

Ismat, Z., and Mitra, G., 2005, Folding by cataclastic flow: evolution of controlling factors during deformation: Journal of Structural Geology, v. 27, no. 12, p. 2181-2203.

James, R. S., Turnock, A. C., and Fawcett, J. J., 1976, The stability and phase relations of iron chlorite below 8.5 kb Contributions to Mineralogy and Petrology, v. 56, no. 1, p. 1-25.

Jerram, D., and Petford, N., 2011, The field description of igneous rocks, John Wiley & Sons.

Johnson, T., Brown, M., Gibson, R., and Wing, B., 2004, Spinel-cordierite symplectites replacing andalusite: Evidence for melt-assisted diapirism in the Bushveld Complex, South Africa: Journal of Metamorphic Geology, v. 22, p. 529-545.

Keith, M., 1954, Phase Equilibria in the System MgO-Cr2O3-SiO2: Journal of the American Ceramic Society, v. 37, no. 10, p. 490-496.

Kirkland, C. L., Yakymchuk, C., Szilas, K., Evans, N., Hollis, J., McDonald, B., and Gardiner, N. J., 2018, Apatite: a U-Pb thermochronometer or geochronometer?: Lithos, v. 318-319, p. 143-157.

Kramers, J., McCourt, S., Roering, C., Smit, C., and van Reenen, D., 2011a, Tectonic models proposed for the Limpopo Complex: Mutual compatibilities and constraints, Volume 207, p. 311-324.

Kramers, J. D., Mouri, H., van Reenen, D. D., Kramers, J. D., McCourt, S., and Perchuk, L. L., 2011b, The geochronology of the Limpopo Complex: A controversy solved, Origin and Evolution of Precambrian High-Grade Gneiss Terranes, with Special Emphasis on the Limpopo Complex of Southern Africa, Volume 207, Geological Society of America, p. 0.

Krogstad, E. J., and Walker, R. J., 1994, High closure temperatures of the U-Pb system in large apatites from the Tin Mountain pegmatite, Black Hills, South Dakota, USA: Geochimica et Cosmochimica Acta, v. 58, no. 18, p. 3845-3853.

Kruger, F. J., 2005, Filling the Bushveld Complex magma chamber: lateral expansion, roof and floor interaction, magmatic unconformities, and the formation of giant chromitite, PGE and Ti-V-magnetitite deposits: Mineralium Deposita, v. 40, no. 5, p. 451-472.

Letts, S., Torsvik, T. H., Webb, S. J., and Ashwal, L. D., 2009, Palaeomagnetism of the 2054 Ma Bushveld Complex (South Africa): implications for emplacement and cooling: Geophysical Journal International, v. 179, no. 2, p. 850-872.

Liipo, J., Vuollo, J., Nykänen, V., and Piirainen, T., 1994, Chrome spinel compositions as evidence for an Archaean ophiolite in the Kuhmo greenstone belt in Finland: Bulletin of the Geological Society of Finland, v. 66, p. 3-18.

Lin, A., 1994a, Glassy pseudotachylyte veins from the Fuyun fault zone, northwest China: Journal of Structural Geology, v. 16, no. 1, p. 71-83.

-, 1994b, Microlite Morphology and Chemistry in Pseudotachylite, from the Fuyun Fault Zone, China: The Journal of Geology, v. 102, no. 3, p. 317-329.

-, 2008, Fragments Within Pseudotachylyte Veins, *in* Friedman, G. M., and Seilacher, A., eds., Fossil earthquakes: the formation and preservation of pseudotachylites: Germany, Springer, p. 139-158.

Lin, A., and Shimamoto, T., 1998, Selective melting processes as inferred from experimentally generated pseudotachylytes: Journal of Asian Earth Sciences, v. 16, no. 5, p. 533-545.

Lister, G., and Snoke, A., 1984, S-C mylonites, 617-638 p.:

Logan, J., Experimental studies of simulated gouge and their application to studies of natural fault zones, *in* Proceedings Proceedings of conference VIII-analysis of actual fault zones in bedrock1979, p. 305-343.

Logan, J., Dengo, C., Higgs, N., and Wang, Z., 1992, Fabrics of experimental fault zones: Their development and relationship to mechanical behavior, International Geophysics, Volume 51, Elsevier, p. 33-67.

Longridge, L., Gibson, R. L., and Nex, P. A., 2009, Structural controls on melt segregation and migration related to the formation of the diapiric Schwerin Fold in the contact aureole of the Bushveld Complex, South Africa: Earth and Environmental Science Transactions of The Royal Society of Edinburgh, v. 100, no. 1-2, p. 61-76.

Macaudière, J., and Brown, W. L., 1982, Transcrystalline shear fracturing and pseudotachylite generation in a meta-anorthosite (Harris, Scotland): Journal of Structural Geology, v. 4, no. 4, p. 395-406.

Maddock, R. H., Grocott, J., and Van Nes, M., 1987, Vesicles, amygdales and similar structures in fault-generated pseudotachylytes: Lithos, v. 20, no. 5, p. 419-432.

Magloughlin, J. F., 1989, The nature and significance of pseudotachylite from the Nason terrane, North Cascade Mountains, Washington: Journal of Structural Geology, v. 11, no. 7, p. 907-917.

Magloughlin, J. F., and Spray, J. G., 1992, Frictional melting processes and products in geological materials: introduction and discussion: Tectonophysics, v. 204, no. 3-4, p. 197-204.

Manatschal, G., 1999, Fluid- and reaction-assisted low-angle normal faulting: evidence from rift-related brittle fault rocks in the Alps (Err Nappe, eastern Switzerland): Journal of Structural Geology, v. 21, no. 7, p. 777-793.

Mavimbela, P., 2013, Metamorphism in the contact aureole of the Eastern limb of the Bushveld Comples, South Africa [Master of Science Dissertation]: University of Pretoria, 131 p.

McCourt, S., 1995, The crustal architecture of the Kaapvaal crustal block South Africa, between 3.5 and 2.0 Ga: Mineralium Deposita, v. 30, no. 2, p. 89-97.

Miyano, T., 8eukes, N. J., amp, and van Reenen, D. D., 1987, Metamorphic evidence for early post-Bushveld sills in the Penge Iron Formation, Transvaal Sequence, Eastern Transvaal: South African Journal of Geology, v. 90, no. 1, p. 37-43.

Molyneux, P. S., and Klinkert, T. G., 1978, A structural interpretation of part of the Eastern Mafic Lobe of the Bushveld Complex and its surrounds: South African Journal of Geology, v. 81, no. 3, p. 359-368.

Mondal, S. K., and Mathez, E. A., 2006, Origin of the UG2 chromitite layer, Bushveld Complex: Journal of Petrology, v. 48, no. 3, p. 495-510.

Montjoie, R., 2018, Discovery and resource evaluation of the Lesego Platinum Merensky Reef and UG2 Chromitite hosted Platinum Group Metals deposit adjacent to the Phosiri Dome and the associated effects of the Phosiri Dome on the reef horizons, Bushveld Complex, South Africa [Master of Science Dissertation]: University of the Witwatersrand, 91 p.

Morley, C., and Guerin, G., 1996, Comparison of gravity-driven deformation styles and behavior associated with mobile shales and salt: Tectonics, v. 15, p. 1154-1170.

Morse, S. A., 1980, Basalts and phase diagrams: an introduction to the quantitative use of phase diagrams in igneous petrology, Springer Verlag.

Muan, A., and Sömiya, S., 1959, Phase Equilibrium Studies in the System Iron Oxide-Al2O3-Cr2O3: Journal of the American Ceramic Society, v. 42, no. 12, p. 603-613.

-, 1960, Phase equilibria in the system iron oxide—Cr2O3–SiO2 in air: Journal of the American Ceramic society, v. 43, no. 10, p. 531-541.

Nel, J., 1984, Geochemical and thermodynamic controls on the formation of mineral assemblages from the metamorphic aureole of the Bushveld complex in the Potgietersrus area. [MSc thesis: University of Pretoria.

Newman, P. J., and Ashley Griffith, W., 2014, The work budget of rough faults: Tectonophysics, v. 636, p. 100-110.

Nomade, S., Renne, P. R., and Merkle, R. K. W., 2004, 40Ar/39Ar age constraints on ore deposition and cooling of the Bushveld Complex, South Africa: Journal of the Geological Society, v. 161, no. 3, p. 411.

Norton, W. H., 1917, A Classification of Breccias: The Journal of Geology, v. 25, no. 2, p. 160-194.

Ord, A., and Hobbs, B., 2013, Localised folding in general deformations: Tectonophysics, v. 587, p. 30-45.

Passchier, C. W., 1984, The generation of ductile and brittle shear bands in a low-angle mylonite zone: Journal of Structural Geology, v. 6, no. 3, p. 273-281.

Passchier, C. W., and Trouw, R. A., 2005, Microtectonics, Springer Science & Business Media.

Perritt, S., and Roberts, M., 2007, Flexural-slip structures in the Bushveld complex, South Africa?: Journal of Structural Geology, v. 29, no. 9, p. 1422-1429.

Philpotts, A., 1964, Origin of pseudotachylites: American Journal of Science, v. 262, no. 8, p. 1008-1035.

Pittarello, L., Di Toro, G., Bizzarri, A., Pennacchioni, G., Hadizadeh, J., and Cocco, M., 2008, Energy partitioning during seismic slip in pseudotachylyte-bearing faults (Gole Larghe Fault, Adamello, Italy): Earth and Planetary Science Letters, v. 269, no. 1-2, p. 131-139.

Price, N. A., Johnson, S. E., Gerbi, C. C., and West Jr, D. P., 2012, Identifying deformed pseudotachylyte and its influence on the strength and evolution of a crustal shear zone at the base of the seismogenic zone: Tectonophysics, v. 518, p. 63-83.

Ray, S. K., 2004, Melt–clast interaction and power-law size distribution of clasts in pseudotachylytes: Journal of Structural Geology, v. 26, no. 10, p. 1831-1843.

Roberts, M., and Clark-Mostert, V., Is there some commonality with respect to geological structure in the Bushveld Complex and the Great Dyke, *in* Proceedings The 4th International Platinum Conference, Platinum in transition 'Boom or Bust', The Southern African Institute of Mining and Metallurgy2010.

Roeder, P., and Reynolds, I., 1991, Crystallization of chromite and chromium solubility in basaltic melts: Journal of Petrology, v. 32, no. 5, p. 909-934.

Rowe, C. D., and Griffith, W. A., 2015, Do faults preserve a record of seismic slip: A second opinion: Journal of Structural Geology, v. 78, p. 1-26.

Rowe, C. D., Kirkpatrick, J. D., and Brodsky, E. E., 2012, Fault rock injections record paleo-earthquakes: Earth and Planetary Science Letters, v. 335, p. 154-166.

Sanderson, D., and Marchini, W. R. D., 1984, Transpression: Journal of Structural Geology, v. 6, p. 449-458.

Schouwstra, R., Kinloch, E., and Lee, C., 2000, A short geological review of the Bushveld Complex: Platinum Metals Review, v. 44, no. 1, p. 33-39.

Schulte, R. F., Taylor, R. D., Piatak, N. M., and Seal II, R. R., 2010, Stratiform chromite deposit model: US Geological Survey, 2331-1258.

Scoates, J. S., and Wall, C. J., 2015, Geochronology of Layered Intrusions, *in* Charlier, B., Namur, O., Latypov, R., and Tegner, C., eds., Layered Intrusions: Dordrecht, Springer Netherlands, p. 3-74.

Scoon, R., 2002, A New Occurrence of Merensky Reef on the Flanks of the Zaaikloof Dome, Northeastern Bushveld Complex: Relationship between Diapirism and Magma Replenishment: Economic Geology, v. 97, p. 1037-1049.

Seabrook, C. L., Cawthorn, R. G., and Kruger, F. J., 2005, The Merensky Reef, Bushveld Complex: mixing of minerals not mixing of magmas: Economic Geology, v. 100, no. 6, p. 1191-1206.

Sharpe, M., and Chadwick, B., 1982, Structures in Transvaal sequence rocks within and adjacent to the eastern Bushveld Complex: Geological Society of South Africa Transactions, v. 85.

Shukla, M. K., and Sharma, A., 2018, A brief review on breccia: it's contrasting origin and diagnostic signatures: Solid Earth Sciences, v. 3, no. 2, p. 50-59.

Sibson, R., 1977, Fault rocks and fault mechanisms: Journal of the Geological Society, v. 133, no. 3, p. 191-213.

Sibson, R., 1985, A note on fault reactivation, 751-754 p.:

-, 1990, Conditions for fault-valve behavior: Geological Society, London, Special Publications, v. 54, p. 15-28.

Sibson, R., and Toy, V., 2006, The Habitat of Fault-Generated Pseudotachylyte: Presence vs. Absence of Friction-Melt.

Sibson, R. H., 1975, Generation of pseudotachylyte by ancient seismic faulting: Geophysical Journal International, v. 43, no. 3, p. 775-794.

Sibson, R. H., 1980, Transient discontinuities in ductile shear zones: Journal of Structural Geology, v. 2, no. 1, p. 165-171.

Sibson, R. H., 1995, Selective fault reactivation during basin inversion: potential for fluid redistribution through fault-valve action: Geological Society, London, Special Publications, v. 88, no. 1, p. 3.

Sibson, R. H., Robert, F., and Poulsen, K. H., 1988, High-angle reverse faults, fluid-pressure cycling, and mesothermal gold-quartz deposits: Geology, v. 16, no. 6, p. 551-555.

Smith, A., and Beukes, N., 2016, Paleoproterozoic Banded Iron formation-Hosted High Grade Hematite Iron Ore Deposits of Transvaal Supergroup, South Africa: Episodes, v. 39, p. 269.

Smith, S. A. F., Collettini, C., and Holdsworth, R. E., 2008, Recognizing the seismic cycle along ancient faults: CO2-induced fluidization of breccias in the footwall of a sealing low-angle normal fault: Journal of Structural Geology, v. 30, no. 8, p. 1034-1046.

Speckbacher, R., Stipp, M., Behrmann, J. H., and Heidelbach, F., 2013, Fluid-assisted fracturing, cataclasis, and resulting plastic flow in mylonites from the Moresby Seamount detachment, Woodlark Basin: Journal of Structural Geology, v. 56, p. 156-171.

Spray, J. G., 1992, A physical basis for the frictional melting of some rock-forming minerals: Tectonophysics, v. 204, no. 3, p. 205-221.

Spray, J. G., 1995, Pseudotachylyte controversy: Fact or friction?: Geology, v. 23, no. 12, p. 1119-1122.

Swanson, M. T., 1988, Pseudotachylyte-bearing strike-slip duplex structures in the Fort Foster Brittle Zone, S. Maine: Journal of Structural Geology, v. 10, no. 8, p. 813-828.

Tanner, G. P. W., 1989, The flexural-slip mechanism: Journal of Structural Geology, v. 11, no. 6, p. 635-655.

Tanner, P. W. G., 1992a, The duplex model: Implications from a study of flexural-slip duplexes, *in* McClay, K. R., ed., Thrust Tectonics: Dordrecht, Springer Netherlands, p. 201-208.

Tanner, P. W. G., 1992b, Morphology and geometry of duplexes formed during flexural-slip folding: Journal of Structural Geology, v. 14, no. 10, p. 1173-1192.

Torabi, A., and Berg, S. S., 2011, Scaling of fault attributes: A review: Marine and Petroleum Geology, v. 28, no. 8, p. 1444-1460.

Tullis, J., 1990, Experimental studies of deformation mechanisms and microstructures in quartzo-feldspathic rocks, *in* Barber, D. J., and Meredith, P. G., eds., Deformation Processes in Minerals, Ceramics and Rocks: Dordrecht, Springer Netherlands, p. 190-227.

Tullis, J., and Yund, R. A., 1987, Transition from cataclastic flow to dislocation creep of feldspar: Mechanisms and microstructures: Geology, v. 15, no. 7, p. 606-609.

Uken, R., 1998, The geology and structure of the Bushveld Complex metamorphic aureole in the Olifants River area.

Uken, R., and Watkeys, M. K., 1997, An interpretation of mafic dyke swarms and their relationship with major mafic magmatic events on the Kaapvaal Craton and Limpopo Belt: South African Journal of Geology, v. 100, no. 4, p. 341-348.

Vance, E. R., and Routcliffe, P., 1976, Heat treatment of some metamict allanites, Mineralogical Magazine, Volume 40, Cambridge University Press, p. 521-523.

Vigneresse, j. l., 2004, A new paradigm for granite generation: Transactions of the Royal Society of Edinburgh: Earth Sciences, v. 95, p. 11-22.

von Gruenewaldt, G., Sharpe, M., and Hatton, C., 1985, The Bushveld Complex; introduction and review: Economic Geology, v. 80, p. 803-812.

Welch, M., 2004, Novel high-pressure behavior in chlorite: A synchrotron XRD study of clinochlore to 27 GPa: American Mineralogist, v. 89, p. 1337-1340.

White, J. C., 2012, Paradoxical pseudotachylyte–Fault melt outside the seismogenic zone: Journal of Structural Geology, v. 38, p. 11-20.

Wilson, A. H., 2015, The earliest stages of emplacement of the eastern Bushveld Complex: development of the Lower Zone, Marginal Zone and Basal Ultramafic Sequence: Journal of Petrology, v. 56, no. 2, p. 347-388.

Wu, D., Pan, J., Xia, F., Huang, G., and Lai, J., 2019, The Mineral Chemistry of Chlorites and Its Relationship with Uranium Mineralization from Huangsha Uranium Mining Area in the Middle Nanling Range, SE China: Minerals, v. 9, no. 3, p. 199.

Zeh, A., Ovtcharova, M., Wilson, A. H., and Schaltegger, U., 2015, The Bushveld Complex was emplaced and cooled in less than one million years – results of zirconology, and geotectonic implications: Earth and Planetary Science Letters, v. 418, p. 103-114.